The Hong Kong Polytechnic University

Department of Mechanical Engineering

Experimental Investigation and Theoretical Analysis on Air Filtration of Sub-micron Aerosols by Nanofiber Filter

Chi-Ho HUNG

A thesis submitted in partial fulfillment of the requirements for the Degree of

Doctor of Philosophy

Initial submission: February 2010

CERTIFICATE OF ORIGINALITY

I hereby declare that this thesis is my own work and that, to the best of my knowledge and belief, it reproduces no material previously published or written, nor material that has been accepted for the award of any other degree or diploma, except where due acknowledgement has been made in the text.

(Signed)

Chi-Ho HUNG (Name of student)

Abstract

The filtration of sub-micron aerosol by a nanofiber medium with fiber diameter 100 – 400 nm is of great interest. For different polymeric materials, we found that both Poly-ethylene Oxide (PEO) nanofiber with fiber diameter 200 nm (fabricated in-house), or other polymeric nanofiber filters with fiber diameter 300 nm (acquired elsewhere), can both remove effectively 50 – 500 nm aerosol generated from a controlled aerosol source. The Payet model, which was originally developed for microfiber filter with Knudsen number of fiber (Kn_f) smaller than 0.1 under the assumption of continuum physics, has been demonstrated to predict the filtration of 50 – 500 nm aerosol using nanofiber filter with much larger Kn_f from 0.4 – 0.6 (transition regime for airflow) for filters with a wide range of solidosity (0.004 – 0.036) and fiber diameter (200 – 300 nm). For filtering these sub-micron aerosols, diffusion and interception by nanofibers has been found to be the dominant mechanisms due to large surface area-to-volume ratio of the nanofibers. In particular, we found good agreement on the diffusion capture mechanism on sub-micron aerosol between Payet's model and our experimental results for low Peclet number (*Pe*), i.e. a measure of convective transport to molecular diffusion, from 5 to 50 by varying the filter solidosity and face velocity. This range of *Pe* is much below what had been reported heretofore in the literature of over 1000.

Nanofiber can be a good filter medium or a coating on an existing medium. In either case, the filtration performance is higher compared to that of microfiber filter. The

disadvantage is that pressure drop is high especially for increasing amount of nanofiber in the filter which can achieve high filtration efficiency. Another part of our research is to develop novel methods to mitigate pressure drop for both clean and loaded nanofiber filters.

For clean filter, we have developed a novel multi-layering method wherein nanofibers are separately spaced out in web / mesh with support material as compared with having the same amount of nanofibers coated or deposited on a single-layer. This reduces pressure drop while achieving a very high filtration efficiency. This has been demonstrated by a reduction of pressure drop by 58 % using 12 layers of nanofiber with each layer having basis weight 0.06 gm^{-2} when compared to a single layer of nanofiber with the same total basis weight of 0.7 gm^{-2}.

For loaded filter, a dual-layer filter with microfibers upstream and nanofibers downstream was developed. This composite arrangement was found to reduce the skin layer effect (i.e. the large pressure drop across a short distance especially at the upstream face of nanofiber layer) by more evenly distributing the captured aerosols in both the microfiber and nanofiber layers.

A second method to reduce pressure drop in a loaded nanofiber filter is to back-pulse the nanofiber filter by pulsating air jet from the downstream end to discharge the deposited aerosol. This allows the filter to temporarily accumulate the solids as measured by pressure drop in excess of a threshold level before back-pulsing. Our

test under 60 hours of repeated loading and regeneration shows the increase in residual pressure drop by 64 Pa under an imposed threshold pressure drop of 300 Pa. This threshold pressure drop can be increased to over 1200 Pa for enhanced storage capacity in between cleaning.

We have also developed a model to explain the loading characteristics of the nanofiber filter as measured by a pressure drop. For light loading, aerosol build-up can be explained by a model wherein aerosol deposit surrounds each fiber, whereas at high solids loading, aerosol build-up in form of dendrites can be modeled by additional “deposit fibers”. Both models respectively at light to high solids loading compare well with the pressure drop measured experimentally. In addition, a model was developed to estimate the deposition profile (i.e. distribution of deposit mass, along filter thickness) including inhomogeneous filter with separate microfiber and nanofiber layers and challenged by polydisperse aerosol stream. This model is an improvement over past model which deals only with homogeneous filter containing single-size fibers challenged by monodisperse aerosol. This model helps to explain the much faster pressure drop increase rate of nanofiber filter and also the effectiveness of dual-layer media on mitigating filter clogging.

Publications arising from the thesis

Journal publications

Leung, W.W.F., Hung, C.H. (2008). Investigation on pressure drop evolution of fibrous filter operating in aerodynamic slip regime under continuous loading of sub-micron aerosols. *Separation and Purification Technology* 63: 691 – 700.

Leung, W.W.F., Hung, C.H., Yuen, P.T. (2009). Experimental investigation on continuous filtration of sub-micron aerosol by filter composed of dual-layers including a nanofiber layer. *Aerosol Science and Technology* 43: 1174 – 1183.

Leung, W.W.F., Hung, C.H., Yuen, P.T. (2010). Effect of face velocity, nanofiber packing density and thickness on filtration performance of filters with nanofibers coated on a substrate. *Separation and Purification Technology* 71: 30 – 37.

Conference proceedings

Leung, W.W.F., Hung, C.H. (2008). Experimental investigation on air filtration of sub-micron particulates by nanofiber filter. 10^{th} World Filtration Congress Proceedings Vol. III 156 – 160, 14^{th} – 18^{th} April 2008, Leipzig, Germany.

Acknowledgements

I wish to express my great thank to my supervisor Prof. Wallace Woon-Fong LEUNG, for his guidance, encouragement and support throughout the course of study. This project could not be completed without his invaluable supervision. I am also grateful to the Institute of Textile and Clothing, The Hong Kong Polytechnic University for their kindly sharing of the electrospinning machine.

Special thanks go to Mr. Chris TSANG and Mr. Bill YUEN from the Department of Mechanical Engineering, The Hong Kong Polytechnic University for their help throughout the project. Sincere thanks also go to the Staff in Project Laboratory of the Department of Mechanical Engineering, The Hong Kong Polytechnic University for their help of setting up the experimental rigs.

Finally, I would like to thank my family for their understanding and support over the years.

Table of contents

List of figures and tables

Table	Caption	Page
3.1	Parameters of the three model filters	25
4.1	Classification of flow regime based on Knudsen number of fiber	30
4.2	Specifications of nanofiber and microfiber filters	32
7.1	Physical parameters of substrate and nanofiber layers coated on it	99

List of symbols and abbreviations

List of symbols

A – Filter frontal area

$C(D_p, x, t)$ – Number concentration of size D_p aerosol at filter depth x and time t

C_c – Cunningham slip correction factor

$C_{in}(D_p)$ – Number concentration of aerosol with size D_p entering the filter

$C_m(x, t)$ – Mass concentration at filter depth x and time t

C_{m0} – Mass concentration of aerosol stream at filter inlet

$C_{out}(D_p)$ – Number concentration of aerosol with size D_p leaving the filter

c – Total solidosity [= $c_f + c_p$]

c_f – Clean filter solidosity (volume fraction occupied by fibrous material)

c_p – Deposit solidosity (volume fraction occupied by aerosol collected in filter)

c_{fl} – Local solidosity of original fiber in loaded filter (fig. 4.5)

c_{pl} – Local solidosity of deposit fiber in loaded filter (fig. 4.5)

D – Diffusion coefficient

D_p – Aerosol size

d_{en} – Enlarged fiber diameter

d_{eq} – Equivalent fiber diameter

d_f – Mean fiber diameter

e – Elementary charge

I_{ij} – Indicator function [= 0 when $i = j$, = 1 when $i \neq j$]

K – Expression appeared in eq. (4.9)

$K(x, t)$ – Deposition profile at filter depth x and time t

K_0 – Deposit mass per unit volume that causes the mass efficiency of filter slice to be doubled from its initial value, i.e. $2\alpha_0\Delta x$

Kn – Knudsen number of particle

Kn_f – Knudsen number of fiber

Kn_p – Knudsen number of deposit fiber

Ku – Kuwabara hydrodynamic factor

Ku_{eq} – Equivalent Kuwabara hydrodynamic factor

Ku_f – Kuwabara hydrodynamic factor of original fiber (fig. 4.5)

Ku_p – Kuwabara hydrodynamic factor of deposit fiber (fig. 4.5)

k – Air permeability

k_B – Boltzmann constant

M – Deposit mass per unit filter area

$M_A(t)$ – Deposit mass per unit area in filter A at time t

$M_D(t)$ – Deposit mass per unit area in filter D at time t

N – Number of deposit fibers formed for each original fiber (fig. 4.5)

n – Integer multiple of elementary charge

$n_d(D_p)$ – Size distribution of aerosol stream challenging the filter [$= dC_{in}(D_p) / d(D_p)$]

n_s – Number of air jet pulses

$P(D_p, \tau)$ – Aerosol penetration through loaded filter at time τ

$P_m(t)$ – Mass penetration of loaded filter at time t [$= C_m(Z, t) / C_{m0}$]

Pe – Peclet number

Q – Airflow rate

T – Absolute temperature

U – Face velocity [= Q / A]

W – Basis weight (mass of fibers per unit filter area)

X_i – Drag force per unit length acting on original fiber (X_f) or deposit fiber (X_p)

X_f – Drag force per unit length acting on original fiber (fig. 4.5)

X_p – Drag force per unit length acting on deposit fiber (fig. 4.5)

x^* – Dimensionless filter depth [= x / Z]

Z – Filter thickness

α_0 – Initial mass efficiency of a filter slice per unit length

Δc_f – Uncertainty of clean filter solidosity

ΔP – Pressure drop across filter

$\Delta P(\tau)$ – Pressure drop across loaded filter at time τ

ΔP_0 – Pressure drop across clean filter

ΔP_{max} – Pressure drop ceiling to trigger backflow regeneration

ΔP_1 – Pressure drop across loaded filter from model 1

ΔP_2 – Pressure drop across loaded filter from model 2

Δp_1 – Pressure drop across loaded filter in idealized condition shown in fig. 4.5

Δp_2 – Pressure drop across loaded filter in idealized condition shown in fig. 4.6

Δx – Filter slice thickness

ΔZ – Uncertainty of filter thickness

γ_{Dp} – Regression coefficient

η – Filtration efficiency (fractional efficiency)

$\eta(D_p, \tau)$ – Filtration efficiency of loaded filter at time τ

η_C – Overall filtration efficiency

η_D – Single fiber efficiency due to diffusion

η_f – Single fiber efficiency

η_N – Filtration efficiency of nanofiber layer

η_R – Single fiber efficiency due to interception

η_S – Filtration efficiency of substrate layer

$\eta_{sl}(D_p, x_i, t)$ – Filtration efficiency of filter slice at depth x_i and time t

μ – Air dynamic viscosity

ξ – Electrical mobility

$\Lambda(D_p)$ – Filtration efficiency raising factor

λ – Mean free path of air molecules

ρ_c – Deposit bulk density

ρ_f – Fiber material density

ρ_p – Aerosol material density

List of abbreviations

AD – Aerodynamic diameter

CPC – Condensation particle counter

EMD – Electrical mobility diameter

HEPA – High efficiency particulate air

MPPS – Most penetrating particle size

QF – Quality factor

Chapter 1

Literature review and introduction

Separation of particulate matters from gas stream is of primary importance in many applications such as engine emission reduction, dust control of industrial processes, automotive cabin, clean room air circulation systems and even personal respiration protection. Fibrous filter is one of the cost-effective means to remove particulate matters from gas stream and its mechanism of filtration has long been studied under both experimental and theoretical aspects [1 – 5]. Pich [2] has developed a model on pressure drop across fibrous filter with Knudsen number of fiber Kn_f (defined as ratio of the mean free path of air molecules to the radius of nanofiber, see eq. (2.5)) that lies in the range from 1×10^{-3} to 0.25, which classifies flow over individual fibers in aerodynamic slip regime. Based on his model, together with filtration efficiency models in aerodynamic slip regime reached by other researchers, Pich [2] suggested using very fine fibers for making non-woven fibrous filters, aiming for higher filtration efficiency and / or lower pressure drop. The theoretical side of aerosol filtration by fibrous filter with Kn_f above 0.25, i.e. transition regime from aerodynamic slip to molecular flow has seldom been studied, mainly due to the inapplicability of Navier-Stokes equations in describing flow over fibers and the complexity of solving Boltzmann equation [6]. Tafreshi et al. [7] has simulated the filtration of spherical aerosol with diameter chosen between 50 and 500 nm by non-woven fibrous medium composed of cylindrical fibers with diameter at 50, 100 and 200 nm (Kn_f = 2.7, 1.3 and 0.7). They assumed the filter operates under reduced

pressure with Kn_f larger than 10, which classifies flow over individual fibers in free molecule regime. To simplify the problem, they further assumed an undisturbed uniform flow over fibers owing to $Kn_f > 10$. Their 3-dimensional model of fibrous medium is generated from Poisson line process. Particle trajectory is obtained by solving the Langevin equation and particle capture is determined by the volume-exclusion method. Results show that filtration efficiency increases as fiber diameter decreases for clean filters of the same thickness and pressure drop. These theoretical studies provide standpoint on the use of nanofibers to enhance filtration performance, especially for filtering sub-micron aerosol.

To experimentally verify the filtration performance of nanofiber media, it is necessary to produce nanofibers and fabricate the fibers into air filters. Electrospinning is a reliable method to produce polymer-based nanofibers as a non-woven cloth. The origin of electrospinning can be traced back to several inventions on fiber spinning by electrostatic forces patented in United States during the 1930s [8 – 10]. Not until the past decade that electrospinning shows the capability of producing fibers in sub-micron range [11]. After this breakthrough, there is a vast amount of researches aiming to understand the effect of process parameters such as polymer type, solution viscosity and electric potential on the morphology of electrospun nanofibers [12 – 13]. The review article by Ramkumar et al. [12] gives a detail account on the characteristics, especially mean diameter, of fibers that have been electrospun from various polymer / solvent combinations.

The topic of nanofiber filtration has been getting more and more attention recently. Tsai et al. [14] has studied the filtration behavior of filter media composed of electrospun polycarbonate (PC), polyurethane (PU) and polyethylene oxide (PEO) fibers. Fiber diameter consistently lies in the range from 100 to 500 nm. PC and PU nanofibers show the ability to retain the charge from electrospinning, but not for PEO nanofibers. Hence, the filtration mechanism of a PEO nanofiber filter is purely mechanical. The basis weight of PEO in the filter media is 3 gm^{-2} and it shows a filtration efficiency of 78 % under the challenge of polydisperse NaCl aerosol with count median diameter (CMD) at 300 nm. The authors postulated that a capture efficiency of 99.97 % (i.e. HEPA level) can be achieved by increasing the basis weight to 16.2 gm^{-2}, which is much lower than the value of other non-woven making processes. It demonstrates the huge saving of polymer material by electrospinning as an alternative to fabricate filter media. Lee et al. [15] has successfully fabricated filter media composed of Nylon 6 (N6) electrospun fibers with diameter ranging from 80 to 200 nm, in various basis weight. The authors suggested that a basis weight between 5.75 and 10.75 gm^{-2} can produce filter media of capture efficiency and air permeability comparable to HEPA filter.

Polymer-based nanofibers produced from electrospinning are soft and can be easily destroyed by gentle rubbing. Hence, electrospun nanofibers in the form of non-woven cloth is seldom used alone as air filter. There are two methods to fabricate nanofibers into air filter sample ready for testing. Firstly, electrospun nanofibers can be mixed with microfibers through vacuum molding [16]. The

advantage is that the nanofibers are intermingled with and thus protected by the microfibers within the bulk fibrous structure. Secondly, nanofibers can be electrospun directly on another porous substrate, mostly an extremely permeable microfiber medium with negligible filtration efficiency over the target aerosol size range [17 – 20], thus forming an inhomogeneous dual-layer composite. The advantage is that the filtration efficiency across the composite can be approximated as that across the nanofiber layer, while the drawback is that the sample must be handled with great care to avoid the nanofibers being rubbed off from the surface.

Two important issues arise from past academic studies have to be addressed. Firstly, the effect of basis weight (which is related to solidosity), thickness and face velocity on the capture efficiency and pressure drop of nanofiber filter should be studied in detail. This is important to filter design, as we need to estimate the basis weight of nanofibers to achieve certain minimum filtration efficiency and also the incurred pressure drop under a specific face velocity. Wang et al. [18] showed that filter media composed of fibers with mean diameter at 150 nm have the most penetrating particle size (MPPS) decreases from 100 to 75 nm when solidosity increases from 0.034 to 0.134. Podgórski et al. [17] discovered that the quality factor of microfiber filter could be improved by coating it with a layer of nanofibers. Their nanofibers are produced from meltblown process with count median diameter at 700 nm. It is postulated that the quality factor can be further improved by using smaller fibers produced from electrospinning. Although these findings provide a general picture on the filtration characteristics of nanofiber media, they are limited to clean state

filtration. In practice, a filter is most likely loaded with aerosol in its life cycle, so it is necessary to study the performance of loaded nanofiber filter, and incorporates them in design stage. Contrary to nanofiber filter, there are many studies on the performance of loaded microfiber filter. Davies [21] has proposed an empirical model on flow resistance of loaded fibrous filter. Watson [22] published photographs showing the formation of dendrites on fiber surface during early stage of loading. Studies on pressure drop increase of High Efficiency Particulate Air (HEPA) filter, which is a microfiber filter with wide application, under continuous aerosol loading have been done by Bergman et al. [23], Vendel et al. [24], Letourneau et al. [25], Novick et al. [26] and Thomas et al. [27]. They also proposed various empirical models on pressure drop across loaded HEPA filter. Brown and Wake [28] and Podgórski [29] have proposed semi-empirical model on the deposition profile of homogeneous fibrous filter loaded with single size aerosol with steady concentration. Their formulation is based on mass balance and should be applicable regardless of the fiber diameter. Sakano et al. [30] modified the model to predict pressure drop across loaded filter composed of fibers with two diameters (i.e. binary fibers). Gradoń et al. [31] modeled the structure of aerosol deposition on fiber surface through Lattice-Boltzmann approach. Dunnett and Clement [32] used Boundary Element Method (BEM) to study the interaction between aerosol deposition and filtration efficiency of a loaded single fiber. Recently, Li and Marshall [33] used Discrete Element Method (DEM) to study the growth of dendrite on a single fiber within a loaded filter with the consideration of dendrite collapse and break-off due to fluid drag that leads to an oscillated number of particles deposited

on that single fiber. Most studies focused on pressure drop across loaded fibrous filter with $Kn_f < 1 \times 10^{-3}$, which classifies flow over an individual fiber in continuum regime. It is necessary to propose a model to predict the pressure drop across loaded fibrous filter with $1 \times 10^{-3} < Kn_f < 0.25$, preferably up to $Kn_f < 0.5$ that corresponds to $d_f > 250$ nm, which classifies flow over an individual fiber in early transition regime from aerodynamic slip to molecular flow.

The objective of this research is to study the filtration of sub-micron aerosol by nanofiber media, hence compare the strength and weakness of nanofiber filter against microfiber filter, followed by exploring ways to improve the filtration performance of nanofiber media making them promising substitute to conventional microfiber filters. This research involves experiments and mathematical modeling. Experimental filtration efficiency is obtained by challenging the filter sample with dry NaCl aerosol having electrical mobility diameter (EMD) chosen between 50 and 480 nm as produced from atomization combined with electrostatic classification, and measuring the aerosol concentration at filter upstream and downstream respectively by condensation particle counter. Theoretical clean filter efficiency is predicted from semi-empirical model adopted from literature [34], while new models are proposed for estimating the pressure drop and deposition profile across filter under continuous sub-micron aerosol loading.

Chapter 2 introduces the performance tests conducted in this research including filtration efficiency and pressure drop measurement, loading filter sample by aerosol

stream under controlled condition, and methods to estimate mean fiber diameter, thickness and solidosity of fibrous filter. Chapter 3 describes the correlation model on clean filter filtration efficiency offered by Payet et al. [34] that is used throughout the study. Chapter 4 discusses the effect of fiber diameter and filter solidosity on the filtration behavior at clean state from both experimental and theoretical angles. A semi-empirical model to estimate the pressure drop across a loaded filter is also developed. The predictions are compared against experimental results to see the effect of filter solidosity on the filtration behavior of loaded nanofiber filter. Chapter 5 studies the filtration behavior of filter composed of dual-layers including a nanofiber layer, which is regarded as one of the ways to improve the dust holding capacity of nanofiber filter. A semi-empirical model is also proposed to estimate the deposition profile across filter depth under continuous loading of polydisperse sub-micron aerosol stream. Chapter 6 introduces the backflow method to regenerate loaded nanofiber filter. The effectiveness of backflow regeneration on nanofiber filter under various degree of loading has been investigated. Chapter 7 evaluates the effect of face velocity, nanofiber layer solidosity and thickness on filtration efficiency and pressure drop of filters with nanofibers coated on a substrate. The nanofiber layer is self-produced by electrospinning. Judged from the results, a novel method of practical importance called “multi-layering” is proposed to fabricate nanofiber filter with greatly reduced pressure drop. Chapter 8 concludes the study and explores future research on electret nanofiber filter.

Chapter 2

Filtration performance tests and estimation of filter properties

2.1 Chapter introduction

The objective of this research is to study the performance of nanofiber media in filtering out sub-micron solid aerosol suspend in air. This Chapter summarizes the technical details of filtration performance tests used in this research. There are two indicators on filtration performance, namely the filtration efficiency (η) and pressure drop across the filter (ΔP). Unless otherwise specified, filtration efficiency (also being commonly referred as fractional efficiency) always adopt the definition described in eq. (2.1):

$$\eta = 1 - \frac{C_{out}(D_p)}{C_{in}(D_p)} \qquad \text{Eq. (2.1)}$$

where $C_{in}(D_p)$ and $C_{out}(D_p)$ are the number concentration (usually in cm^{-3}) of aerosol with "size" D_p entering and leaving the filter respectively. For a spherical particle, its "size" refers to the diameter. However, for an irregular aerosol, its "size" has various definitions depending on the method of aerosol sampling and measurement. The definition of aerosol "size" adopted in this research will be explained in Section 2.2.

The most penetrating particle size (MPPS) of filter media composed of fibers with mean diameter (d_f) from 1 to 10 μm is around 0.3 μm. The nanofiber filter media in this study have d_f from 0.2 to 0.3 μm. From filtration theory, the MPPS decreases with d_f. Hence, the MPPS of our nanofiber filter media should be smaller than that of

microfiber media, i.e. 0.3 μm. We then choose 0.05 μm as the starting aerosol size up to 0.48 μm, which allows us to locate the MPPS for all types of filters in this study. In addition, our aerosol size range from 0.05 to 0.48 μm is large enough to cover the test range specified under various test standards of high performance filter media, such as ASTM F2299 [35], 42 CFR Part 84.181 [36], BS EN 13274-7 [37], and BS EN 1822-1 [38], making our test results in line with industrial standard.

Pressure drop across an air filter reflects its airflow resistance. Air filters, no matter they are granular bed or fibrous filters, belong to the category of porous material. Hence, they obey the Darcy's Law under laminar flow condition, as represented by eq. (2.2):

$$\frac{\Delta P}{U} = \frac{\mu c_f Z}{k} \qquad \text{Eq. (2.2)}$$

where U is the face velocity, usually defined as airflow rate (Q) divided by filter frontal area (A), c_f is the volume fraction occupied by fibrous material within the filter, usually referred as solidosity and $1 - c_f$ is the porosity, Z is the filter thickness, μ is the air dynamic viscosity, and k is the air permeability. Darcy's Law shows that ΔP increases with the decrease in k under fixed U. In practice, pressure drop is used more often than air permeability when evaluating the filtration performance.

In filtration industry, it is usual to combine filtration efficiency and pressure drop into a single indicator known as the quality factor (QF), according to eq. (2.3):

$$QF = -\frac{\ln(1-\eta)}{\Delta P} \qquad \text{Eq. (2.3)}$$

QF can be regarded as a benefit-to-cost ratio, with the normalized filtration efficiency $-\ln(1-\eta)$ as the benefit and pressure drop ΔP as the cost. A filter with greater η and/or lower ΔP than another possesses higher *QF*, reflecting its better quality.

During extended use in dusty airflow, the microstructure within a fibrous filter changes continuously. At the beginning, the aerosol starts to deposit on individual fibers. As filtration continues, the upcoming aerosol starts to deposit on both the fibers and aerosol collected in earlier stage. The deposition grows into dendrite and clogs up the filter eventually. This temporal change of filter status, due to continuous aerosol loading affects the filtration efficiency and pressure drop, is worth to investigate.

Hence, the filtration performance tests conducted in this research are mainly:

(a) Filtration efficiency and pressure drop measurement, and

(b) Loading initially clean filter samples by aerosol stream under controlled condition.

Section 2.2 elaborates the method used to measure filtration efficiency and pressure drop of a filter. Section 2.3 develops the scheme to load up filter samples. Section 2.4 summarizes ways to estimate other properties of a fibrous filter, including the mean fiber diameter, filter thickness and filter solidosity.

2.2 Filtration efficiency and pressure drop measurement

Figure 2.1 shows the layout of experiment set-up to measure filtration efficiency. Its design and operation has taken reference from international standards [35 – 38] and past academic studies [15, 39 – 40]. About 1.6 g of sodium chloride (NaCl) is first dissolved in 80 cm^3 of water to form an aqueous solution containing 5 wt. % of NaCl. The NaCl solution is atomized by compressed air supplied continuously to the stainless steel atomizer. The atomized polydisperse NaCl aerosol stream is mixed with dilution air in properly adjusted flow rate and its moisture content is removed by passing through the Nafion membrane dryer. The dried aerosol then passes through the aerosol neutralizer containing a Polonium-210 (Po-210) radioactive source to reach the Boltzmann equilibrium charged state [41]. The impactor located at the downstream of aerosol neutralizer removes larger particles by aerodynamic means. The aerosol stream then goes into the electrostatic classifier (MSP Corp., SMAG 7388L) installed with a vertical electrode connected to high voltage source. The electrode voltage can be adjusted from 10 V to 10 kV so that only aerosol with specific electrical mobility (ξ) can be attracted towards the slit located at electrode lower end by traveling through a fixed parabolic trajectory. For a spherical particle, ξ is related to its diameter D_p as follows:

$$\frac{D_p}{C_c} = \frac{ne}{3\pi\mu\xi} \qquad \text{Eq. (2.4)}$$

where e is the elementary charge equals to 1.607×10^{-19} C, n is the integer multiple of elementary charge, C_c is the Cunningham slip correction factor equals to $1 + Kn[1.207 + 0.44\exp(-0.78 / Kn)]$ [42], and ξ is the electrical mobility. Kn is the

Knudsen number of particle defined as:

$$Kn = \frac{2\lambda}{D_p} \qquad \text{Eq. (2.5)}$$

where λ is the mean free path of air molecules.

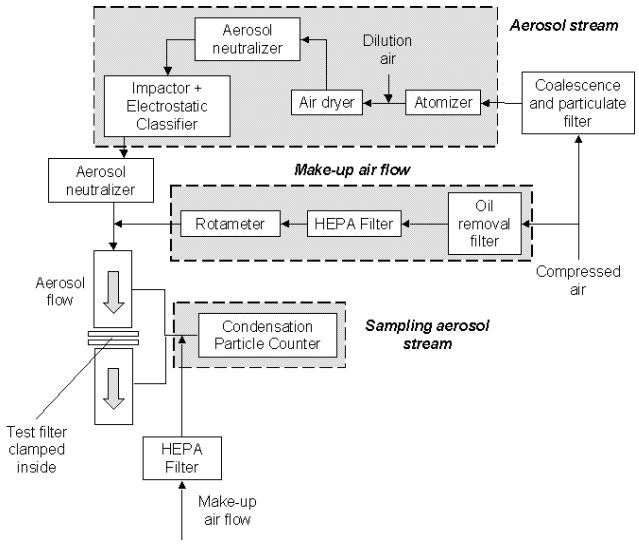

Fig. 2.1 Schematic of experiment set-up to measure filtration efficiency

For the irregular NaCl aerosol used in this study, its "size" is the electrical mobility diameter (EMD) defined as the diameter (D_p) of a sphere, as calculated from eq. (2.4) with n = 1 and a given ξ. Unless otherwise specified, aerosol size in this research always refers to EMD with the symbol D_p. Another diameter measure commonly used in aerosol science is the aerodynamic diameter (AD). For clarity, eq. (2.6) gives the conversion between EMD and AD. Filtration efficiency is measured by challenging the filter with NaCl aerosol ranging from 50 to 480 nm, followed by measuring the aerosol concentration at filter upstream and downstream alternatively.

$C_c(D_p', \lambda)(D_p')^2 = C_c(D_p, \lambda)D_p^2\rho_p$ Eq. (2.6)

where D_p and D_p' represent the EMD and AD respectively, C_c is the Cunningham slip correction factor first appear in eq. (2.4), and ρ_p is the material density of the assumed spherical aerosol.

The attracted aerosol with specific ξ (i.e. D_p) is directed into a vertical test rig where the filter sample is installed in the middle section. The aerosol is mixed with dried and HEPA filtered make-up air for bringing up the aerosol flow to desired face velocity. A Condensation Particle Counter (TSI, CPC 3010) connected with a vacuum suction pump is used to sample and measure aerosol concentration at filter upstream and downstream alternatively, through corresponding sampling outlets fixed with isokinetic tubes.

Eq. (2.4) shows that electrostatic classification generates aerosol stream containing particles having the same ξ but different sets of (D_p, n). This is known as the multiple-charge effect. Since the filtration efficiency is measured by challenging the filter with aerosol size-by-size, the in-built software provided by manufacturer cannot be used to perform charge correction. A retrofit program written in Microsoft® Visual C++ is used instead to correct the filter upstream and downstream aerosol concentration as measured by CPC. Its algorithm is explained in Appendix I. After charge correction, the actual $C_{in}(D_p)$ and $C_{out}(D_p)$ can be substituted into eq. (2.1) for determination of experimental η.

It is helpful to provide more operation details of key experimental devices (impactor, electrostatic classifier, and condensation particle counter) as the accuracy of the experimental results in this work are strongly related on the way the measurements are performed.

An impactor is mounted on the outside of the electrostatic classifier. The aerosol first enters an impactor, which removes particles above a known size by inertial impaction. The impaction plate deflects the flow to form a 90° bend in the streamlines. Large particles with sufficient inertia are unable to follow the streamlines and impact on the plate. Smaller particles avoid hitting the plate and enter a small passage in the nozzle. Thus, the impactor is used to remove particles larger than a known aerodynamic size. The aerodynamic size at which the particles are separated is called the cut-point diameter. The cut-point diameter is a function of the impactor flow rate and nozzle diameter.

In the electrostatic classifier, the aerosol enters a Po-210 bipolar charger (commonly known as neutralizer), which exposes the aerosol particles to high concentrations of bipolar ions. The particles and ions undergo frequent collisions due to the random thermal motion of the ions. The particles quickly reach a state of equilibrium, in which they carry a bipolar charge distribution that can be approximated by Wiedensohler's expression [41]. The charged aerosol passes from the neutralizer into the main portion of the electrostatic classifier. The main portion contains two concentric metal cylinders. The polydisperse aerosol and sheath air are introduced at

the top of the classifier and flow down the annular space between the cylinders. The aerosol surrounds the outer core of sheath air, and both streams flow laminarly down the annulus with no mixing. The inner cylinder, also known as the collector rod, is maintained at a controlled negative voltage, while the outer cylinder is electrically grounded. This creates an electric field between the two cylinders. The electric field causes positively charged particles to be attracted through the sheath air to the negatively charged collector rod. Particles are precipitated along the length of the collector rod. The locations of the precipitating particles depend on the particle electrical mobility (ζ), the classifier flow rate, and the classifier geometry. Particles with high electrical mobility are precipitated along the upper portion of the rod. Particles within a narrow range of electrical mobility exit with the monodisperse air flow through a small slit located at the bottom of the collector rod. These particles are transferred to the test rig for efficiency testing or condensation particle counter to determine the particle concentration. The remaining particles are removed from the classifier via the excess air flow.

The aerosol concentration is measured by the condensation particle counter (CPC). As an aerosol first enters the CPC, it is saturated with alcohol vapor as it passes over a heated pool of alcohol. The vapor-saturated aerosol stream then flows into a cold condenser, where it is cooled by thermal diffusion. The alcohol condenses onto the particles and the particles grow into droplets large enough to be counted optically. The mechanism used to grow particles in the CPC is heterogeneous condensation, whereby particle growth is promoted by the presence of condensation nuclei. The

saturation ratio of the condensing vapor determines the smallest particle size detected by the CPC. As the temperature difference increases, the saturation ratio increases, thereby lowering the minimum particle diameter that can be detected. Our TSI Model 3010 CPC has a lower particle detection size of 10 nm. Once the particles have grown to an optically detectable size, which is typically 2 to 3 μm, they are able to scatter light onto a photodetector. At concentrations below 10,000 particles cm^{-3}, the pulse of light scattered by each particle is counted separately and the concentration is computed from the frequency of the pulses. At concentrations above 10,000 particles cm^{-3}, the effect of coincidence becomes significant and correction factor should be applied on the concentration reading.

NIST (National Institute of Standard and Testing) traceable calibration using NIST SRM-1963 296 nm Polystyrene Latex (PSL) spheres is performed annually by service engineer from MSP Corp. to ensure the sizing accuracy of our sub-micron aerosol generation and measurement system.

The filtration efficiency test of each aerosol size (D_p) is repeated 3 to 5 times. The average value is used to construct a 5 % confidence interval based on Student's t-test. The 5 % confidence interval is then checked for lying within the interval corresponds to ± 2.5 % of the mean value. For example, if the mean value is 0.7 (70 % efficiency), the result is accepted when the 5 % confidence interval lies within 0.6825 to 0.7175 (68.25 to 71.75 % efficiency).

Pressure drop across the filter is measured by the Capillary Flow Porometer (PMI, CFP-1100A). The CFP gradually increases the flow across the filter and measures its pressure drop accordingly, thus generates a pressure drop-against-flow curve (typical to the one as shown in figure 2.2). Linear regression is used to obtain the best-fitted straight line. This method is accurate since the fibrous filters in this study belong to the category of porous media that obeys the Darcy's Law, which suggests a linear relationship between ΔP and U according to eq. (2.2). The pressure drop at a specific U is then obtained by projection from the best-fitted straight line.

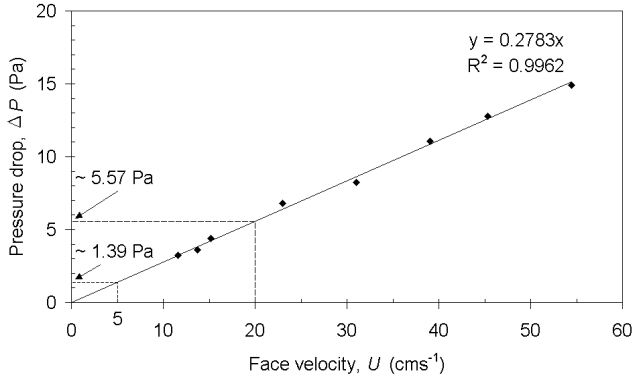

Fig. 2.2 Typical pressure drop-against-flow curve

2.3 Loading filter by aerosol stream under controlled condition

To simulate extended use in dusty environment, filter samples are loaded continuously by neutralized (actually bi-polar charged close to Boltzmann equilibrium charged state) polydisperse NaCl aerosol generated from atomization. The set-up for loading filter under controlled condition is depicted in figure 2.3. It is

somewhat similar to that shown in figure 2.2 for testing of filtration efficiency, but with the electrostatic classifier and CPC connected together and operated in scanning mode to measure the aerosol size distribution at filter upstream and downstream respectively. Both the face velocity and aerosol size distribution are maintained at constant levels to ensure a steady loading. A typical size distribution of atomized polydisperse NaCl aerosol adopted in this study is shown in figure 2.4 with peak concentration approaching 1×10^5 cm^{-3}. The distribution is a log-normal one having a mode at 75 nm. Pressure drop across the loaded filter is monitored throughout the loading process. Filtration efficiency is measured at regular time interval by switching the loading set-up back to the one depicted in figure 2.1.

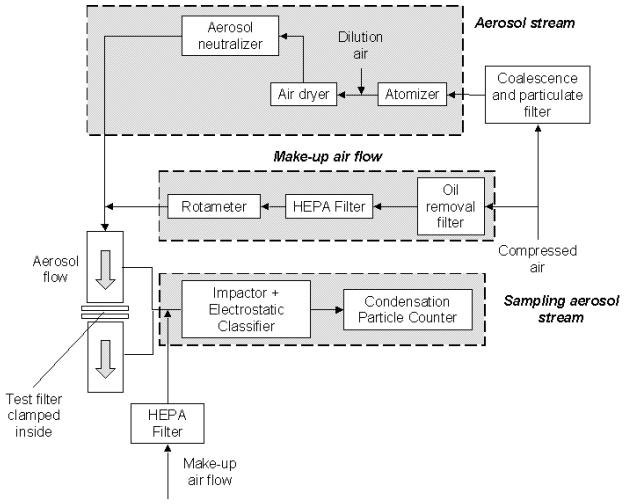

Fig. 2.3 Schematic of experiment set-up to load filter samples

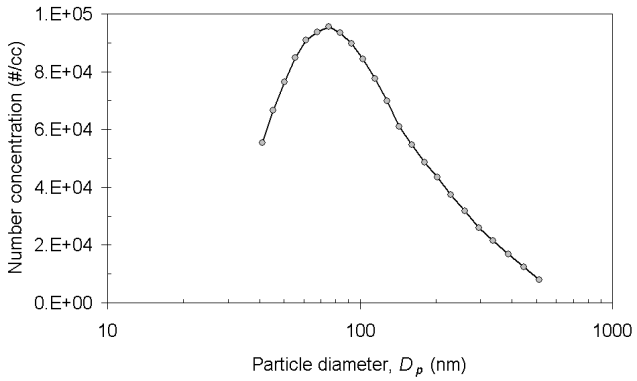

Fig. 2.4 Typical size distribution of atomized polydisperse NaCl aerosol

2.4 Estimation of mean fiber diameter, filter thickness and filter solidosity

The mean fiber diameter (d_f), thickness (Z) and solidosity (c_f) are important structure properties of a fibrous filter that affect its filtration efficiency (η) and pressure drop (ΔP). d_f is estimated from pictures obtained by Scanning Electron Microscope (JEOL, JSM 6490). Figure 2.5 shows an SEM picture on one of the nanofiber filters in this study. The diameter of each fiber is measured directly from the SEM picture. d_f is then estimated by taking the average of 50 to 100 fibers, contributed from at least three SEM pictures taken from different locations on the nanofiber filter. It also leads to other useful statistics on fiber diameter such as the standard deviation and empirical distribution function (EDF).

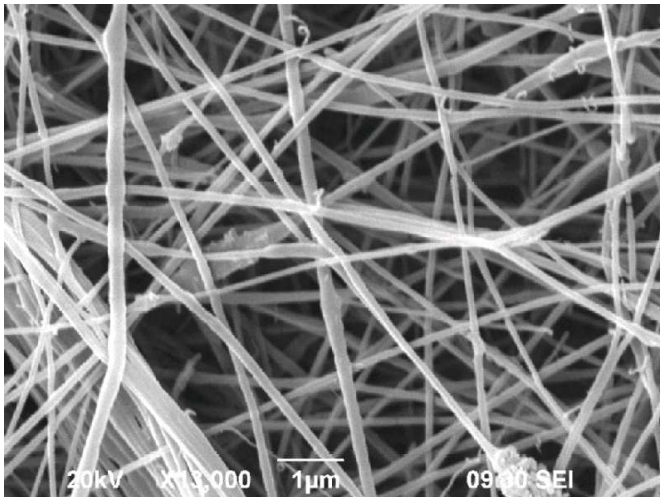

Fig. 2.5 SEM picture (magnification = 13 kX, JEOL JSM 6490) on one of the nanofiber filters

A micrometer can be used to measure the fibrous filter when its thickness is greater than 1×10^{-4} m. This applies to most of the microfiber filters in this study. On the other hand, nanofiber layer is too thin and its thickness is hardly detectable by micrometer. The original approach is to view the cross-section of nanofiber layer under SEM and measure its thickness directly from the SEM picture. However, technical difficulties hinder the use of this approach. Firstly, the cross-section of nanofiber as viewed under SEM is heavily deformed during mechanical cutting. It is because the cutting tools are unable to produce a sharp cut on the soft nanofibers. Instead, the nanofibers are torn apart and damaged during the cutting process. Secondly, the profile of the cross-section of nanofiber layer is rough and it becomes difficult to define an accurate and uniform thickness from the SEM pictures. Since the direct measurement approach is not applicable, Davies' empirical formula given by eq. (2.7) is proposed to estimate the thickness of nanofiber layer from

experimentally determined pressure drop value.

$$\frac{(\Delta P)d_f^2}{4\mu UZ} = 16c_f^{1.5}\left(1+56c_f^3\right) \qquad \text{Eq. (2.7)}$$

Eq. (2.7) is obtained by Davies [43] through testing of fibrous filter with d_f ranging from 1.6 to 80 μm and c_f smaller than 0.3. ΔP across a clean fibrous filter measured experimentally should be within ± 30 % [43] to that estimated from eq. (2.7), provided that 1.6 μm < d_f < 80 μm and 0.006 < c_f < 0.3. Subsequently, Davies' correlation was further validated by Werner and Clarenburg [44] to cover the finer range on fiber diameter (98 nm < d_f < 1.54 μm and 0.039 < c_f < 0.084). Filter solidosity c_f is defined as:

$$c_f = \frac{W}{\rho_f Z} \qquad \text{Eq. (2.8)}$$

where W is the mass of fibers per unit filter area (basis weight) and ρ_f is the fiber material density. Substitute eq. (2.8) into eq. (2.7) yields:

$$\frac{(\Delta P)d_f^2\rho_f}{4\mu UW} = 16c_f^{0.5}\left(1+56c_f^3\right) \qquad \text{Eq. (2.9)}$$

By knowing W and ρ_f beforehand and after measuring ΔP across the filter, c_f can be estimated according to eq. (2.9). It follows that Z can be obtained simultaneously from eq. (2.8) using the estimated c_f from eq. (2.9).

The uncertainties of derived quantities c_f and Z can be obtained from experimental uncertainty analysis based on the uncertainties in the experimentally measured quantities ΔP and d_f.

For $c_f < 0.056$, eq. (2.9) can be approximated as:

$$\frac{(\Delta P) d_f^2 \rho_f}{4\mu U W} = 16 c_f^{0.5} \qquad \text{Eq. (2.10)}$$

Hence, the uncertainties on variables in eq. (2.10) are related by:

$$\frac{d(\Delta P)}{\Delta P} + 2\frac{d(d_f)}{d_f} + \frac{d(\rho_f)}{\rho_f} - \frac{d\mu}{\mu} - \frac{dU}{U} - \frac{dW}{W} = \frac{1}{2}\frac{d(c_f)}{c_f} \qquad \text{Eq. (2.11)}$$

where the $d(\ )$s' are the uncertainties on corresponding variables. Since ΔP and d_f are the only measured quantities, eq. (2.11) can be further simplified to:

$$\frac{d(c_f)}{c_f} = 2\left[\frac{d(\Delta P)}{\Delta P} + 2\frac{d(d_f)}{d_f}\right] \qquad \text{Eq. (2.12)}$$

where $d(c_f)$, $d(\Delta P)$, and $d(d_f)$ are the uncertainties on c_f, ΔP, and d_f respectively. Similarly, from eq. (2.8),

$$\frac{d(c_f)}{c_f} + \frac{d(\rho_f)}{\rho_f} + \frac{dZ}{Z} = \frac{dW}{W} \qquad \text{Eq. (2.13)}$$

Again, eq. (2.13) can be further simplified to:

$$\frac{d(Z)}{Z} = -\frac{d(c_f)}{c_f} \qquad \text{Eq. (2.14)}$$

where dZ is the uncertainty on Z.

For filter with Z being measured directly by micrometer, eq. (2.8) is used to determine c_f when ρ_f is known. On the other hand, eq. (2.7) is used to estimate c_f when ρ_f is unknown.

Chapter 3

Model on clean filter filtration efficiency

3.1 Chapter introduction

This Chapter introduces the correlation model on clean filter filtration efficiency that is used throughout the study. It is offered by Payet et. al [34] and shows close agreement with experimental results when D_p lies within 80 to 400 nm and d_f as small as 1 μm. There are many approaches to model filtration efficiency. A classical method is to simplify the non-woven fibrous media as an array of cylinders transverse to flow, followed by finding the fraction of particles being collected by a single cylinder. The flow field around the single cylinder can be either Kuwabara [45] or Happel [46], with Kuwabara's showing closer agreement with experimental results [47]. Both Eulerian and Lagrangian approach can model particle transport across the single cylinder. In Eulerian approach, the aerosol flow is described by continuum based equations same as the continuous phase. Single fiber efficiency is obtained by solving the concentration gradient around the cylinder [1]. In Lagrangian approach, aerosol is treated as individual rigid spheres governed by Newton's 2nd Law. Different mechanisms such as diffusion, interception and gravitation are represented by various external forces appear in the force balance equation [48]. Single fiber efficiency is given by the fraction of spheres with traveling path touching the cylinder. The single fiber efficiency is then scaled up to filter efficiency based on the cylinder array model. The correlation model proposed

by Payet et. al [34] results from the above method. Their expressions on single fiber efficiency are found out by Eulerian means and empirically correlated, which are given in Section 3.2.

3.2 Expressions of the correlation model

A clean non-woven fibrous filter can be simplified as an array of cylinders transverse to aerosol flow for which the filtration efficiency (η), filter solidosity (c_f), single fiber efficiency (η_f), filter thickness (Z) and mean fiber diameter (d_f) are all related as follows [5]:

$$\eta = 1 - \exp\left[-\frac{4 c_f \eta_f Z}{\pi (1 - c_f) d_f} \right] \qquad \text{Eq. (3.1)}$$

For sub-micron aerosol, the interaction of diffusion and interception is significant, and inertial impaction is usually neglected. The single fiber efficiency is given by:

$$\eta_f = \eta_D + \eta_R \qquad \text{Eq. (3.2)}$$

where η_D and η_R are the single fiber efficiencies due to diffusion and interception respectively, and are expressed in eqs. (3.3) and (3.4) accordingly [34]:

$$\eta_D = 1.6 \left(\frac{1 - c_f}{Ku} \right)^{1/3} Pe^{-2/3} C_1 C_2 \qquad \text{Eq. (3.3)}$$

where $Ku = -(\ln c_f) / 2 + c_f - c_f^2 / 4 - 3 / 4$ is the Kuwabara hydrodynamic factor, $Pe = U d_f / D$ is the Peclet number, $D = k_B T C_c / 3\pi\mu D_p$ is the diffusion coefficient, k_B is the Boltzmann constant, T is the absolute temperature, and C_c is the Cunningham

slip correction factor that has appeared once in eq. (2.4).

$$\eta_R = 0.6\left(\frac{1-c_f}{Ku}\right)\left(1+\frac{Kn_f}{D_p/d_f}\right)\left(\frac{D_p^2/d_f^2}{1+D_p/d_f}\right) \qquad \text{Eq. (3.4)}$$

where D_p / d_f is sometimes referred as the interception ratio. The constants C_1 and C_2 are given by:

$$C_1 = 1 + 0.388Kn_f[(1-c_f)Pe / Ku]^{1/3} \qquad \text{Eq. (3.5)}$$

$$C_2 = \frac{1}{1+1.6\left[(1-c_f)/Ku\right]^{1/3}Pe^{-2/3}C_1} \qquad \text{Eq. (3.6)}$$

Examples are provided to illustrate the relative importance of diffusion and interception on capture efficiency and most penetrating particle size (MPPS) of fibrous filter. Table 3.1 shows the parameters of the three model filters.

Filter no.	1	2	3
Mean fiber diameter, d_f (μm)	3	1	3
Face velocity, U (cms^{-1})	8	8	16
Filter solidosity, c_f	0.1		
Filter thickness, Z (m)	1×10^{-4}		
Air temperature (^oC)	25		
Aerosol density (gcm^{-3})	2.16		

Table 3.1 Parameters of the three model filters

In figures 3.1 and 3.2, subscripts 1, 2 and 3 represent the single fiber efficiencies of model filters 1, 2 and 3, subscripts *D* and *R* represent the single fiber efficiencies due

to diffusion and interception respectively, while subscript *f* represents the combined single fiber efficiency described by eq. (3.2). As can be seen from figure 3.1, reducing d_f from 3 to 1 μm while maintaining c_f at 0.1 enhances both the diffusion and interception mechanisms by providing larger specific surface area for aerosol deposition. The combined single fiber efficiency thus increases from η_{1f} to η_{2f}. The lower MPPS of filter 2 than filter 1 is due to the larger enhancement on interception than diffusion mechanism by finer fibers. As verified by experimental results presented in later Chapters, nanofibers really provide higher efficiency with lower MPPS than microfibers.

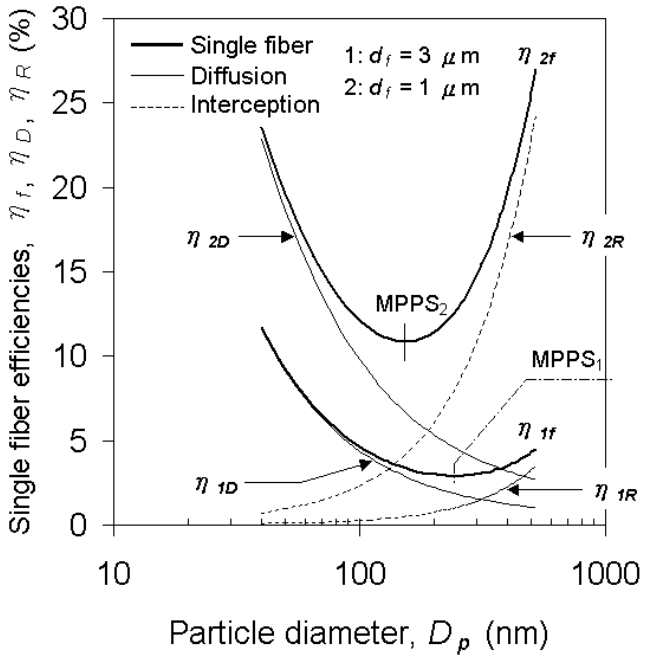

Fig. 3.1 Change on single fiber efficiencies and MPPS under reduction on fiber diameter

Figure 3.2 shows the change on single fiber efficiencies when *U* increases from 8 to

16 cms^{-1}. Increase on U does not affect the interception mechanism as eq. (3.4) already shows that η_R is independent of U. However, higher U shortens the traveling time of aerosol through the fibrous filter and reduces the chance for them to collide on fibers through Brownian motion, consequently leads to lower η_D. The combined effect is that capture efficiency decreases with MPPS shifts down, as indicated by curves η_{1f} and η_{3f} in figure 3.2.

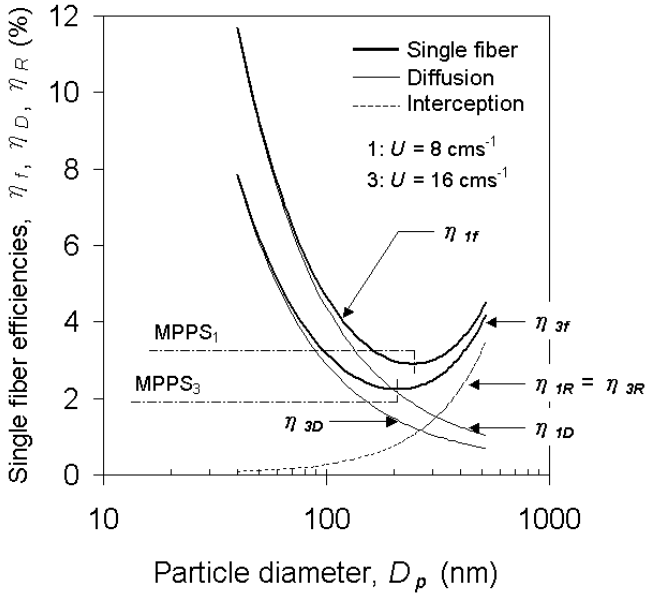

Fig. 3.2 Change on single fiber efficiencies and MPPS under increase on face velocity

Figure 3.3 shows the filter efficiencies η augmented from single fiber efficiencies η_f through eq. (3.1). The enhancement on η_f by finer fibers as observed from figure 3.1 is largely amplified in figure 3.3 when η is concerned.

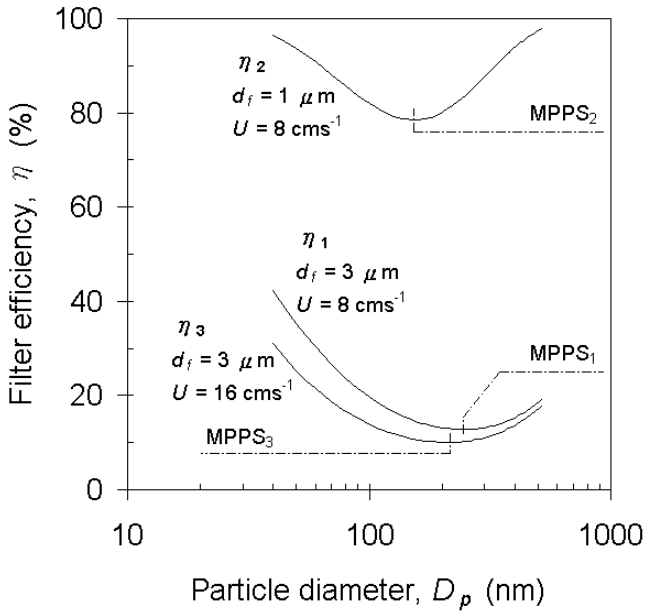

Fig. 3.3 Capture efficiencies of model filters 1, 2 and 3

Chapter 4

Filtration behavior of loaded nanofiber filter

4.1 Chapter introduction

Throughout the years, many ways have been developed to enhance the filtration performance of air particulate fibrous filter [49]. One of the possible ways is to fabricate extremely fine fibers down to nano-scale in order to increase specific surface area for filtration. There is a vast amount of theoretical studies on pressure drop across clean (unused) fibrous filters, from continuum to aerodynamic slip regime [5]. Pressure drop increase of fibrous filter under continuous aerosol loading has been studied by Bergman et al. [23], Vendel et al. [24], Letourneau et al. [25], Novick et al. [26] and Thomas et al. [27] focusing on the high efficiency particulate air (HEPA) filters. While Brown and Wake [28], Sakano et al. [30] and Miguel [50] have developed more general pressure drop models not specific to loaded HEPA filters.

In most applications such as indoor ventilation, industrial and engine filtration, filtration behavior of fibrous filter under continuous aerosol loading is one of the important indicators to filter performance. For example, when two filters have identical filtration efficiency and pressure drop in a clean state, the one with faster pressure drop increase rate during loading is regarded to have poorer performance since it clogs up faster. To obtain a full picture on the usefulness of nanofiber filter,

its filtration behavior in a loaded state should also be assessed. While the filtration behavior of microfiber filter under solid aerosol loading is well studied [23 – 28, 30, 50], there is little published data on the side of nanofiber filter. Hence, this Chapter will focus on studying the filtration efficiency and pressure drop elevation of loaded nanofiber filter. As a note, Chapters 4 to 6 belong to earlier stage of this research project and the experimental results are obtained by testing filters supplied by manufacturer. In later stage, we are able to self-produce nanofiber filters through electrospinning method and Chapter 7 will investigate the filtration behavior of these self-produced samples.

Flow in fibrous filter can be classified as different regime according to the Knudsen number of fiber (Kn_f). Table 4.1 lists the classification of flow regime based on Kn_f.

Knudsen number of fiber, Kn_f	Flow regime
$Kn_f < 0.001$	Continuous
$0.001 < Kn_f < 0.25$	Aerodynamic slip
$0.25 < Kn_f < 10$	Transition
$Kn_f > 10$	Molecular

Table 4.1 Classification of flow regime based on Knudsen number of fiber

Nanofiber filters in this study have mean fiber diameter (d_f) from 200 to 300 nm. The corresponding Kn_f lies between 0.44 and 0.66, in which flow over fibers belongs to the early transition regime. Hence, the aerodynamic slip model will be used to

develop a new semi-empirical model for estimation of pressure drop across a nanofiber filter loaded with sub-micron solid aerosol. Predictions from this new model will be compared against experimental results.

Section 4.2 discusses the effect of filter solidosity and fiber diameter on the filtration behavior of clean fibrous filter from both experimental and theoretical angles. Section 4.3 develops a new semi-empirical model to estimate the pressure drop across a loaded filter, which helps to predict and explain the filtration behavior of a nanofiber filter under sub-micron solid aerosol loading. Section 4.4 studies the effect of filter solidosity on the filtration behavior of loaded nanofiber filter through experiments. Section 4.5 briefly concludes the findings in this Chapter by summarizing the performance of nanofiber filter in clean and loaded state. It serves as the basis for follow-up studies aiming to improve the performance of nanofiber filters as explored in Chapters 5 and 6.

4.2 Filtration efficiency and pressure drop of clean filter

The specifications of both nanofiber and microfiber filters studied in this Chapter are listed in table 4.2.

	Nanofiber			Microfiber
Filter	A	B	C	D
Mean fiber diameter, d_f (nm)	300	300	300	1,800

Filter thickness, Z ($\times 10^{-5}$ m)	1	1	1	10
Filter solidosity, c_f	0.024	0.017	0.011	0.048
Pressure drop ΔP at 5 cms^{-1} (Pa)	24.5	14.7	9.8	19.6

Table 4.2 Specifications of nanofiber and microfiber filters

Nanofiber filters A, B and C are produced by coating nanofiber web on extremely porous coarse fiber substrate (d_f = 14.7 μm). The coarse fiber substrate acts as a framework for anchoring of nanofibers and offers negligible filtration efficiency and pressure drop. Mean fiber diameter d_f is estimated from SEM pictures according to the procedures introduced in Secction 2.4. Filter thickness Z of A to C refers to the thickness of nanofiber web instead of the whole filter. Manufacturer provides the thickness values of filters A to D. Filter solidosity c_f is estimated from eq. (2.6). Again, c_f of filters A to C refer only to nanofiber web.

Figures 4.1 and 4.2 show the SEM pictures of nanofiber filter A and microfiber filter D respectively. Figure 4.1 clearly shows that filter A has the nanofiber web coated on coarse fiber substrate.

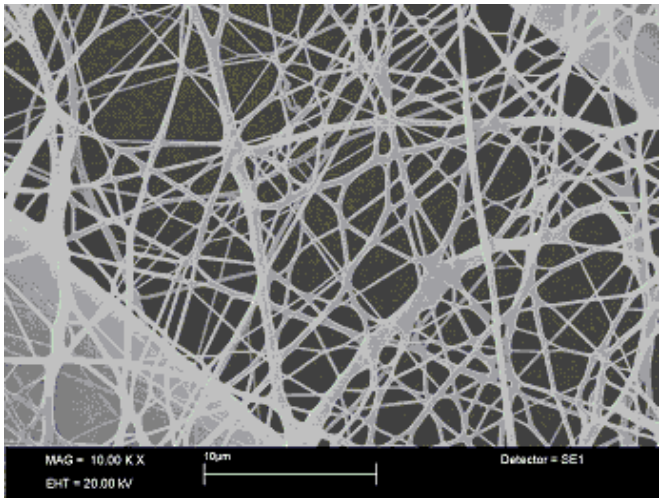

Fig. 4.1 SEM picture of nanofiber filter A (magnification = 10 kX, Leica Stereoscan 440)

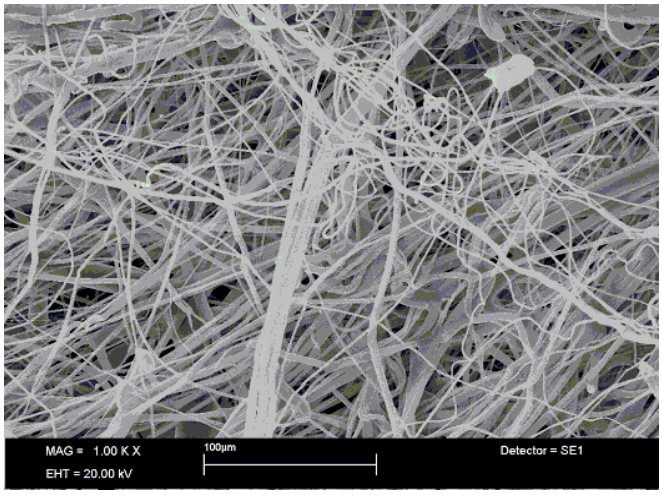

Fig. 4.2 SEM picture of microfiber filter D (magnification = 1 kX, Leica Stereoscan 440)

Figure 4.3 shows the experimental filtration efficiencies of filters A to D as challenged by atomized NaCl aerosol with diameter D_p ranging from 41 to 514 nm at a face velocity of 5 cms^{-1}, together with predictions from Payet's model [34]

introduced in Section 3.2. Experimental filtration efficiency of filter A (d_f = 300 nm, c_f = 0.024) is higher than filter D (d_f = 1.8 μm, c_f = 0.048) for the entire range of D_p. The most penetrating particle size (MPPS) of filters A and D are 103 and 203 nm respectively. The improved filtration efficiency and reduced MPPS of filter A as compared to filter D is attributed to enhanced interception mechanism, implying that nanofiber filter with more surface area per unit volume of fiber is more capable of capturing particles through the mechanism of interception rather than microfiber filter. Experimental MPPS of filters A, B and C are 103, 128 and 143 nm respectively. Again, reduced MPPS and increased filtration efficiency from filters C to A is attributed to enhanced interception mechanism with increasing surface area per unit volume of nanofiber. Figure 4.3 also shows the experimental filtration efficiency of clear substrate is relatively constant at approximately 2 % across particle sizes. In other words, the substrate has no filtration capability other than providing structural support as it is intended.

Besides interception, diffusion is also important to affect the filtration of sub-micron aerosol by nanofibers. Under our test condition, the single fiber efficiency due to diffusion (η_D) decreases from 0.4 to 0.06 from 0.05 to 0.5 μm aerosol, while the single fiber efficiency due to interception (η_R) increases from 0.03 to 0.7 from 0.05 to 0.5 μm aerosol. Since η_D and η_R have the same order of magnitude, they are both important to the overall efficiency. On the other hand, the single fiber efficiency due to inertial impaction (η_I) increases from 1.6×10^{-8} to 1.3×10^{-5} from 0.05 to 0.5 μm aerosol, which is much lower than η_D and η_R, indicating it has negligible effect on

the overall efficiency.

Since filters A to C are formed by coating a nanofiber web on coarse fiber substrate, their theoretical efficiencies as indicated by the solid curves in figure 4.3 are obtained from:

$$\eta_C = 1-(1-\eta_N)(1-\eta_S) \qquad \text{Eq. (4.1)}$$

where η_C is the overall filtration efficiency, η_N and η_S are the filtration efficiencies of nanofiber web and substrate respectively, each determined according to Payet's model [34] introduced in Section 3.2. Kn_f of substrate is 9×10^{-3} (d_f = 14.7 μm), thus the flow over fibers belongs to aerodynamic slip flow regime ($0.001 < Kn_f < 0.25$). Hence, Payet's model built upon Navier-Stokes equation with slip correction is suitable to predict the filtration efficiency of substrate. On the other hand, Kn_f of nanofiber web is 0.44 (d_f = 300 nm), making the flow over fibers transitional (i.e. transition from slip to molecular flow) which is difficult to simulate, and the model is not a physical representation on flow problem in nano-scale. Moreover, the test aerosol is sub-micron in size. It follows that aerosols and fibers are of similar scale and aerosols can no longer be treated as point masses not affecting the flow over fibers, which contradicts with model's assumption. Despite of this, the experimental and theoretical values are still compared to determine the possible deviation. Surprisingly, the model can predict quite accurately the filtration efficiencies of nanofiber filters A to C.

Figure 4.4 compares the quality factor (*QF*) between nanofiber filter (A to C) and

microfiber filter (D). The *QF* of microfiber filter is similar to nanofiber filter for D_p in the range from 50 to 140 nm. From 140 nm onwards, *QF* of microfiber filter goes below nanofiber filter, and the deviation grows with D_p. It shows that microfiber filter is less cost effective than nanofiber filter in filtering larger aerosol (D_p > 120 nm) in the tested sub-micron range.

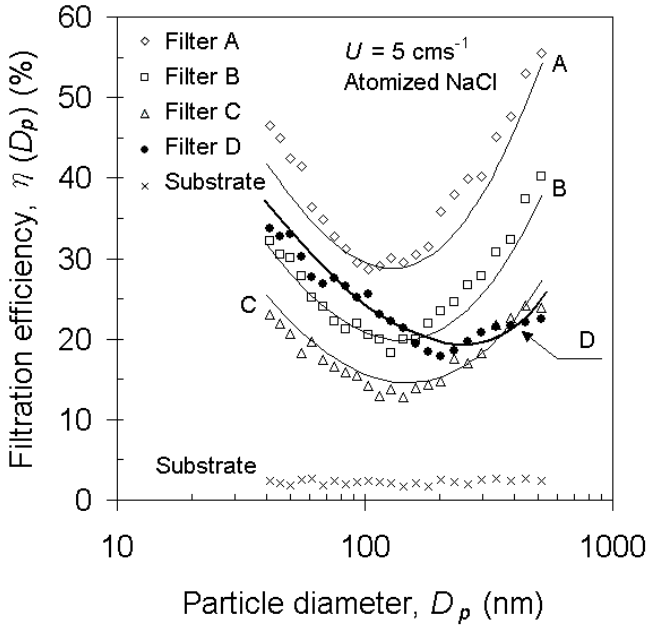

Fig. 4.3 Filtration efficiencies of nanofiber filters A to C and microfiber filter D

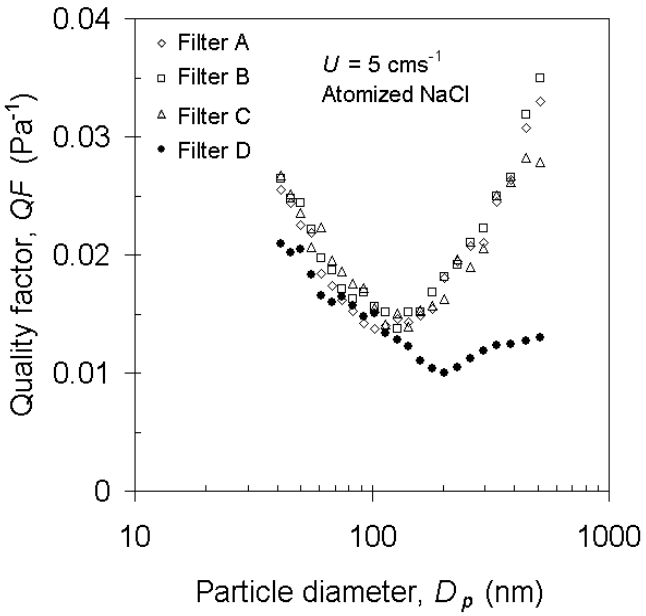

Fig. 4.4 Quality factor of nanofiber filters A to C and microfiber filter D

A quantitative relationship can be drawn from the above findings. Nanofiber filter composed of 300 nm fibers with solidosity from 0.011 to 0.024 has quality factor lies in the range from 0.015 to 0.035, which is higher than microfiber filter composed of 1,800 nm fibers with similar range of solidosity in filtering aerosol larger than 120 nm. To expand the scope of this quantitative relationship such that it can be applied directly to industrial field, nanofiber filters with more choices on fiber diameter and solidosity can be produced by electrospinning method, and used for further investigation.

4.3 Semi-empirical model on pressure drop of loaded filter

In this study, the model on pressure drop ΔP across a loaded fibrous filter is

proposed as:

$$\Delta P = \frac{c_p \Delta P_1 + c_f \Delta P_2}{c_f + c_p} \qquad \text{Eq. (4.2)}$$

c_p is the solidosity of aerosol captured in the filter (deposit) as defined in eq. (4.3), ΔP_1 is the pressure drop across a loaded filter in an idealized condition by treating deposit aligned as fibers (so called deposit fibers) against flow and ΔP_2 is the pressure drop across a loaded filter in another idealized condition assuming deposit enlarge the cross-sectional area of original fibers uniformly.

$$c_p = \frac{M}{\rho_c Z} \qquad \text{Eq. (4.3)}$$

where M is the mass of deposit per unit area and ρ_c is the deposit bulk density, which is usually lower than its material density depending on the packing.

ΔP_1 and ΔP_2 assume idealized deposition patterns that are inappropriate by themselves in describing pressure drop across loaded filter. However, weighted average between these two idealized conditions forms a more applicable model as will be justified by experimental results. It follows that upon continuous aerosol loading, dendrite formation takes place. The dendrites can be treated as obstacles protruded out from fiber surface causing elevated pressure drop. Realistically, as loading continues, deposit contribute to a larger portion of pressure drop than original fibers, analogous to the case of binary filter containing fibers of distinct diameter d_f and d_p with $c_p >> c_f$, rendering pressure drop closer to ΔP_1. By incorporating ΔP_2 into the model, ΔP returns to Davies' empirical formula for describing pressure drop across a clean filter when $c_p = 0$. The derivations of ΔP_1

and ΔP_2 are given below.

Figure 4.5 shows the idealized deposition pattern of ΔP_1 model by treating deposit on each original fiber aligned as three deposit fibers (N = 3) transverse to flow. Drag force (per unit length) acting on a circular fiber in aerodynamic slip regime as given by Pich's [2] hydrodynamic model is:

$$X_i = \frac{4\pi\mu U\left(1+1.996Kn_i\right)}{Ku_i + 0.998Kn_i\left(-\ln c_{il} + c_{il}^2/2 - 1/2\right)} \qquad \text{Eq. (4.4)}$$

i is an index that can be f or p representing parameters of original or deposit fibers respectively, X_i is the drag force per unit length acting on fiber, Kn_i is the Knudsen number of fiber, Ku_i is the Kuwabara hydrodynamic factor as given in eq. (4.5) and c_{il} is the local solidosity in a loaded filter as given in eqs. (4.6) and (4.7).

$$Ku_i = -(\ln c_{il})/2 + c_{il} - c_{il}^2/4 - 3/4 \qquad \text{Eq. (4.5)}$$

$$c_{fl} = (N + 1)c_f \qquad \text{Eq. (4.6)}$$

$$c_{pl} = (N + 1)c_p / N \qquad \text{Eq. (4.7)}$$

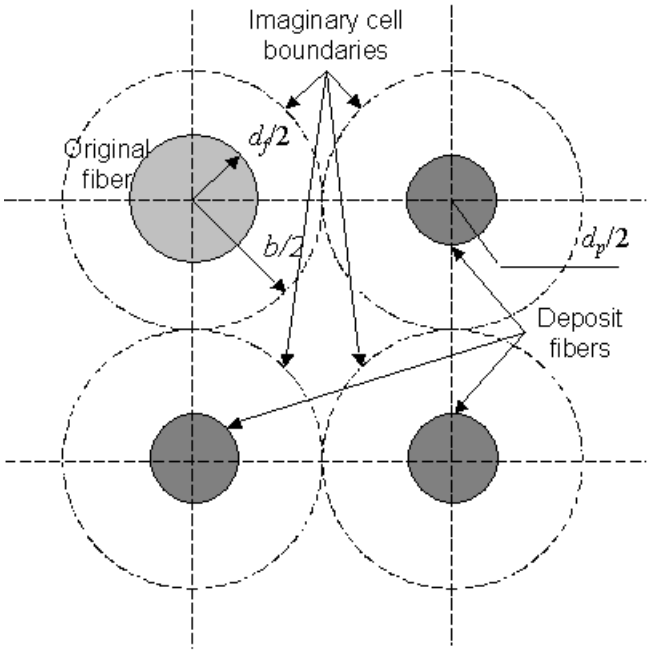

Fig. 4.5 Idealized deposition pattern of ΔP_1 model

Pressure drop Δp_1 for flow over the array of original and deposit fibers as of figure 4.5 becomes:

$$(\Delta p_1) d_f^2 / (4\mu UZ) = 4 c_f K \qquad \text{Eq. (4.8)}$$

$$K = \frac{1 + 1.996 Kn_f}{Ku_f + 0.998 Kn_f \left(-\ln c_{fl} + c_{fl}^2/2 - 1/2\right)} + \frac{N\left(1 + 1.996 Kn_p\right)}{Ku_p + 0.998 Kn_p \left(-\ln c_{pl} + c_{pl}^2/2 - 1/2\right)} \qquad \text{Eq. (4.9)}$$

A realistic non-woven filter contains fibers at random angles against flow should have pressure drop ΔP_1 lower than that of the model filter as depicted in figure 4.5 (i.e. $\Delta P_1 < \Delta p_1$). In addition, eqs. (4.8) and (4.9) derived from cell model approach only suits for highly porous filter. To address these two problems, it can be imagined that pressure drop across a loaded filter described by eqs. (4.8) and (4.9) is equivalent to pressure drop across another model filter composed of fibers transverse

to flow with diameter d_{eq}, solidosity $c_f + c_p$ and Kuwabara hydrodynamic factor Ku_{eq}:

$$\frac{4\mu UZc_f K}{d_f^2} = \frac{4\mu UZ(c_f + c_p)}{d_{eq}^2} \frac{1 + 3.992\lambda/d_{eq}}{Ku_{eq} + 1.996(\lambda/d_{eq})C_{eq}} \qquad \text{Eq. (4.10)}$$

$$Ku_{eq} = -[\ln(c_f + c_p)]/2 + (c_f + c_p) - (c_f + c_p)^2/4 - 3/4 \qquad \text{Eq. (4.11)}$$

$$C_{eq} = -\ln(c_f + c_p) + (c_f + c_p)^2/2 - 1/2 \qquad \text{Eq. (4.12)}$$

To solve for d_{eq}, eq. (4.10) can be re-arranged in dimensionless form:

$$x^3 + \frac{0.998Kn_f C_{eq}}{Ku_{eq}} x^2 - \frac{1 + c_p/c_f}{K(Ku_{eq})} x - \frac{1.996Kn_f(1 + c_p/c_f)}{K(Ku_{eq})} = 0 \qquad \text{Eq. (4.13)}$$

where $x = d_{eq} / d_f$. Eq. (4.13) is in 3rd order of x and can be solved numerically by Newton's method or exactly by Cardano's formula.

If the above model filter with mean fiber diameter d_{eq} and solidosity $c_f + c_p$ becomes a realistic filter having fibers aligned in random angles against flow, its pressure drop ΔP_1 can be estimated from eq. (2.7), thus:

$$(\Delta P_1)d_{eq}^2 / (4\mu UZ) = 16(c_f + c_p)^{1.5}[1 + 56(c_f + c_p)^3] \qquad \text{Eq. (4.14)}$$

Re-arranging gives:

$$\Delta P_1 = 64\mu UZ(c_f + c_p)^{1.5}[1 + 56(c_f + c_p)^3] / (xd_f)^2 \qquad \text{Eq. (4.15)}$$

where x is the solution of eq. (4.13).

Eq. (4.15) is a combination of Pich's [2] hydrodynamic model and Davies' [43] empirical formula. The theoretical applicability range of eq. (4.15) is:

$$\frac{64\lambda^2 c_f ZN\rho_c}{d_f^2} < M < (0.3 - c_f)Z\rho_c \qquad \text{Eq. (4.16)}$$

When $c_p = 0$ and $N = 0$, Ku_p tends to infinity and Ku_{eq} equals to Ku_f. Further when fiber diameter d_f is much larger than λ (i.e. $Kn_f \rightarrow 0$), eq. (4.13) becomes $x^3 - x = 1$ with the solution $x = 1$ or $d_{eq} = d_f$. Under this condition, eq. (4.15) returns to eq. (2.6) for estimating pressure drop across a clean filter. With aerodynamic slip effect making Kn_f not negligible, eq. (4.15) does not return to eq. (2.6) when $c_p = 0$ and $N = 0$. This is because the derivation of ΔP_1 involves re-construction of Kuwabara cells. To overcome this problem, another partial model ΔP_2 is proposed for small c_p.

Figure 4.6 shows the idealized deposition pattern of ΔP_2 assuming deposit enlarge the cross-sectional area of original fibers uniformly, that is:

$$d_{en} = \sqrt{1 + \frac{c_p}{c_f}}\, d_f \qquad \text{Eq. (4.17)}$$

where d_{en} is enlarged fiber diameter and c_p can be expressed in terms of M according to eq. (4.3).

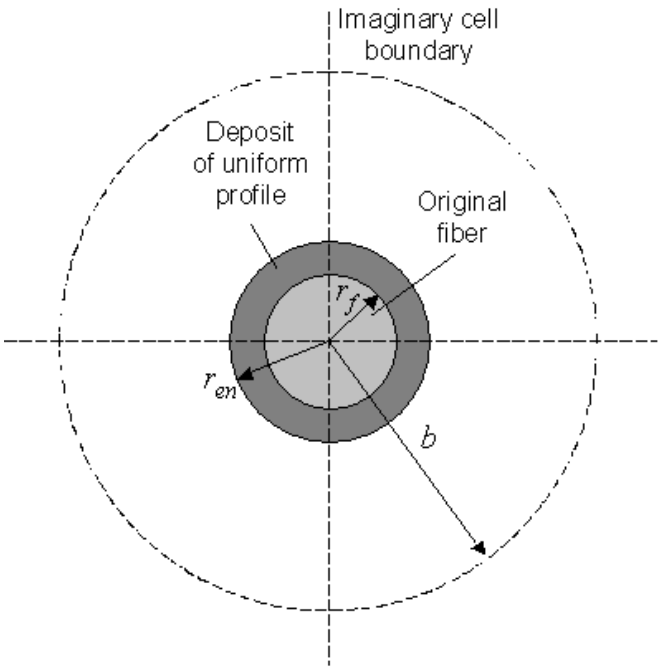

Fig. 4.6 Idealized deposition pattern of ΔP_2 model

For a realistic non-woven filter with mean fiber diameter d_{en} solidosity $c_f + c_p$, pressure drop across the filter can be estimated from eq. (2.6), thus:

$$(\Delta P_2)d_{en}^2 / (4\mu UZ) = 16(c_f + c_p)^{1.5}[1 + 56(c_f + c_p)^3] \qquad \text{Eq. (4.18)}$$

Substitute eq. (4.17) into eq. (4.18) yields:

$$\Delta P_2 = 64\mu UZc_f(c_f + c_p)^{0.5}[1 + 56(c_f + c_p)^3] / d_f^2 \qquad \text{Eq. (4.19)}$$

ΔP_1 and ΔP_2 obtained from eqs. (4.15) and (4.19) respectively will be substituted into eq. (4.2) for modeling pressure drop across a filter (ΔP) under increasing deposit mass ($M = c_p\rho_c Z$). A numerical example demonstrating the difference among ΔP_1, ΔP_2 and ΔP is shown in figure 4.7. As can be seen in the figure at a small deposit mass, ΔP is closer to ΔP_2, while under a large deposit mass, ΔP is closer to ΔP_1. It should be noted when comparing with experimental results later that in the

intermediate range between the small and large deposit mass extremes, none of the expressions ΔP_1 or ΔP_2 provides a satisfactory approximation as with ΔP, which is also within bound between ΔP_1 and ΔP_2 in accordance to eq. (4.2).

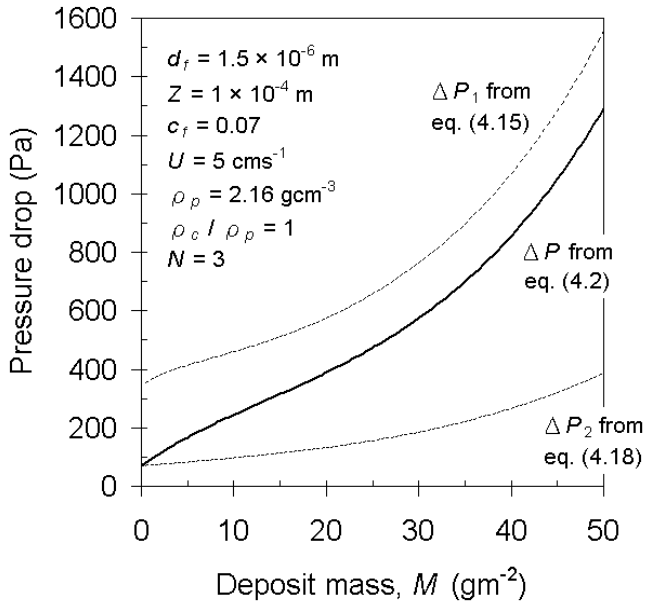

Fig. 4.7 ΔP, ΔP_1 and ΔP_2 as a function of deposit mass

Figure 4.8 shows a filter with higher c_f elevates to higher ΔP under the same deposit mass M according to the semi-empirical model described by eq. (4.2). For two filters with different c_f, their difference in ΔP increases with M. Hence, c_f has to be controlled carefully during production process to avoid excessive rise of ΔP under extended use while the filtration efficiency still meets minimal requirement.

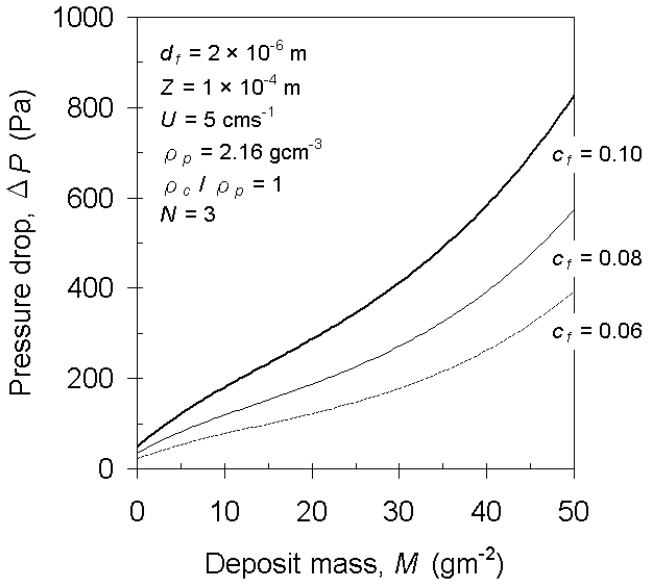

Fig. 4.8 Predicted ΔP across loaded filters with different c_f

Figures 4.9 and 4.10 show the effects of deposit bulk density ρ_c and number of deposit fibers formed for each original fiber N on ΔP across a loaded filter as modeled by eq. (4.2). ρ_c and N represent deposition pattern when the filter is loaded by aerosol stream with different size distribution. Hence, ρ_c and N can be treated as functions of D_p. When the filter is loaded by an aerosol stream of high polydispersity, the deposit can be packed more intact with the smaller aerosol filling up the voids of the matrix formed by larger aerosol results in higher ρ_c (closer to ρ_p) and ΔP increases less rapidly as shown in figure 4.9. Smaller aerosol allows the formation of more but finer deposit fibers results in higher N and ΔP increases more rapidly as shown in figure 4.10. The net effect on ΔP increase rate when the filter is loaded by differently sized aerosol can only be observed through experiments. Experimental results from Song et al. [51] show that pressure drop across a HEPA filter increases more rapidly when the filter is loaded by smaller aerosol. For application purpose, ρ_c

= ρ_p and N = 3 can be used to check for overall agreement between eq. (4.2) and experimental results first, followed by fine tuning on simulation parameters.

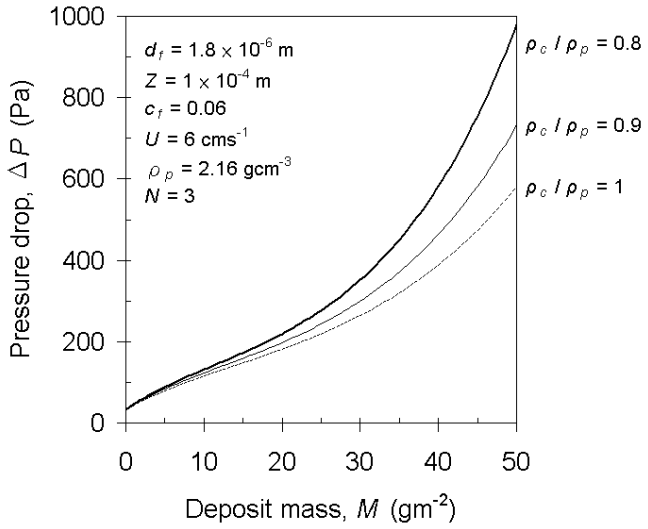

Fig. 4.9 Predicted ΔP across loaded filters with different ρ_c

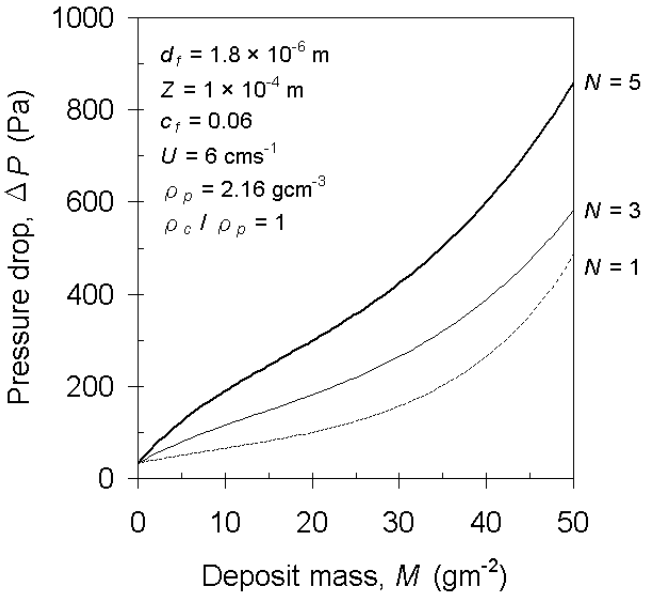

Fig. 4.10 Predicted ΔP across loaded filters with different N

4.4 Filtration efficiency and pressure drop of loaded filter

Section 4.3 explains the trend of predicted ΔP across a loaded filter with respect to increasing M. Experimentally, ΔP is monitored by a different pressure gauge (or other differential pressure measuring devices) throughout the loading process. However, deposit mass M contributed from the sub-micron aerosol captured within the filter is very small and usually under the detection threshold of laboratory electronic balance. Hence, this Chapter will first introduce an indirect method for estimation of M as a value changing with time along the loading process.

The instantaneous deposit mass $M(t)$ can be written as:

$$M(t) = \int_{\tau=0}^{\tau=t} \int_{Dp=0}^{Dp=\infty} n_d(D_p)\eta(D_p,\tau)U\frac{\pi D_p^3}{6}\rho_p d(D_p)d\tau \qquad \text{Eq. (4.20)}$$

where $n_d(D_p)$ is the size distribution of aerosol stream challenging the filter, $dC_{in}(D_p)$ [$= n_d(D_p)d(D_p)$] is the differential concentration of aerosol (expressed in number per unit volume) with size between D_p and $D_p + d(D_p)$, and $\eta(D_p, \tau)$ is the filtration efficiency as a continuous function of particle diameter D_p and time τ.

Experimentally, $\eta(D_p, \tau)$ is sampled at regular time interval ΔT during the loading process by shifting the set-up in figure 2.3 back to the one in figure 2.1 as described in Section 2.2. Frequent sampling of $\eta(D_p, \tau)$ obviously hinders the loading test. If $\eta(D_p, \tau)$ is sampled sparsely, however, one has to assume it remains relatively unchanged between consecutive sample collections which makes the deposit mass data less accurate, i.e.

$$M(t+\Delta T) \approx M(t) + \left[\sum_{i=1}^{i=n} C_{in}(D_{pi}) \eta(D_{pi}, t) U \frac{\pi D_{pi}^3}{6} \rho_p \right] \Delta T \qquad \text{Eq. (4.21)}$$

where $M(t + \Delta T)$ is the deposit mass at time $t + \Delta T$, $M(t)$ is the deposit mass at time t, $C_{in}(D_{pi})$ is the filter upstream aerosol concentration in size bin with log-mean diameter D_{pi} (i = 1, 2, … n where n is the number of scanning channels) and $\eta(D_{pi}, t)$ is the filtration efficiency at particle diameter D_{pi} and time t that is assumed to be constant over the time interval $[t, t + \Delta T]$.

To improve the accuracy of deposit mass data, it becomes necessary to obtain a realistic continuous function of $\eta(D_p, \tau)$ based on available experimental data. Eq. (4.22) is an empirical formula proposed by Davies [21] relating the growth of pressure drop and filtration efficiency of a filter under continuous aerosol loading. It holds only when loading conditions such as aerosol size distribution and face velocity are held constant throughout the loading process.

$$\frac{P(D_p, \tau)}{P(D_p, 0)} = \frac{1 - \eta(D_p, \tau)}{1 - \eta(D_p, 0)} = \gamma_{Dp}^{1-\sqrt{\Delta P(\tau)/\Delta P_0}} \qquad \text{Eq. (4.22)}$$

where $\eta(D_p, \tau)$ and $P(D_p, \tau)$ are the filtration efficiency and aerosol penetration of a loaded filter at particle diameter D_p and time τ whereas those corresponding to $\tau = 0$ represent a clean filter. ΔP_0 and $\Delta P(\tau)$ are the pressure drop across clean and loaded filter respectively. Under continuous aerosol loading, with filtration efficiencies $\eta(D_p, \tau)$ sampled at discrete time interval ΔT and continuous monitoring on pressure drop data $\Delta P(\tau)$, the continuous function of $\eta(D_p, \tau)$ can be secured from least-square estimation (regression coefficient as γ_{Dp}) based on eq. (4.22). Hence, a time step Δt much smaller than experimental sampling interval ΔT can be adopted in eq. (4.21)

for estimation of $M(t)$ along the loading process.

In Section 4.2, the performance of filters A to D in a clean state has been studied experimentally. This Chapter will explore the performance of filters A to D in a loaded state by loading them with polydisperse NaCl aerosol stream with D_p spanning from 41 to 514 nm under a face velocity of 5 cms^{-1}. The pressure drop of filter D (d_f = 1.8 μm, c_f = 0.048) is recorded every 2 hour and its filtration efficiency is sampled every 10 hour. ΔP across clean filter D is measured to be 19.62 Pa when U = 5 cms^{-1}. Figure 4.11 shows the experimental values and polynomial fitted curve of the normalized pressure drop $\Delta P(\tau) / \Delta P_0$. For filter D, $\Delta P(\tau) / \Delta P_0 = 3 \times 10^{-5}\tau^3 - 0.002\tau^2 + 0.12\tau + 1$ with the coefficient of determination R^2 equals to 0.998.

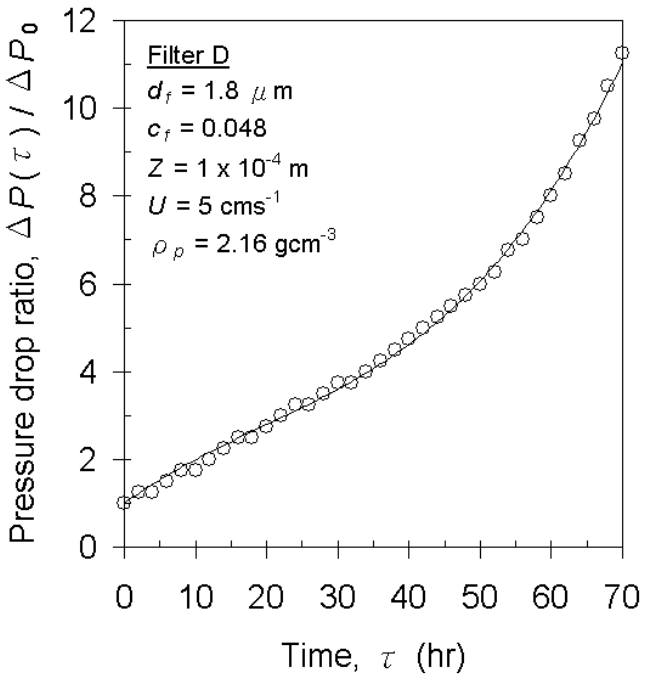

Fig. 4.11 Experimental $\Delta P(\tau) / \Delta P_0$ of loaded filter D and the best-fitted curve as a

3rd order polynomial

Figure 4.12 shows the filtration efficiency of filter D after various loading duration. The MPPS of filter D shifted from 203 to 128 nm after 70 hours of aerosol loading. The variation of filtration efficiency with aerosol size also reduces as a result of continuous aerosol loading.

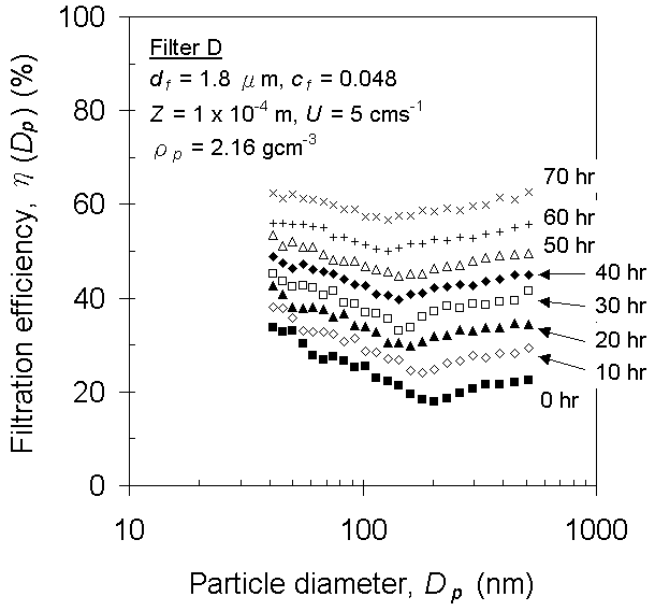

Fig. 4.12 Filtration efficiency of filter D after various loading duration

Figure 4.13 plots the filtration efficiencies of selected particle sizes at 50, 100, 140 and 200 nm against loading duration for finding out the regression coefficient γ_{Dp} of eq. (4.22) using the least-square estimation method. The curves in figure 4.13 are the best-fitted ones in the form of eq. (4.22) for each selected particle size. It can be observed that eq. (4.22) shows three different stages on the rate of increase of

filtration efficiency from an initial fast rate reducing to a medium rate, and increasing back to an ultimate fast rate again. Presumably, this has to do with the process of dendrite formation followed by filter clogging. Normalized regression coefficients $\ln(\gamma_{Dp})$ and corresponding coefficients of determination R^2 are plotted against particle diameter D_p in figure 4.14. Given the high value of R^2, eq. (4.22) is an acceptable empirical formula describing the time change of filtration efficiency under continuous aerosol loading. Realistic continuous functions of $\eta(D_p, \tau)$ for each D_p are thus obtained and $M(t)$ can be estimated from eq. (4.21) using a finer time step Δt much smaller than ΔT. It follows that the total solidosity c is the sum of filter solidosity c_f and deposit solidosity c_p, i.e.

$$c = c_f + c_p = c_f + \frac{M}{\rho_c Z} \qquad \text{Eq. (4.23)}$$

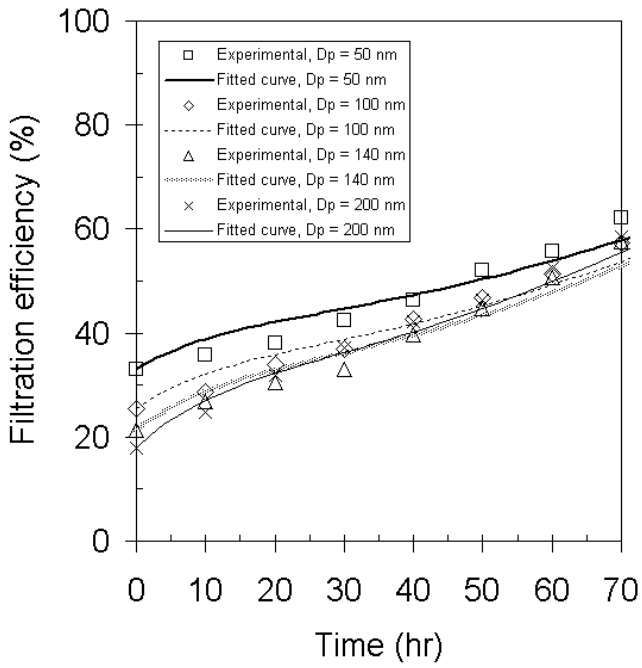

Fig. 4.13 Filtration efficiencies at selected particle sizes against loading duration of

filter D and the best-fitted curves in the form of eq. (4.22)

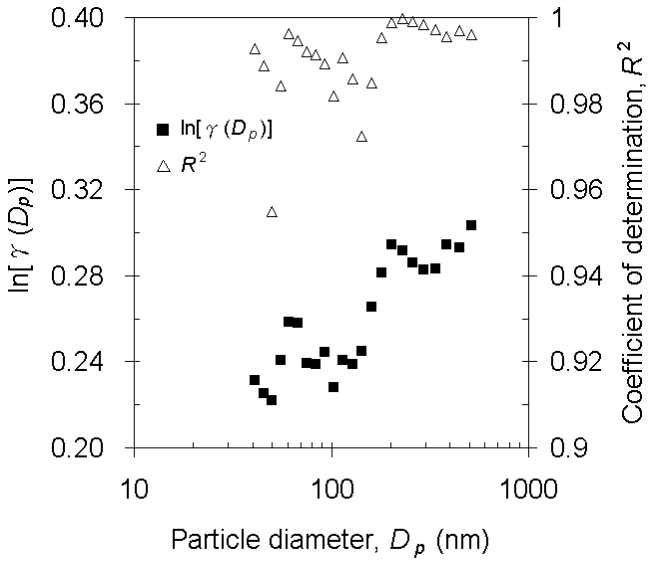

Fig. 4.14 Normalized regression coefficient ln(γ_{Dp}) and corresponding coefficient of determination R^2 against particle diameter D_p of filter D

Figure 4.15 plots the experimental pressure drop against deposit mass of filter D, together with the predicted pressure drop from eq. (4.2). Two of the simulation parameters, namely, number of particle fiber(s) formed for each original fiber N and deposit bulk density ρ_c are not known and thus can be freely adjusted. By substituting N = 3 and ρ_c / ρ_p = 1, eq. (4.2) overestimates the pressure drop while N = 2 and ρ_c / ρ_p = 1 leads to underestimation as deposit mass increases. By using N = 2 and ρ_c / ρ_p = 0.96, the predicted ΔP agrees closely with experimental results up to 41.04 gm^{-2}.

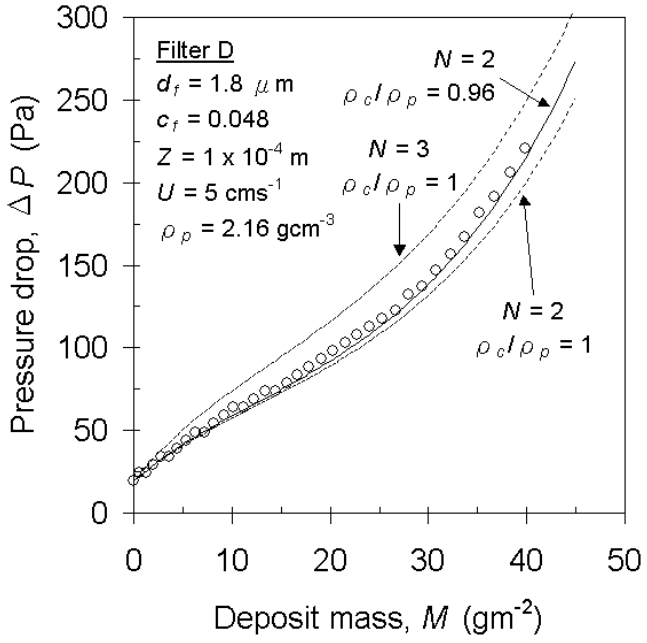

Fig. 4.15 Experimental and predicted pressure drop of filter D under continuous aerosol loading

The pressure drop of filter A (d_f = 300 nm, c_f = 0.024) is recorded every 0.25 hour and its filtration efficiency is sampled hourly. ΔP across clean filter A is 24.53 Pa when U = 5 cms^{-1}. Figure 4.16 shows the experimental values and polynomial fitted curve of the normalized pressure drop $\Delta P(\tau)$ / ΔP_0. For filter A, $\Delta P(\tau)$ / ΔP_0 = $0.10\tau^3 - 0.36\tau^2 + 2.45\tau + 1$ with the coefficient of determination R^2 equals to 0.9998.

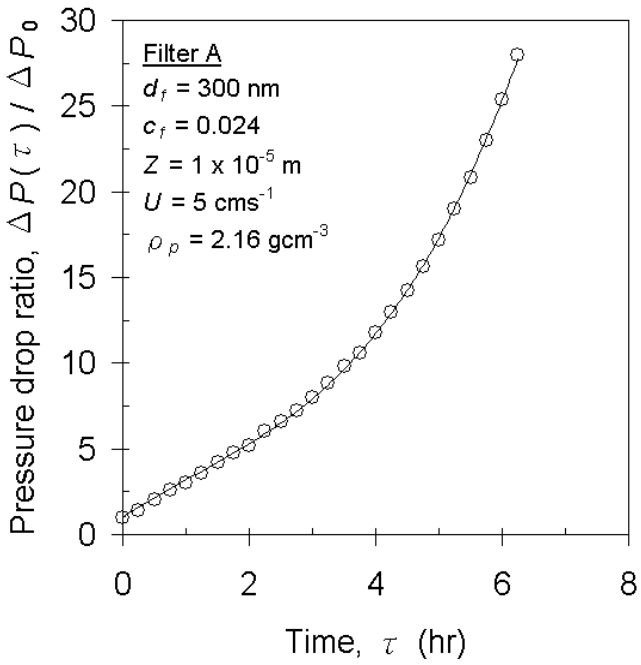

Fig. 4.16 Experimental $\Delta P(\tau) / \Delta P_0$ of loaded filter A and the best-fitted curve as a 3rd order polynomial

Figure 4.17 shows the filtration efficiency of filter A after various loading duration. The MPPS of filter A shifted from 103 to 92 nm after 6 hours of aerosol loading. Similar to microfiber filter (filter D), the variation of filtration efficiency with aerosol size reduces as a result of continuous aerosol loading.

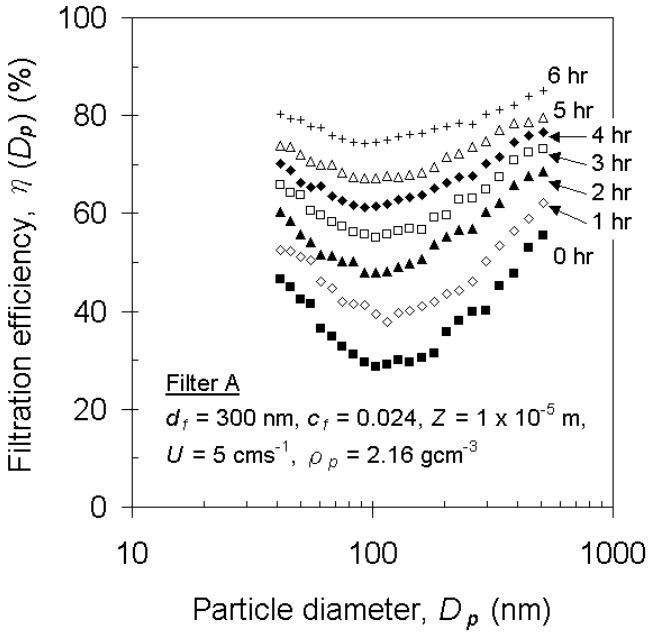

Fig. 4.17 Filtration efficiency of filter A after various loading duration

Figure 4.18 plots the filtration efficiencies of selected particle sizes at 50, 100, 140 and 200 nm against loading duration, together with the best-fitted curves in the form of eq. (4.22) obtained from least-square estimation. Normalized regression coefficients $\ln(\gamma_{Dp})$ and corresponding coefficients of determination R^2 are plotted against particle diameter D_p in figure 4.19. It shows the good fitting of eq. (4.22) even in the case of nanofiber filter (filter A) with d_f equals to 300 nm. The three different rates, i.e. initial fast rate, medium rate, and ultimate fast rate are seen in figure 4.18 but they are less distinct as with the microfiber filter D.

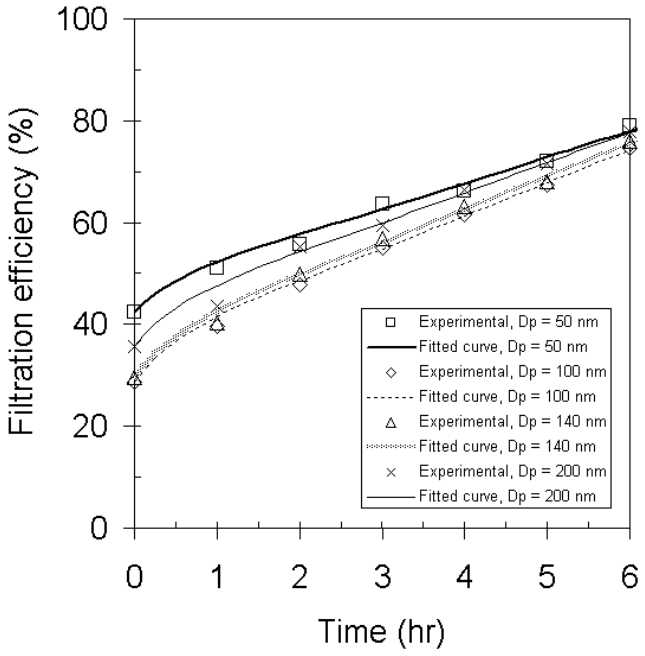

Fig. 4.18 Filtration efficiencies at selected particle sizes against loading duration of filter A and the best-fitted curves in the form of eq. (4.22)

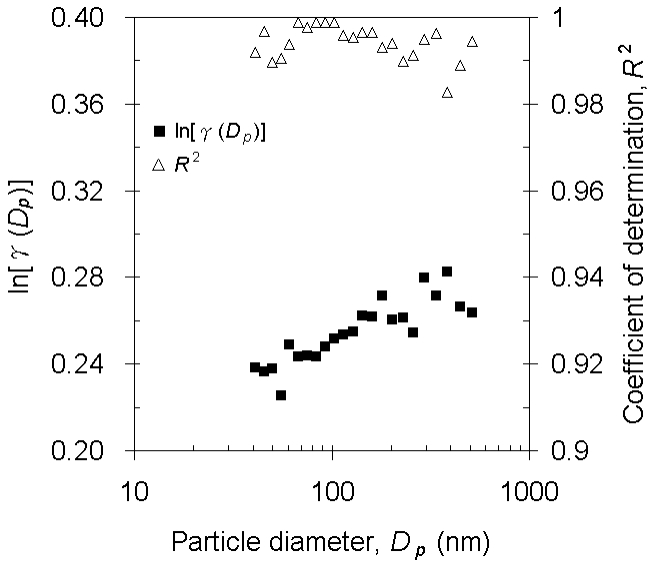

Fig. 4.19 Normalized regression coefficient ln(γ_{Dp}) and corresponding coefficient of determination R^2 against particle diameter D_p of filter A

With γ_{Dp}, $M(t)$ of filter A is estimated in the same way as filter D. Exact procedures are also repeated for filters B and C and figure 4.20 plots the experimental ΔP against M of nanofiber filters A to C, together with the predicted ΔP from eq. (4.2). Both experiment and model suggested that c_f has a decisive effect on pressure drop increase under continuous aerosol loading, at least in the case of nanofiber filters in this study. Since the nanofiber filters A to C are loaded by polydisperse NaCl aerosol stream with size distribution close to that being used to load up microfiber filter D, simulation parameters $N = 2$ and $\rho_c / \rho_p = 0.96$ that offers close agreement in the case of microfiber filter are used again. Predictions from eq. (4.2) generally agree with experimental results up to a deposit mass value of 4.7 gm^{-2}, where filter A starts to show deviation between experimental and predicted ΔP values.

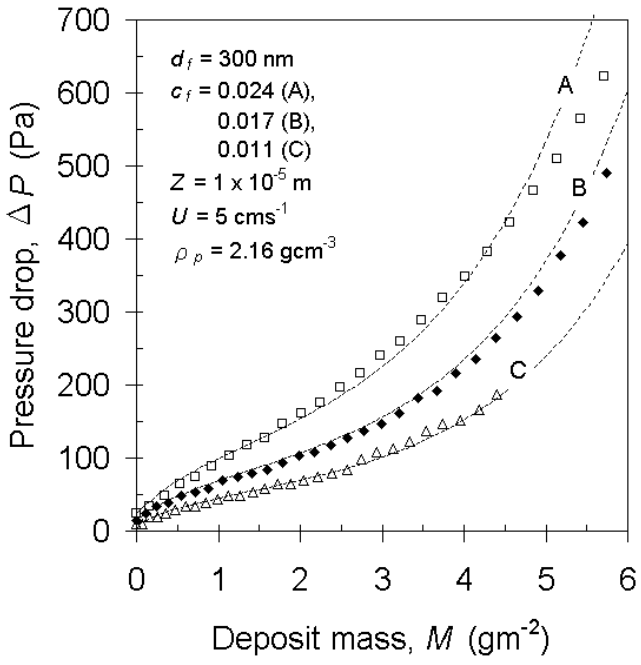

Fig. 4.20 Experimental and predicted pressure drop of filters A to C under

continuous aerosol loading

By comparing figures 4.15 and 4.20, it can be observed that the nanofiber filters have pressure drop rises more rapidly than microfiber filter. Morever, figure 4.21 compares the change of MPPS among filters A to D under continuous aerosol loading, where deposit solidosity c_p as calculated from eq. (4.3) represents the degree of loading. The MPPS of filters A, B and C shifted down slightly from 103, 128 and 143 nm to 92, 103 and 103 nm respectively; however, the MPPS of filter D shifted down from 203 to 128 nm at similar degree of loading. The MPPS of microfiber filter decreases at a faster rate than nanofiber filters. Moreover, the MPPS of microfiber filter decreases monotonically, which is not observed for nanofiber filters. The entirely different loading characteristics between nanofiber and microfiber filters are related to the distribution of deposit (i.e. deposition profile) across filter depth, which will be discussed in Chapter 5.

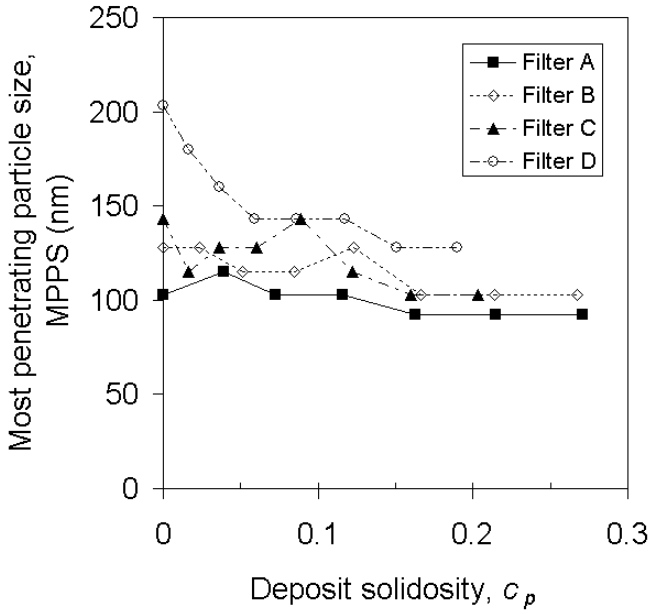

Fig. 4.21 Change of MPPS of filters A, B, C and D under continuous aerosol loading

4.5 Chapter conclusions

Filtration efficiency and pressure drop of nanofiber and microfiber filters at both clean and loaded state have been studied in this Chapter. Decrease of MPPS under continuous aerosol loading is observed for both types of filters. At similar degree of loading based on deposit solidosity c_p, the shift of MPPS of nanofiber filter is larger than microfiber filter. Clean nanofiber filter (filter A: d_f = 300 nm, c_f = 0.024) offers higher filtration efficiency and quality factor than its microfiber counterpart (filter D: d_f = 1.8 μm, c_f = 0.048) does not necessarily imply that nanofiber is "absolutely better" than microfiber filter. As observed from the loading experiment (Section 4.4), also supported by the semi-empirical model (Section 4.3), the pressure drop of nanofiber filter rises more rapidly than microfiber filter. Hence, the relatively low

dust holding capacity is regarded as a weakness to nanofiber filter, as it leads to frequent filter replacement during extended use. Moreover, the pressure drop increase rate of nanofiber filter is very sensitive to its filter solidosity c_f. The semi-empirical model on pressure drop across a loaded fibrous filter thus becomes a useful tool in filter design, and its predictions show agreement with experimental results. The next phase of this study will be to investigate two possible ways to utilize the strength of nanofiber filter at clean state (high filtration efficiency and quality factor) and avoid its shortcomings at loaded state (low dust holding capacity). One way is to install a microfiber filter upstream to nanofiber filter as a pre-filter to screen out part of the aerosol stream hence reduces the loading on nanofiber filter. This method will be studied in Chapter 5. Another way is to regenerate the filter by backflow of pressurized air jet after certain time of loading, and this method will be investigated in Chapter 6. Chapter 5 also includes a modified model on deposition profile across the depth of a filter under polydisperse aerosol loading, which helps to further explain the different loading characteristics between nanofiber and microfiber filters.

Chapter 5

Filtration behavior of filter composed of dual-layers including a nanofiber layer

5.1 Chapter introduction

In Section 2.1, it has been mentioned that filter quality mainly depends on filtration efficiency and pressure drop. In order to improve filter quality, filter media should be highly permeable (i.e. low pressure drop) while still have filtration efficiency above the level as required by environmental standards or end-users. In Section 4.2, it has been discovered that nanofiber filter offers higher filtration efficiency and quality factor than microfiber filter at a clean state, which may suggest the former "absolutely" better than the latter under most working conditions. However, Section 4.4 shows that under continuous loading of sub-micron solid aerosol, pressure drop across nanofiber filter rises at a much faster rate than microfiber filter. It reflects the lower dust holding capacity of nanofiber filter and practically requires frequent filter regeneration by backflow of compressed air [52], thus leading to higher energy consumption and increased chance of destroying the fragile nanofibers by the air jet. To reduce the pressure drop increase rate of nanofiber filter media, it is proposed in Section 4.5 that a microfiber filter can be placed upstream to nanofiber filter forming an inhomogeneous dual-layer filter. Gradoń et al. [20], Podgórski et al. [19] and Podgórski [17] have found that a dual-layer filter with nanofibers placed upstream to microfibers has significantly increased efficiency at the MPPS and improved quality factor as compared to conventional microfiber filters at a clean state. Their studies

confirmed that a filter composed of dual-layers including a nanofiber layer keeps the advantage of nanofibers. It is then worth to investigate the effectiveness of this inhomogeneous dual-layer filter on improving the dust holding capacity of nanofiber media, which will be the focus of Chapter 5.

The loading characteristics of inhomogeneous filters (also homogeneous ones) largely depend on their deposition profile across filter depth. From a semi-empirical approach, Brown and Wake [28], also Podgórski [29], have proposed the concept of linear loading within a filter slice to predict the deposition profile across the depth of a homogeneous fibrous medium loaded with aerosol of single size. Their predictions show agreement to efficiency test results. However, the situation complicates in this study when the inhomogeneous dual-layer filters are challenged by polydisperse aerosol. Hence, the approach from Brown and Wake [28] and Podgórski [29] will be modified in the present work. The assumptions and shortcomings of this approach will be addressed subsequently. Since the deposition model is semi-empirical, experimental results of constituent filter layers presented in Chapter 4 are used to determine all necessary empirical constants, one of which is the filtration efficiency raising factor [30].

5.2 Filtration efficiency and quality factor of clean dual-layer filter

Filters A, C and D studied in Chapter 4 are stacked up as dual-layer filters E, F and G as depicted in figure 5.1. Filters E and F contain identical microfiber and

nanofiber layers in reversed arrangement, hence they have equal thickness, pressure drop and filtration efficiency in clean state. Filter G is also an inhomogeneous dual-layer filter, but its nanofiber layer has a gradient packing density by stacking filters A and C, with the more porous (i.e. lower c_f) layer C upstream to the less porous (i.e. higher c_f) layer A.

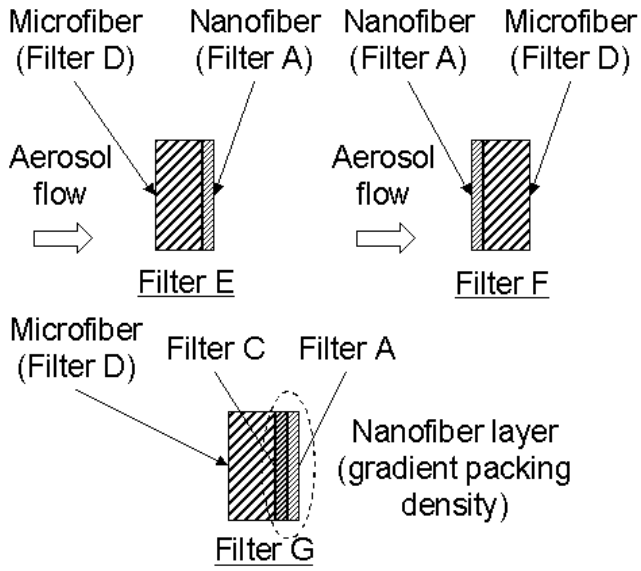

Fig. 5.1 Stacking of constituent filter layers within the dual-layer filters E, F and G

The filtration efficiencies of filters F and G are depicted in figure 5.2 (filters A and D as reference). The MPPS of filter F is 160 nm, which lies between that of filters A (103 nm) and D (203 nm). Filter F is formed by stacking nanofiber and microfiber filters, with nanofiber facing upstream. This arrangement is identical to the dual-layer filter that has been studied thoroughly by Gradoń et al. [20] and Podgórski et al. [19], and their findings on increased efficiency and reduced MPPS of dual-layer filter as compared to conventional microfiber filters agree with our

results. The MPPS of filter G is 140 nm that is further below filter F due to the presence of an extra nanofiber layer (filter C). However, this extra nanofiber layer only provides slight efficiency improvement over the range from 70 to 200 nm.

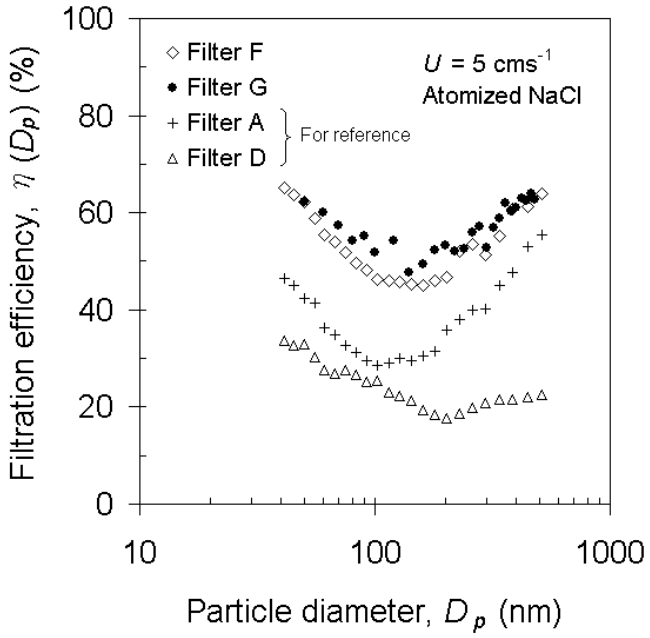

Fig. 5.2 Filtration efficiencies of dual-layer filters F and G

Figure 5.3 shows the quality factor (*QF*) of clean dual-layer filters F and G (filters A and D as reference). Although stacking up nanofiber and microfiber filters provides higher efficiency, it incurs excess pressure drop. The trade-off is clearly indicated in figure 5.3 where *QF* of filter F is lower than that of filter A, especially for particles larger than 300 nm. Although filter G with an extra nanofiber layer has *QF* consistently below filter F, it eventually shows higher dust holding capacity in Section 5.3.

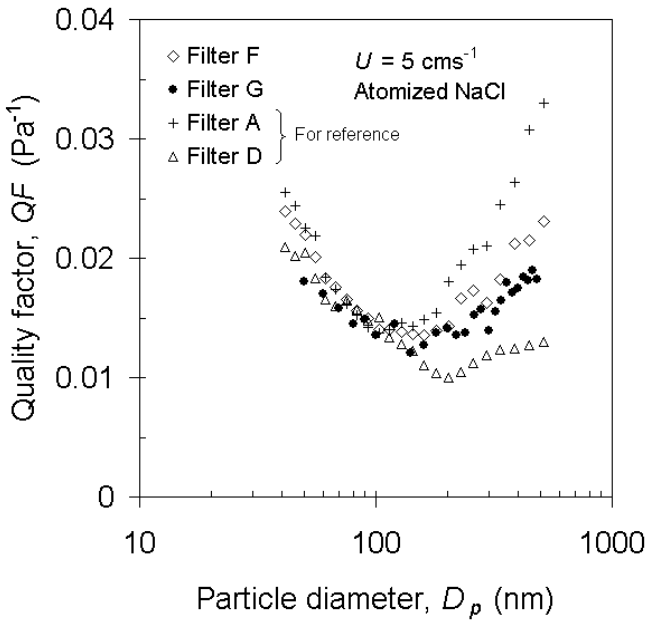

Fig. 5.3 Quality factors of dual-layer filters F and G

5.3 Semi-empirical model on deposition profile with polydisperse aerosol

By assuming the mass efficiency of a filter slice being linearly related to the deposit mass as a first approximation, Brown and Wake [28] and Podgórski [29] have derived an expression on the deposition profile of a homogeneous fibrous filter under continuous loading of single size aerosol. It should be noted that mass efficiency refers to the ratio between mass of collected aerosol and mass of challenging aerosol, and is equivalent to filtration efficiency defined by eq. (2.1) only in the case of single size aerosol. When an inhomogeneous dual-layer filter is loaded continuously by polydisperse aerosol, the expression can still be used to estimate the deposition profile of upstream layer, but not the case for downstream layer due to the size distribution of aerosol stream leaving the upstream layer

changing with time with consequence of an unsteady inlet condition in the downstream layer. As a start, the expression on deposition profile as obtained by Brown and Wake [28] and Podgórski [29] will be adopted, followed by deriving an equation for solving the filtration efficiency raising factors. Using the filtration efficiency raising factors, the size distribution of aerosol stream leaving the upstream layer will be determined subsequently. The deposition profile of downstream layer can be estimated accordingly.

The expressions on mass concentration $C_m(x, t)$ and deposition profile $K(x, t)$ (i.e. deposit mass per unit volume) across filter depth (x) after loading for t units of time, obtained by Brown and Wake [28] and Podgórski [29], are given as follows:

$$C_m(x,t) = \frac{C_{m0}}{\{1+\exp(\alpha_0 U C_{m0} t/K_0)[\exp(\alpha_0 x)-1]\}} \qquad \text{Eq. (5.1)}$$

$$K(x,t) = \frac{K_0[\exp(\alpha_0 U C_{m0} t/K_0)-1]}{\{1+\exp(\alpha_0 U C_{m0} t/K_0)[\exp(\alpha_0 x)-1]\}} \qquad \text{Eq. (5.2)}$$

where C_{m0} is the mass concentration of aerosol stream at filter inlet assuming steady throughout the loading process, U is the face velocity, α_0 is the initial mass efficiency of a filter slice per unit length, and K_0 is the deposit mass per unit volume that causes the mass efficiency of the filter slice to be doubled from its initial value (i.e. $2\alpha_0\Delta x$ and Δx is the thickness of a filter slice).

Substitute $x = Z$ (where Z is the filter thickness) into eq. (5.1), it can be re-written as:

$$\ln\left[\frac{1}{P_m(t)}-1\right] = \beta_0 + \beta_1 t \qquad \text{Eq. (5.3)}$$

where $P_m(t)$ is the mass penetration of the filter defined as $C_m(Z, t) / C_{m0}$, $\beta_0 = \ln[\exp(\alpha_0 Z) - 1]$, and $\beta_1 = \alpha_0 U C_{m0} / K_0$. To determine β_0 and β_1 (hence α_0 and K_0), $P_m(t)$ is sampled at regular time interval during the loading test (experiment set-up shown in figure 2.3) , followed by performing linear regression analysis on the data. Eq. (5.2) yields the deposition profile $K(x, t)$ once α_0 and K_0 are known.

While K_0 is regarded as the constant relating mass efficiency and deposit mass, the filtration efficiency raising factor $\Lambda(D_p)$ is regarded as the constant relating filtration efficiency for a given particle diameter D_p and deposit mass. Analogous to K_0, $\Lambda(D_p)$ has to be determined empirically from filtration efficiencies $\eta(D_p, t)$ sampled at regular time interval during the loading process. Suppose the filter is partitioned into N slices along its thickness (i.e. $\Delta x = Z / N$), $\eta(D_p, t)$ and the filtration efficiency of each slice in the filter $\eta_{sl}(D_p, x_i, t)$ are related by eq. (5.4):

$$1 - \eta(D_p, t) = \prod_{i=0}^{N-1} \left[1 - \eta_{sl}\left(D_p, x_i, t\right)\right] \qquad \text{Eq. (5.4)}$$

$\eta_{sl}(D_p, x_i, t)$ is assumed to increase linearly with $K(x_i, t)$:

$$\eta_{sl}\left(D_p, x_i, t\right) = \eta_{sl}\left(D_p, 0\right)\left[1 + \Lambda\left(D_p\right) K\left(x_i, t\right)\right] \qquad \text{Eq. (5.5)}$$

where $\eta_{sl}(D_p, 0)$ is the filtration efficiency of a slice in the clean filter, which is derived from eq. (5.4) with $t = 0$.

Substitute eq. (5.5) into eq. (5.4) yields:

$$P\left(D_p, t\right) = \prod_{i=0}^{N-1} \left[P_{sl}\left(D_p, 0\right) - \eta_{sl}\left(D_p, 0\right) K\left(x_i, t\right) \Lambda\left(D_p\right)\right] \qquad \text{Eq. (5.6)}$$

where $P(D_p, t)$ is the aerosol penetration defined as $1 - \eta(D_p, t)$, and $P_{sl}(D_p, 0)$ is the aerosol penetration across a slice in the clean filter defined as $1 - \eta_{sl}(D_p, 0)$. As stated, $\eta(D_p, t)$ is measured at regular time interval during the loading process and $K(x_i, t)$ is calculated from eq. (5.2), the only unknown left undetermined in eq. (5.6) is $\Lambda(D_p)$ that can be obtained by the method of least-square estimation:

$$\frac{d}{d\Lambda}\sum_k\left\{P\left(D_p,t_k\right)-\prod_{i=0}^{N-1}\left[P_{sl}\left(D_p,0\right)-\eta_{sl}\left(D_p,0\right)K\left(x_i,t_k\right)\Lambda\right]\right\}^2=0 \qquad \text{Eq. (5.7)}$$

The intermediate form of eq. (5.7) is:

$$f(\Lambda)=\sum_k\left\{P\left(D_p,t_k\right)-\prod_{i=0}^{N-1}\left[P_{sl}\left(D_p,0\right)-\eta_{sl}\left(D_p,0\right)K\left(x_i,t_k\right)\Lambda\right]\right\}\left\{\sum_{i=0}^{N-1}\prod_{j=0}^{N-1}\left[P_{sl}\left(D_p,0\right)I_{ij}-\eta_{sl}\left(D_p,0\right)K\left(x_i,t_k\right)\Lambda^{Iij}\right]\right\}=0 \qquad \text{Eq. (5.8)}$$

where $I_{ij} = 0$ when $i = j$ and 1 when $i \neq j$. Secant method was used to solve eq. (5.8) to circumvent the complication of evaluating the derivative of $f(\Lambda)$.

After obtaining $\Lambda(D_p)$ of constituent filter layers, the deposition profile $K(x, t)$ of an inhomogeneous dual-layer filter is predicted from the following approach:

$$C\left(D_p, x+\Delta x, t\right)=C\left(D_p, x, t\right)\left[1-\eta_{sl}\left(D_p, x, t\right)\right] \qquad \text{Eq. (5.9)}$$

where $C(D_p, x, t)$ is the number concentration of size D_p particle at filter depth x and time t. $C(D_p, 0, t)$ is the size distribution of challenge aerosol, which is maintained steady and monitored throughout the loading process. $\eta_{sl}(D_p, x, 0)$ is the filtration efficiency of a slice within the clean filter that can be derived from eq. (5.4). Hence, $C(D_p, 0, t)$ and $\eta_{sl}(D_p, x, 0)$ are, respectively, the boundary and initial conditions of eq. (5.9). Assume the thickness of upstream and downstream layers are Z_1 and Z_2

respectively, $C(D_p, Z_1, t)$ represents both the size distribution of aerosol stream leaving the upstream and entering the downstream layers, while $C(D_p, Z_1 + Z_2, t)$ is the size distribution of aerosol stream leaving the downstream layer.

The deposition profile $K(x, t)$ is then estimated according to eq. (5.10):

$$K(x,t+\Delta t) = K(x,t) + \sum_{Dp} \frac{C(D_p,x,t)\eta_{sl}(D_p,x,t)\pi D_p^3 \rho_p U(\Delta t)}{6(\Delta x)} \qquad \text{Eq. (5.10)}$$

where ρ_p is the particle density. The initial condition $K(x, 0)$ is the deposit mass per unit volume within a clean filter, which is equal to zero. Eq. (5.10) gives the deposition profile at time $t + \Delta t$. To proceed along time, $K(x, t + \Delta t)$ is substituted into eq. (5.5) for getting $\eta_{sl}(D_p, x, t + \Delta t)$. The steps starting from eq. (5.9) are repeated in order to obtain the time evolution of deposition profile.

By integrating $K(x, t)$ along filter thickness Z, the deposit mass per unit filter area $M(t)$ can be obtained:

$$M(t) = \int_0^Z K(x,t)dx \qquad \text{Eq. (5.11)}$$

When $M(t)$ is divided by $\rho_p Z$, it gives $c_p(t)$ as the deposit solidosity:

$$c_p(t) = \frac{M(t)}{\rho_p Z} \qquad \text{Eq. (5.12)}$$

5.4 Filtration efficiency and pressure drop of loaded dual-layer filter

We have seen in Chapter 4 that the nanofiber filters A, B and C clog up faster than

microfiber filter D. Further, nanofiber filter of higher solidosity (c_f) has pressure drop that rises more rapidly. These loading characteristics are related to the distribution of aerosol deposit, i.e. deposition profile, across filter depth. The deposition profile $K(x^*, t)$ of filters A to D under a deposit mass (M) of 4 gm^{-2} as estimated from the model described by eq. (5.2) is shown in figure 5.4. x^* (= x / Z, where Z is the filter thickness) is used instead of x because filter D has thickness 10 times to that of filters A to C. As depicted in figure 5.4, aerosol deposit is distributed much more evenly across the depth of microfiber filter D than nanofiber filters A to C. Comparing with figures 4.15 and 4.20, this uniform deposition profile leads to the much lower pressure drop increase rate of filter D. Hence, a nanofiber filter having higher filtration efficiency and quality factor than microfiber filter at clean state (e.g. filter A outperforms filter D as indicated by figures 4.3 and 4.4) does not suggest it to be the "absolutely" better filter. On the other hand, microfiber filters, by virtue of increased fiber diameter, are usually made thicker in order to achieve high filtration efficiency. The increased thickness facilitates dust holding, while a thin layer of nanofibers cannot achieve this objective. Among the nanofiber filters, filter C with the lowest c_f (0.011) shows the most uniform deposition profile, while filter A with the highest c_f (0.024) has the steepest deposition profile across filter depth. Hence, filter C has lower pressure drop increase rate than filter A. As evident in figure 4.20, despite ΔP across filters A, B and C at clean state are at their low values – 24.53, 14.72 and 9.81 Pa respectively, ΔP across filters A, B and C loaded with 4 gm^{-2} deposit becomes large – 348, 235 and 142 Pa respectively. It indicates that the increased flow resistance incurred by less porous nanofiber filter may not suit for

long service due to the increased fiber length per unit volume, which means an increased number of sites for aerosol deposition. Hence, loading characteristics such as pressure drop increase rate should be considered in filter design and selection, especially when nanofibers are used. While it is more significant for nanofiber filter and much less for microfiber filter, deposition profile is steep at face region (i.e. skin layer) and becomes moderate towards back region. This skin layer contributes to most of the flow resistance across a loaded filter.

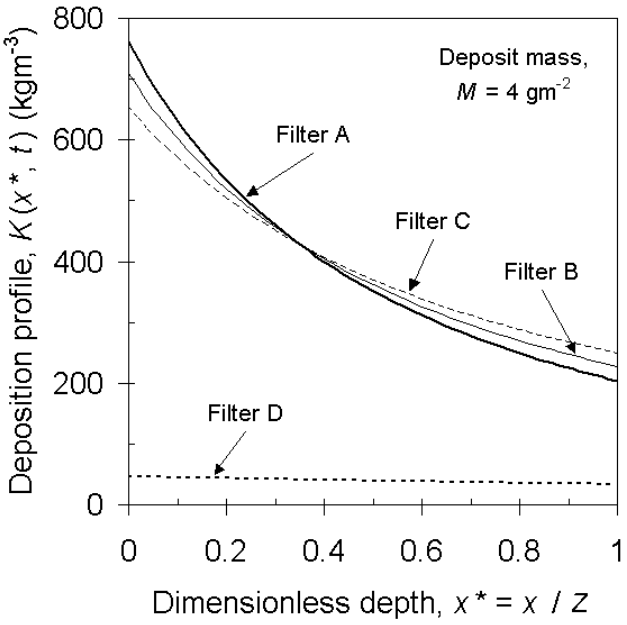

Fig. 5.4 Deposition profile of filters A, B, C and D after collected 4 gm^{-2} deposit

In order to validate the semi-empirical model developed in Section 5.3, filter A has been loaded by polydisperse aerosol in three different size distributions as shown in figure 5.5 (square dots). Empirical terms α_0, K_0 and $\Lambda(D_p)$ as determined from loading test under distribution 2 are used to predict the filtration efficiencies under

distributions 1 (higher concentration, smaller mode) and 3 (lower concentration, larger mode) using the newly developed model. Figure 5.6 shows the experimental and predicted efficiency at 100 nm particles. It can be seen that as loading continues, the semi-empirical model (line) slightly under-estimate the filtration efficiency (dots). However, the degree of under-estimation should be acceptable by considering the simplicity of the model.

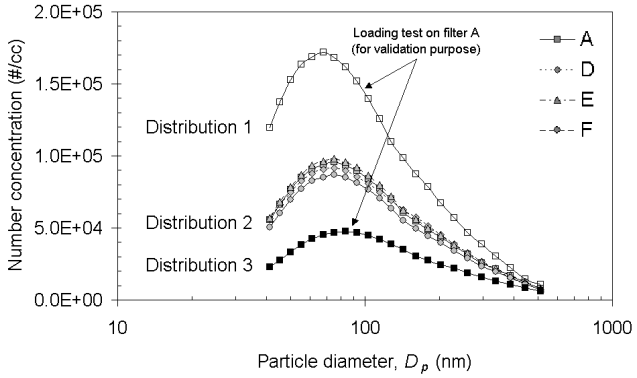

Fig. 5.5 Size distribution of aerosol stream loading up filters A, D, E and F

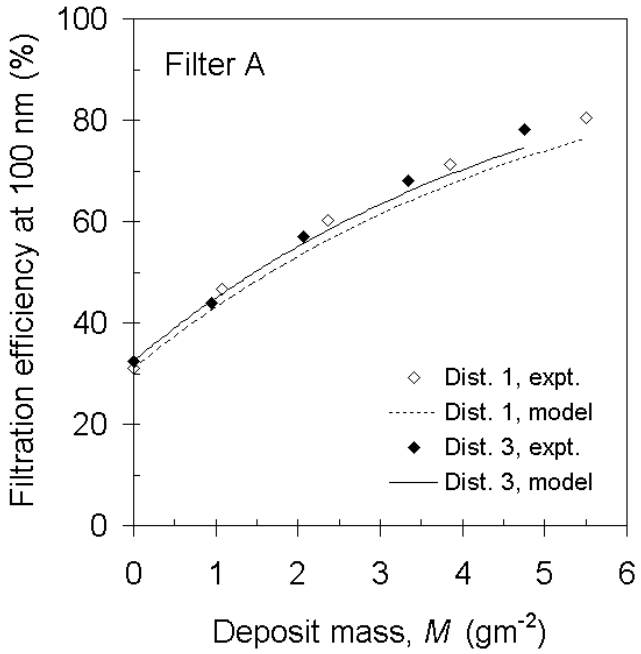

Fig. 5.6 Validating the semi-empirical model on deposition profile with polydisperse aerosol

The filter layers are stacked to form the dual-layer filters as shown in figure 5.1. Filter E is formed by placing filter D upstream to filter A, aiming to relieve clogging in nanofiber layer, especially skin region, by utilizing the dust holding capacity of microfiber layer. Filter F serves as a control by placing filter A upstream to filter D, such that filters E and F have the same thickness, filtration efficiencies and pressure drop at clean state. The dual-layer filters have undergone the same series of loading tests and their filtration efficiencies are depicted in figures 5.7 and 5.8. $M_A(t)$ and $M_D(t)$ are the deposit mass in filter layers A and D respectively as obtained by eq. (5.11), while $c_{pA}(t)$ and $c_{pD}(t)$ are the deposit solidosity in corresponding filter layers as obtained by eq. (5.12). At a first glance, filter E facilitates even distribution of deposit among microfiber and nanofiber layers, with $M_A(t)$ and $M_D(t)$ equal to 4.23

and 2.06 gm^{-2} after loaded for 6 hours. In contrast, filter F has the major portion of deposit being collected in its nanofiber layer, with $M_A(t)$ and $M_D(t)$ equal to 5.00 and 0.23 gm^{-2} after loaded for 6 hours. For dual-layer filter, the shift of MPPS after loading is not as obvious as microfiber filter (filter D, figure 4.12). The sensitivity of filtration efficiency on particle diameter reduces as a result of loading. Figure 5.9 shows the elevation of pressure drop across loaded dual-layer filters. ΔP across filter E increases slower than filter F, first of all because microfiber layer in filter E helps to collect part of the challenging aerosol, thus reduces the loading and curtail the pressure drop elevation of downstream nanofiber layer. In contrast, filter F has its nanofiber layer under direct challenge of aerosol stream, where it clogs up rapidly.

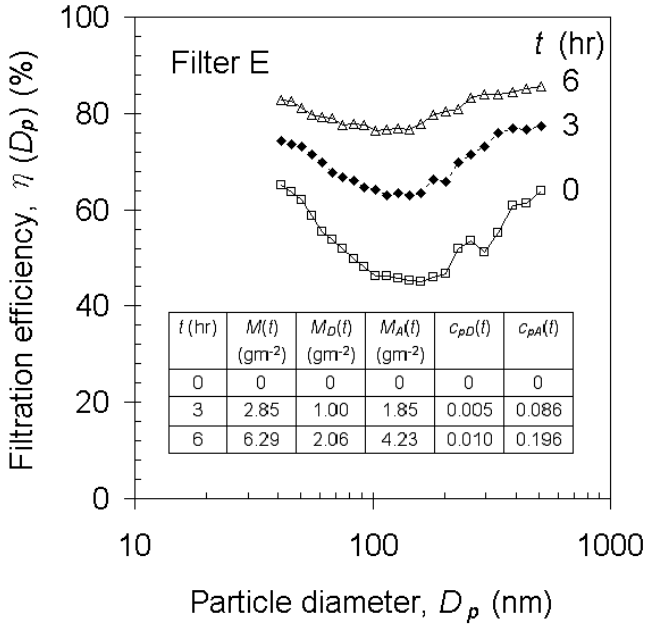

t (hr)	M(t) (gm-2)	MD(t) (gm-2)	MA(t) (gm-2)	cpD(t)	cpA(t)
0	0	0	0	0	0
3	2.85	1.00	1.85	0.005	0.086
6	6.29	2.06	4.23	0.010	0.196

Fig. 5.7 Filtration efficiency of filter E after various loading duration

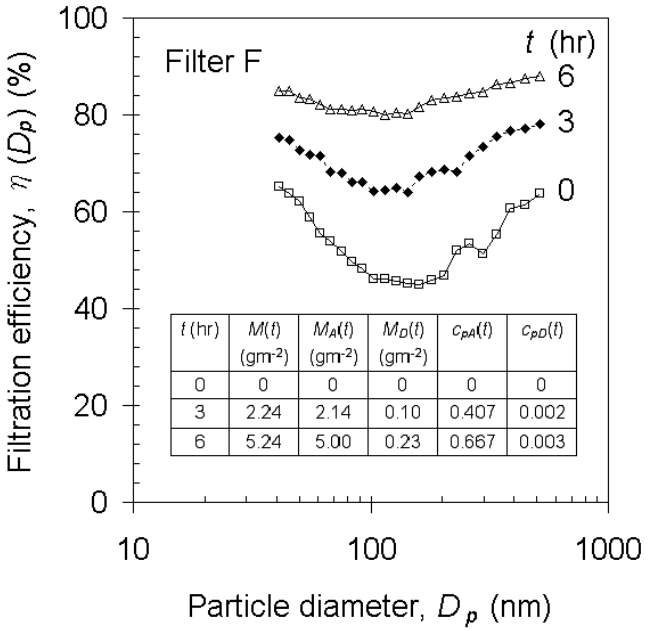

t (hr)	M(t) (gm-2)	MA(t) (gm-2)	MD(t) (gm-2)	cpA(t)	cpD(t)
0	0	0	0	0	0
3	2.24	2.14	0.10	0.407	0.002
6	5.24	5.00	0.23	0.667	0.003

Fig. 5.8 Filtration efficiency of filter F after various loading duration

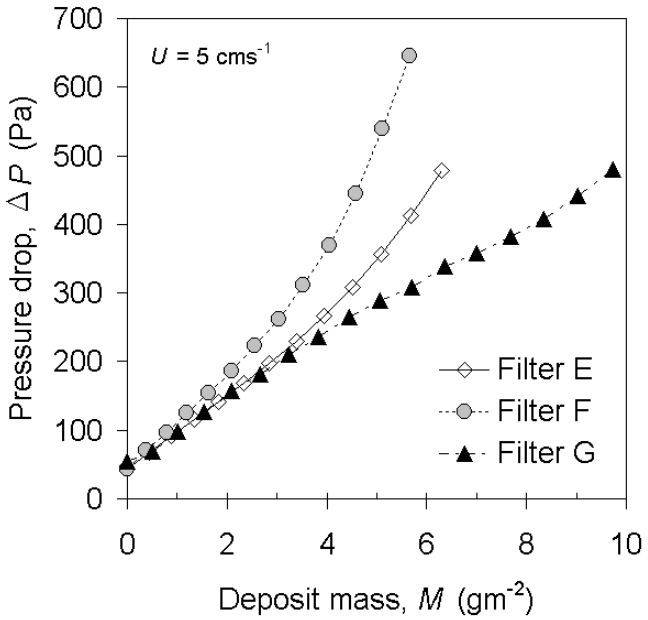

Fig. 5.9 Experimental pressure drop of filters E, F and G under continuous aerosol loading

Deposition profile within individual layers also contributes to the distinct pressure drop increase rate between dual-layer filters E and F. Figure 5.10 compares the deposition profile $K(x^*, t)$ between filters E and F when $M(t)$ [= $M_A(t) + M_D(t)$] is at 5 gm^{-2}. $K(x^*, t)$ of dual-layer filter is predicted from eqs. (5.9) and (5.10) by adopting $N = 50$ for individual layers. Similar results can be achieved by adopting $N = 25$ (figure 5.11) and even $N = 10$ (figure 5.12). The only influence of choosing a larger N is that the predicted deposition profile is in higher resolution. It should be noted that $K(x^*, t)$ in y-axis of figure 5.10 (also 5.11 and 5.12) is in logarithmic scale since the deposit mass in microfiber layer is two orders of magnitude lower than that in nanofiber layer. $K(x^*, t)$ in nanofiber layer of filter F starting with 890 kgm^{-3} at face skin region decreasing to 219 kgm^{-3} at back region, while filter E has this value starting with 602 kgm^{-3} at face skin region decreasing to 181 kgm^{-3} across nanofiber layer thickness. The more uniform deposition profile across nanofiber layer in filter E leads to lower pressure drop increase rate.

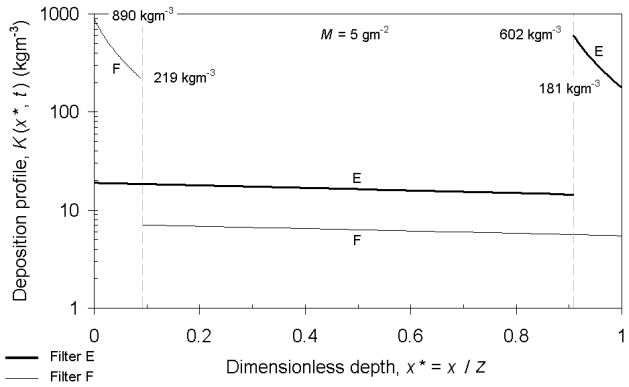

Fig. 5.10 Deposition profile across filters E and F after collected 5 gm^{-2} deposit (N = 50)

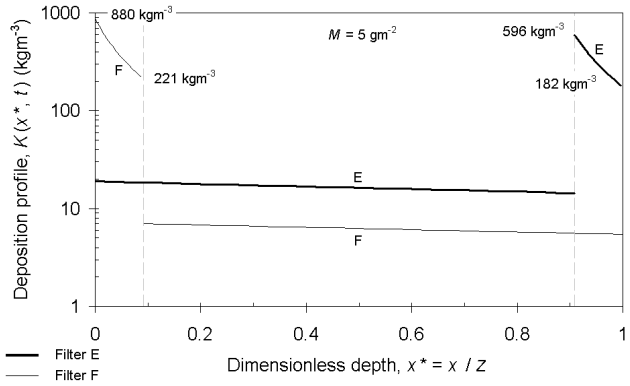

Fig. 5.11 Deposition profile across filters E and F after collected 5 gm^{-2} deposit (N = 25)

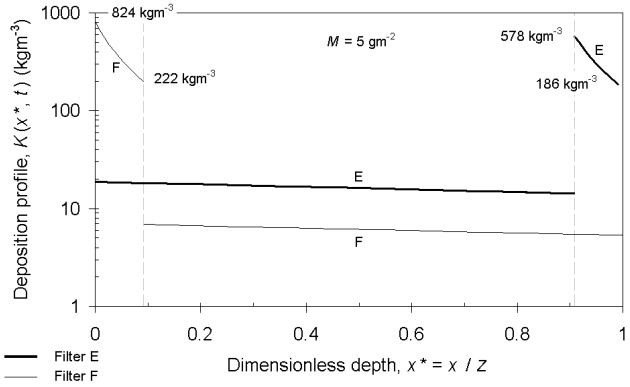

Fig. 5.12 Deposition profile across filters E and F after collected 5 gm^{-2} deposit (N = 10)

In the following, the points that are somewhat hidden in the semi-empirical model on deposition profile are discussed. This model assumed the nanofiber and microfiber layers act independently and do not affect each other's filtration performance. However, Przekop and Gradoń [53] have used the Lattice-Boltzmann

method to simulate aerosol flow in a mutli-scale system formed by nanofibers and microfibers, and found that nanofibers placed immediately (i.e. at most several diameters of microfiber) before microfibers become strong attractors for collecting particulates due to the high velocity gradients formed around. Hence, the actual amount of deposit in nanofiber layer of filter F is more than that estimated from our model. This is also one of the plausible factors rendering W_A of filter F slightly larger than W_A of filter E under the same solids load W. This argument is most appropriate for a filter with both types of fibers intermingled. However, in our case with distinct separate layers of fiber sizes, nanofibers at the surface of filter F should be far enough from the backing microfibers and the flow pattern around them will not be significantly affected by the backing microfibers. Hence, our model should provide a reasonable estimate on the deposition profile. For filter E, since the nanofiber layer is downstream of the microfiber layer, some nanofibers are shielded from aerosol flow by the larger microfibers, thus cannot participate in filtration. In this case, the loading model will over-estimate the amount of deposit collected by nanofibers immediately downstream of microfibers. This may be a more plausible reason for the slightly lower efficiency under aerosol loading for filter E when compared to filter F. Last but not least, re-entrainment affects the deposition profile in such a way that particulates collected in filter upstream portion are continuously brought to the downstream portion by fluid drag. However, our filter samples are continuously loaded with polydisperse aerosol having size distribution as shown in figure 5.5. High aerosol concentration causes deposition rate on fibers much higher than detachment rate of collected aerosol so that the entrainment effect may not be

that significant in this study.

Filter G is also an inhomogeneous dual-layer filter, but its nanofiber layer has a gradient solidosity by stacking the more porous (also more permeable) filter C upstream to the less porous filter A. As depicted in figure 5.9, although the pressure drop across filter G (53.96 Pa) is higher than filter E (44.13 Pa) at clean state, filter G has a lower pressure drop increase rate under loading. Under 5 gm^{-2} deposit, the pressure drop across filters E and G are 356 and 289 Pa respectively, and their difference grows with deposit mass. Figure 5.13 shows the deposition profile across filter G when W equals to 5 gm^{-2}. Compare with figure 5.10, the deposition profile across nanofiber layers of filter G is more uniform than that of filter E. It is because the nanofiber layer in filter G has a gradient solidosity, using the side with higher porosity to accommodate the densely packed deposit at face region, while leaving the side with lower porosity to handle the tail region of deposition profile. This relieves the skin effect as observed in homogeneous single-layer nanofiber filter.

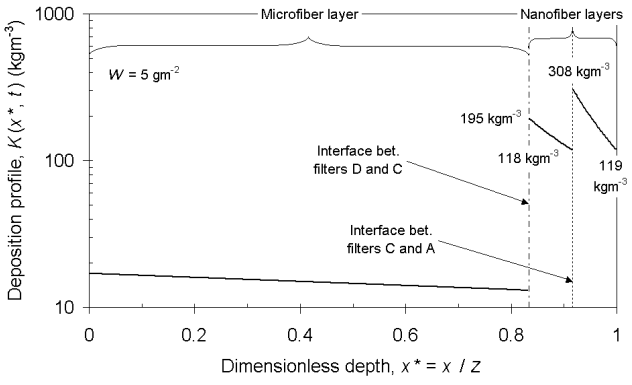

Fig. 5.13 Deposition profile across filter G after collected 5 gm^{-2} deposit (N = 50)

The thickness of microfiber layer does have effect on the filtration performance of the dual-layer filters. The dual-layer filters will have higher filtration efficiency and pressure drop at clean state when thicker microfiber layers are used. On the other hand, thicker microfiber layer can trap more dust from the aerosol stream thus reduces the loading on the downstream nanofiber layer, which leads to lower pressure drop increase rate (i.e. higher dust holding capacity). The balance between clean state filtration efficiency and dust holding capacity evolves to an optimization problem of practical value, which is worth to investigate in the future.

5.5 Chapter conclusions

It has been demonstrated that the higher filtration efficiency and quality factor of nanofiber filter does not necessarily imply that it is “absolutely” better than microfiber filter. Microfiber filter has higher dust holding capacity under continuous loading of sub-micron aerosol, as justified from its much lower pressure drop increase rate than nanofiber filter. In order to compensate for each other’s shortcoming, a dual-layer composite (filter E) formed by placing microfiber filter (filter D) upstream and nanofiber filter (filter A) downstream is proposed. Loading test results show that filter E has lower pressure drop increase rate than its control sample filter F, first of all because the upstream microfiber layer in filter E has collected part of the challenging aerosol (despite they may be sub-micron in size), thus reduces the loading on downstream nanofiber layer. Secondly, the deposition

profile in nanofiber layer of filter E is more uniform than that of filter F (reducing the skin-layer effect), thus its pressure drop increase rate is suppressed significantly. Thirdly, filter F has nanofibers placed immediately before microfibers and they are unobstructed for collecting aerosol in contrast to the reverse arrangement of filter E. Hence, a major portion of aerosol collected by filter F is in its nanofiber layer. The nanofiber layer downstream of the microfiber layer can be further improved by having a gradient solidosity increasing towards downstream. This provides a transition from the more porous microfiber to the more densely packed nanofiber, which is favorable in redistribution of deposit in the dual-layer filter translating to even lower pressure drop and effectively mitigating the skin effect. Our findings suggested that the inhomogeneous dual-layer filter is effective to relieve clogging or skin formation in nanofiber filter by providing better capacity utilization. On the other hand, nanofiber enhances sub-micron aerosol capture, rendering our proposed dual-layer filter suitable to extended operation from clean to loaded state.

Chapter 6

Backflow regeneration of nanofiber filter

6.1 Chapter introduction

It has been mentioned in the conclusion of Chapter 4 that there are two methods to avoid rapid clogging of nanofiber filter. One of them is to use a dual-layer set-up with microfibers upstream to nanofibers in order to achieve a more uniform deposition profile across nanofiber layer thickness. This method has been studied in detail in Chapter 5. Another method is to regenerate the aerosol loaded nanofiber filter back to clean state regularly. For microfiber filter, it is typical to use an air jet to blow from its downstream side. The mechanism is to initiate mechanical shaking on the filter to loosen the dust agglomerate, and then remove the agglomerate fragments by fluid (air) drag. However, polymer based nanofibers are usually fragile and may detach easily from the substrate under backflow. Hence, to regenerate nanofiber filter by backflow method, it is important to adopt proper air jet pressure and backflow duration, preferably through electronic control devices.

Section 6.2 explains the set-up of backflow system used to regenerate aerosol loaded fibrous filter. Section 6.3 presents the results and findings on regeneration of different types of nanofiber filters in various degree of loading. Section 6.4 is a brief conclusion and provides an insight into further research on nanofiber filter regeneration.

6.2 Set-up of backflow system

Figure 6.1 shows the set-up of backflow system to regenerate aerosol loaded fibrous filter. The supply pressure of compressed air can be adjusted through a regulator. The compressed air is directed to a solenoid value, where its open and close duration is controlled through Programmable Logic Control (PLC). The air jet going out from the nozzle impacts on the backside of loaded fibrous filter. It initiates mechanical shaking on the filter and loosens the dust agglomerate, and then the agglomerate fragments are removed by fluid (air) drag. Figure 6.2 shows the pattern of pulsating air jet achieved by alternative opening and closing of solenoid valve. The open and close duration, also the number of cycles, are set through the PLC controller. Pressure drop across the filter is measured every 10 cycles of air jet pulse. The whole regeneration process lasts for 120 cycles. After regeneration, the filter is loaded under the same aerosol size distribution until meeting the pressure drop ceiling again. Regeneration and loading is repeated alternatively until a clear picture on the growth of residual pressure drop is obtained.

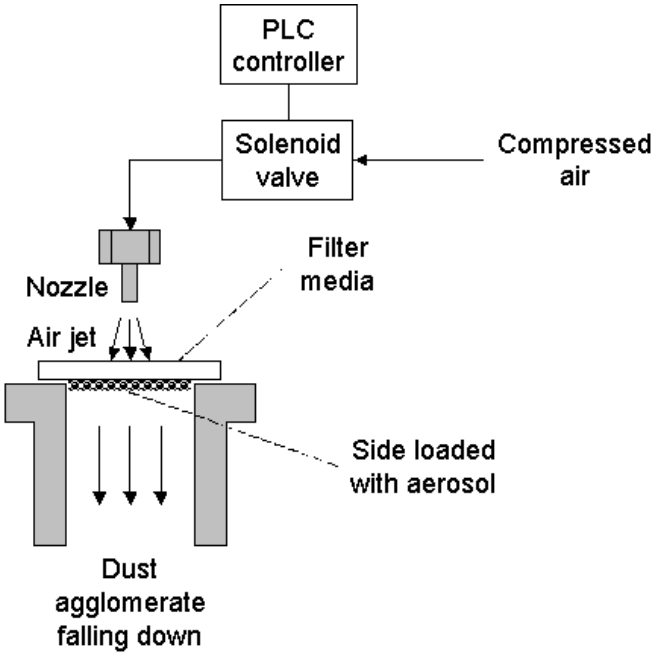

Fig. 6.1 Set-up of backflow system to regenerate loaded fibrous filter

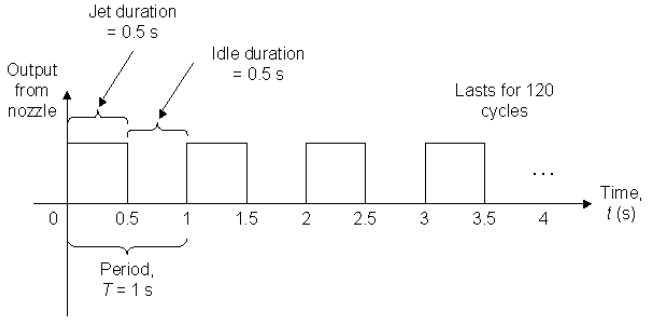

Fig. 6.2 Pulsating air jet through alternative opening and closing of solenoid valve

Longer pulse duration is more likely to destroy the fragile nanofibers, while shorter pulse duration may not provide effective cleaning. The pulse duration is obtained through trial-and-error. Starting from 1 sec, the pulse duration is reduced in 0.1 sec interval and the nanofiber layer is intact when the pulse duration eventually set at 0.5 sec. Pulse duration shorter than 0.5 sec has not been adopted, but it is expected that

more than 120 pulses are needed for effective cleaning when pulse duration is shorter than 0.5 sec.

6.3 Repeated loading and regeneration on nanofiber filter

Filter A is loaded to 300 Pa and regenerated by backflow of pulsating air jet repeatedly for 32 cycles. Its pressure drop along alternative loading and regeneration is depicted in figure 6.3. Backflow regeneration cannot completely remove all the dust agglomerate trapped inside the filter (i.e. patchy cleaning). Hence, the pressure drop does not restore to that across a clean (unused) filter, and the elevation from clean filter pressure drop after regeneration is called residual pressure drop. As shown in figure 6.3, residual ΔP increases with the number of loading and regeneration cycles, indicating an increasing amount of dust agglomerate trapped inside the filter. It can also be observed that the time required for filter A to be loaded up to 300 Pa is 3 hours in the starting cycle, and it decreases to 1.5 hours in the 32^{nd} cycle. Its loading and regeneration behavior is very similar to that of microfiber filters [52].

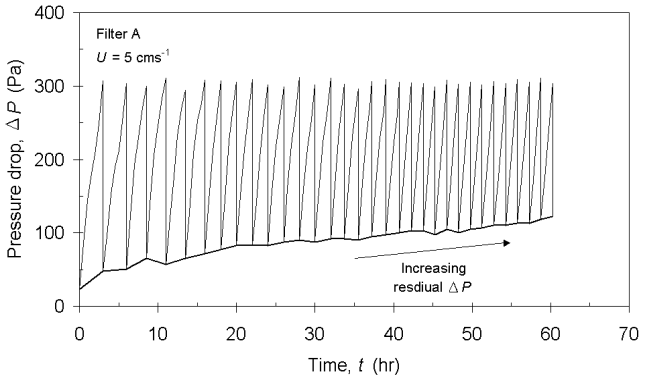

Fig. 6.3 Pressure drop across filter A along alternative loading and regeneration

Figure 6.4 shows the pressure drop across filter A against the number of air jet pulses during regeneration. The regeneration process can be roughly divided into three stages. Stage 1 shows a rapid decrease in pressure drop indicating a major portion of dust agglomerate is removed from the filter. In stage 2, the decrease rate drops meaning that the remaining dust agglomerate is more difficult to be removed by backflow. When regeneration reaches stage 3, pressure drop becomes nearly constant, representing the existence of residual ΔP (ΔP when n_s = 120) where no more trapped dust can be removed from the filter. As the number of regeneration increases, pressure drop decreases at a slower rate. This is due to an increasing portion of trapped dust comes from the residual of previous regeneration, which is more difficult to remove than the newly collected dust.

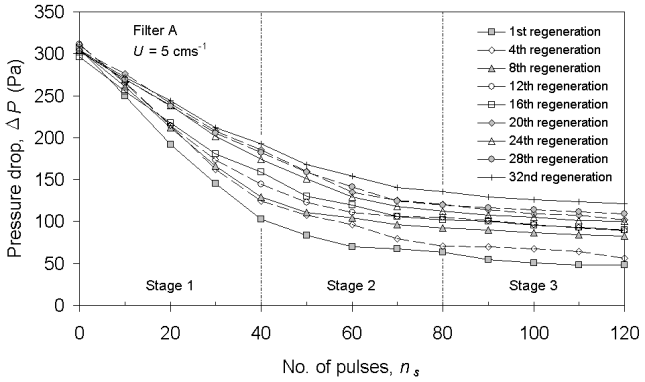

Fig. 6.4 Pressure drop across filter A against number of air jet pulses during regeneration

In Chapter 6 Section 6.3, nanofiber filter A is regenerated once its pressure drop reaches 300 Pa. From fig. 4.16, the time required to load nanofiber filter A up to 300 Pa is 4 hours (corresponds to 3.5 gm^{-2} deposit mass). On the other hand, fig. 4.11 shows that the time required to load microfiber filter D up to 300 Pa is estimated to be 80 hours. Hence, the nanofiber filter needs to be regenerated 20 times more frequent than microfiber filter. Past literature shows that the pressure drop across HEPA filter elevates to roughly 1250 Pa when deposit mass reaches 3 gm^{-2} (aerosol size: 0.153 µm). However, HEPA filter is always installed downstream of a set of pre-filters and is not subjected to such heavy aerosol loading.

The operation time for a filter to reach certain level of deposit mass depends on the concentration and size distribution of the incoming aerosol stream. The size distribution of aerosol stream adopted in this study is shown in fig. 5.5. Under this loading condition, the operation time for nanofiber filter A to accumulate 1 gm^{-2}

deposit mass is 1.5 hours. Fig. 4.20 shows that the pressure drop of filter A starts to elevate rapidly from 3.5 gm^{-2} deposit mass (300 Pa) onwards, and the filter should be replaced (or regenerated) at this point for low pressure drop applications such as facemask and respirator without active pumping or vacuuming air across the filter.

For backflow regeneration, the backflow devices can be integrated into the air circuit and automatically regenerates the filter once its pressure drop or operation time reaches certain level. It is not necessary to switch down the system, as in the case of filter replacement. If the filter is installed in critical location where downtime is a concern, regeneration is more appropriate than replacement for which stand-by filters are used temporarily. In addition, the replaced filter can always be regenerated and reused, and this practice is widely adopted by plants with industrial applications. On the other hand, if the filter is used under healthcare environment and loaded with infectious particles, backflow regeneration seems not appropriate. However, studies have been carried out to functionalize nanofibers by adding anti-bacterial or anti-viral chemicals, aiming to kill the bacteria or virus-laden particles being collected by the filter media.

6.4 Regeneration of nanofiber filters with different extent of loading

Filter H is another nanofiber filter with d_f = 300 nm, $Z = 1 \times 10^{-5}$ m, c_f = 0.045 and ΔP at clean state equals to 62 Pa. Filter H samples are loaded to different extent with maximum pressure drop (ΔP_{max}) equals to 300, 600, 1200 and 1800 Pa, followed by

regeneration. Figure 6.5 shows the loading and regeneration of filter H with different extent of loading. Figure 6.6 compares the regeneration curves of filter H among different ΔP_{max}. It shows the pressure drop decrease rate during backflow regeneration increases with ΔP_{max}, but residual ΔP remains the same irrespective of ΔP_{max} for the same filter. Hence, the effectiveness of backflow regeneration on loaded nanofiber filter does not undermine with the extent of loading (measured by higher ΔP_{max}). Figure 6.7 compares the dimensionless ΔP (= ΔP / ΔP_{max}) across filter H among different values of ΔP_{max}. By performing regeneration once filter H reaches 300 Pa, the dimensionless residual ΔP is 23.81 %. When regeneration is performed until filter H reaches 1200 Pa, the dimensionless residual ΔP reduces to 6.12 % and this percentage is less than that of the case for ΔP_{max} = 300 Pa indicating the nanofiber can accommodate for higher solids loading with an effective cleaning. However, further increase of ΔP_{max} beyond 1200 Pa does not lower the dimensionless residual ΔP as can be seen from the overlapping regeneration curves of ΔP_{max} = 1800 Pa and ΔP_{max} = 1200 Pa.

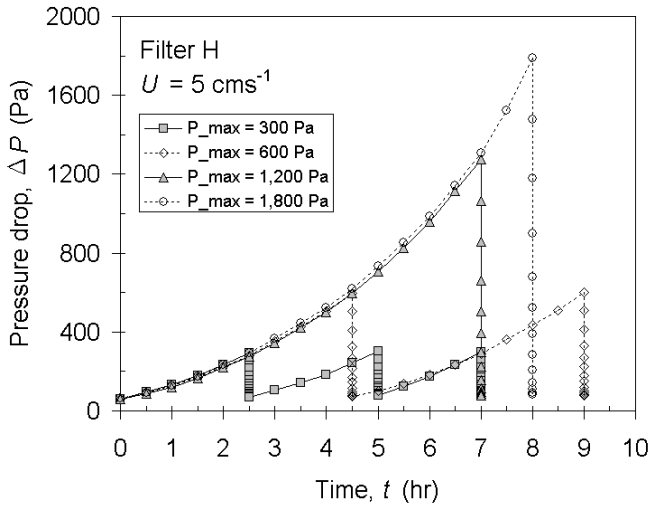

Fig. 6.5 Loading and regeneration of filter H with different extent of loading

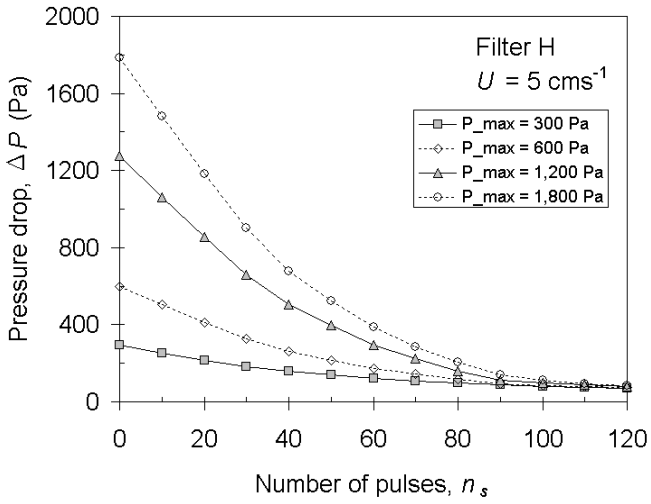

Fig. 6.6 Regeneration curves of filter H with different extent of loading

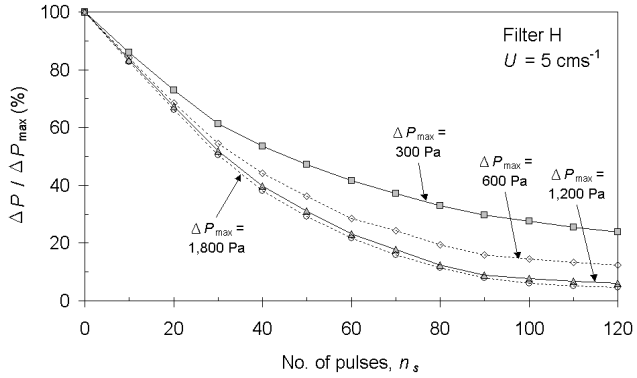

Fig. 6.7 Dimensionless regeneration curves of filter H with different extent of loading

6.5 Chapter conclusions

Backflow regeneration on loaded nanofiber filter is demonstrated in Chapter 6. To

avoid destroying the fragile nanofibers by air jet, the supply pressure and jet duration are accurately controlled through regulator and solenoid valve. Under repeated loading and regeneration, the residual ΔP increases gradually, which is the same as the case of microfiber filter. Backflow regeneration proceeds in three stages. The first stage has the major portion of dust agglomerate removed readily from the filter, causing pressure drop decreases rapidly. The second stage requires the cleaning of dust agglomerate more difficult to be removed, hence the pressure drop decreases slower. No more dust agglomerate can be removed from the filter in the third stage and the pressure drop remains constant, which becomes the residual ΔP. By loading the same nanofiber filter to different extent, it shows the residual ΔP remains unchanged for different values of ΔP_{max}. The effectiveness of backflow regeneration on loaded nanofiber filter can be evaluated by plotting dimensionless ΔP (= ΔP / ΔP_{max}) against number of pulses n_s, known as the dimensionless regeneration curve. Dimensionless residual ΔP decreases with respect to ΔP_{max}, indicating backflow regeneration is more effective under higher extent of loading. However, there exists an upper limit such that further increase on ΔP_{max} does not lower dimensionless residual ΔP anymore (e.g. ΔP_{max} = 1,200 Pa for filter H), hence there exists an optimal ΔP_{max} for effective backflow regeneration.

Chapter 7

Self-production of nanofiber filter

7.1 Chapter introduction

In Chapters 4 to 6, the nanofiber filters for testing are provided from a manufacturer. They come in three different solidosities (c_f = 0.011, 0.017 and 0.024) with mean fiber diameter d_f equals to 300 nm. To obtain a broader picture on the effect of face velocity, solidosity and thickness on filtration performance of nanofiber filters, it is necessary to have self-produced samples for testing. Most researchers postulated that non-woven filters composed of nanofibers, or non-woven microfiber filter integrated with nanofibers, possess greatly enhanced filtration efficiency, but increased pressure drop as a trade-off. Hence, the amount of nanofibers in a filter medium has to be carefully adjusted to prevent incurring excess pressure drop. Past studies have demonstrated the filtration capability of media composed of electrospun Nylon 6 (N6) [15] and Polyethylene Oxide (PEO) nanofibers [14]. In addition, Dharmanolla and Chase [16] reported that it is possible to increase the quality factor (*QF*) of a microfiber filter by mixing microfibers and electrospun nanofibers through vacuum molding. They have proposed an algorithm to optimize the amount of nanofibers to be added for constructing a filter medium with maximized *QF*. To further understand the effect of properties such as face velocity, solidosity and thickness on filtration efficiency and pressure drop of nanofiber filters, isolated nanofiber layer has been fabricated in various forms for testing.

Nanofiber medium on itself is soft and fragile and cannot be used alone as air filters. However, nanofibers can be coated on a rigid substrate to form a composite that can be handled readily. Most often the substrate is a non-woven microfiber medium [18 – 20, 54]. For research purpose, it is desirable to use an extremely permeable microfiber medium with negligible filtration efficiency as the substrate, so that the filtration efficiency and pressure drop measured across the composite can be approximated to those of nanofiber layer [18, 54]. Nanofiber coating can be either produced by electrospinning method [12] or melt-blown process [19, 20], with diameter of electrospun fibers usually smaller than that of melt-blown fibers.

This Chapter will evaluate the effect of face velocity, nanofiber layer solidosity and thickness on filtration efficiency and pressure drop of filters with nanofibers coated on a substrate. The substrate is a non-woven microfiber medium with negligible filtration efficiency and pressure drop as compared to nanofiber layer. The nanofiber layer was self-produced by electrospinning using PEO as the polymer. Mean diameter of nanofibers was estimated to be 200 to 300 nm. Samples in various nanofiber layer solidosities were produced by adopting different electrospinning durations. Efficiency tests were performed using sub-micron sodium chloride (NaCl) aerosol ranging from 50 to 480 nm. Predictions from classical filtration theories were also used to check the experimental results, which indicated the need for modification in modeling the capture of sub-micron aerosol by nanofibers.

Section 7.2 explains the production process of nanofiber filters. The effect of nanofiber layer solidosity, face velocity and nanofiber layer thickness on filtration performance as observed from experiments will be discussed in Sections 7.3, 7.4 and 7.5 respectively. In Section 7.5, a novel method of practical importance called “multi-layering” is proposed to fabricate nanofiber filter with greatly reduced pressure drop. This is especially advantageous for high efficiency applications that requires densely packed nanofibers in the filter medium.

7.2 Production of PEO nanofiber filter

Figure 7.1 shows a schematic of the nanofiber electrospinning unit (NEU-010, KES Kato Tech Co., Ltd). The 20 ml syringe is filled with Polyethylene Oxide (PEO) solution. Its plunger is adhered to a linear actuator system in which the solution feed rate can be carefully adjusted and maintained steady throughout the electrospinning process. The capillary is connected to a high voltage supply and the drum is earthed as a collector. An electric potential is generated between the capillary and the drum. Solution that flows out slowly from the capillary is subjected to an electric force. The hemispherical solution droplet attached to the outlet of capillary then deforms into conical shape, which is known as the Taylor cone. A jet is produced when the electric force overcomes the surface tension of the Taylor cone. The jet travels through the air towards the rotating drum, where the substrate is wrapped around. Adjacent like charges deposited on the fiber repels against each other stretching the fiber and producing even smaller-diameter sub-branches. This whole process

continues until the jets or smaller jets hit the collector surface. At the same time, solvent evaporation in flight is enhanced as the sub-jets has large surface area leading to only polymer nanofibers deposited on the substrate surface. The syringe is set into transverse motion along the rotating axis of the drum to achieve wider covering of nanofibers on the substrate.

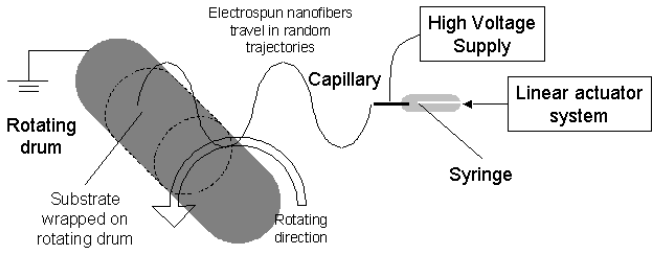

Fig. 7.1 Schematic of the nanofiber electrospinning unit

The conditions to electrospin PEO nanofibers are determined by referencing to Wan et al. [55], Doshi and Reneker [11] and Tsai et al. [14], accompanied by our repeated trials and inspection of samples under Scanning Electron Microscope (SEM) to observe for uniform fiber diameter with minimum bead formation. PEO solution is prepared by dissolving PEO powders (obtained from Aldrich) having a molecular weight of 600,000 grams/mole in a solvent containing 80 % by volume (vol. %) of isopropyl alcohol and 20 vol. % of water. The mass ratio between polymer and solvent is 5 %. The syringe has 20 ml nominal volume and the capillary is of 0.7 mm inner diameter. The applied voltage is 20 kV and the distance between capillary and drum surface is 14 cm. Solution feed rate is maintained at 6×10^{-3} ml/min. The substrate is a non-woven composed of coarse fibers with mean diameter at 14.7 μm.

Pressure drop across the substrate at 5 cms^{-1} is measured to be 1.39 Pa.

Nanofiber layer solidosity depends on electrospinning duration. The longer the electrospinning lasts, the more nanofibers can be coated on the substrate. The basis weight W of nanofibers as described in eqs. (2.7) and (2.8) thus increases with electrospinning duration. It is intuitive to assume both the solidosity c_f and thickness Z of nanofiber layer increases with electrospinning duration. To fabricate nanofiber layers of the same c_f but different Z, nanofiber filters (i.e. substrate coated with nanofibers) produced under the same electrospinning duration can be stacked up as depicted in figure 7.2. Practically, the nanofiber layer in the stack can be considered to have solidosity and thickness close to c_f and $2Z$.

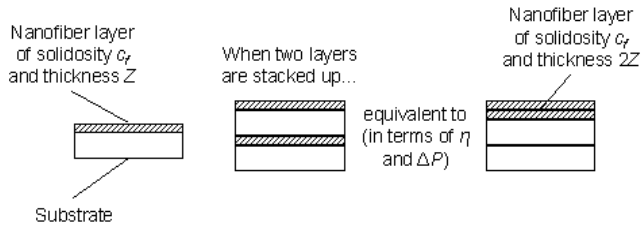

Fig. 7.2 Nanofiber layer of the same solidosity but different thickness

Table 7.1 summarizes the physical parameters of substrate and nanofiber layers coated on it. The substrate is obtained from manufacturer and the nanofiber layers (N1 – N9) are produced in our laboratory by electrospinning PEO solution under the conditions mentioned previously. N1 to N9 are produced under different electrospinning durations, with N1 the shortest and gradually increases to N9. The basis weight W of substrate is measured by electronic balance, while the values of

nanofiber layers are too small to be detectable. Instead, W of N1 to N9 was determined by multiplying the solution feed rate (6×10^{-3} ml/min), solvent density, polymer / solvent mass ratio (5 %) and electrospinning duration together. Thus, W is proportional to electrospinning duration. The mean fiber diameter d_f is estimated from SEM pictures. Since the nanofiber layers are coated on substrates, pressure drop ΔP across the nanofiber layers cannot be measured directly. Instead, the ΔP across clear substrate was first measured, and this value was being subtracted from the ΔP across substrates coated with nanofibers (i.e. composites). For example, ΔP across substrate coated with nanofiber layer N3 is measured to be 14.6 Pa at 5 cms^{-1}, and the ΔP across a clear substrate of 1.4 Pa is being subtracted to yield the ΔP across N3 being 13.2 Pa. The thickness Z of the substrate on the order of mm is measured by micrometer. Its solidosity c_f is estimated from eq. (2.6) by knowing ΔP / U, d_f and Z. It is very difficult to use SEM to measure the thickness of nanofiber layer because the nanofibers coated on substrate are very thin and easily damaged during the cutting process, thus the cross-section of nanofiber layer as viewed under SEM is heavily deformed. Instead, eq. (2.8) is used to estimate c_f. For example, N3 has d_f equals to 208 nm, W equals to 0.12 gm^{-2}, ρ_f equals to 1.22 gcm^{-3} and ΔP equals to 13.2 Pa when U = 5 cms^{-1}, its c_f is estimated to be 8.7×10^{-3}. It follows that Z as obtained from eq. (2.7) equals to 11.8×10^{-6} m. Values of c_f and Z obtained in this way should be allowed for variances. Nevertheless, we must estimate c_f and Z of nanofiber layers, as they are essential in modeling the filtration efficiencies. The uncertainty of ΔP is obtained from repeated measurements on the same sample. The uncertainties of derived quantities c_f and Z are obtained from

experimental uncertainty analysis. Figures 7.3 to 7.5 are the SEM pictures showing the top view of nanofiber layers of N1S, N4S and N8S respectively. While the substrate fibers can still be observed in pictures of N1S and N4S, they are completely covered up by nanofibers in N8S, indicating the increasing basis weight of nanofibers.

Medium	Substrate	N1	N2	N3	N4	N5	N6	N7	N8	N9
Mean fiber diameter, d_f (nm)	14.7 $\times$ 10^3	208	208	208	208	208	208	208	208	208
Basis weight, W (gm^{-2})	29.08	0.058	0.088	0.12	0.18	0.23	0.35	0.47	0.58	0.70
Solidosity, $c_f \pm \Delta c_f$ ($\times$ 10^{-3})	130 $\pm$ 27.4	3.9 $\pm$ 0.6	6.6 $\pm$ 0.95	8.7 $\pm$ 1.32	13.6 $\pm$ 1.63	17.8 $\pm$ 2.22	25.4 $\pm$ 2.82	30.8 $\pm$ 3.34	34.6 $\pm$ 3.79	36.0 $\pm$ 3.84
Thickness, $Z \pm \Delta Z$ ($\times$ 10^{-6} m)	100 $\pm$ 4	13.3 $\pm$ 2.05	11.8 $\pm$ 1.71	11.8 $\pm$ 1.79	11.4 $\pm$ 1.37	11.6 $\pm$ 1.45	12.2 $\pm$ 1.36	13.4 $\pm$ 1.45	14.9 $\pm$ 1.63	17.2 $\pm$ 1.84
Pressure drop ΔP at 5 cms^{-1} (Pa)	1.4 $\pm$ 0.08	4.4 $\pm$ 0.12	8.6 $\pm$ 0.19	13.2 $\pm$ 0.34	24.7 $\pm$ 0.25	37.7 $\pm$ 0.47	67.6 $\pm$ 0.38	99.4 $\pm$ 0.42	131.8 $\pm$ 0.61	161.2 $\pm$ 0.55

Table 7.1 Physical parameters of substrate and nanofiber layers coated on it

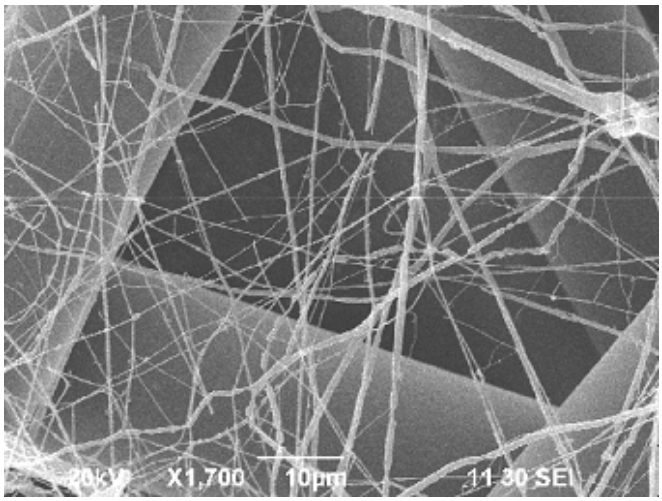

Fig. 7.3 SEM picture of N1S

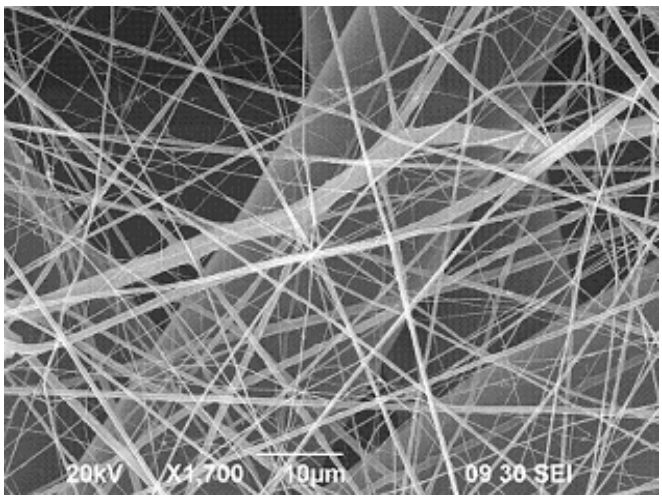

Fig. 7.4 SEM picture of N4S

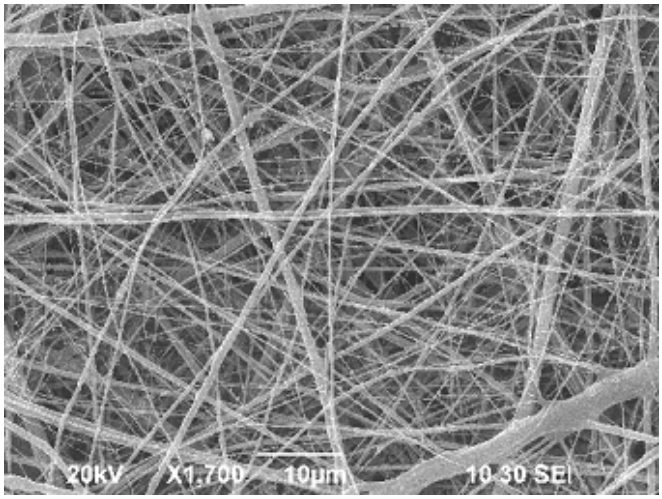

Fig. 7.5 SEM picture of N8S

The filtration efficiency (η) of the self-produced nanofiber filters N1S to N9S are tested in the same way as described in Section 2.2.

The nanofiber filters N1S to N9S produced from electrospinning method in this study have basis weight from 0.058 to 0.7 gm^{-2}. Commercial microfiber and HEPA filters usually have basis weight over 100 gm^{-2}. Hence, the material cost to manufacture nanofiber filters should be much lower than microfiber and HEPA filters due to the use of smaller amount of fibers. However, the existing plants using meltblown technology to produce microfiber and HEPA filters need to install new electrospinning machines in order to produce polymer-based nanofibers. It raises the initial cost.

7.3 Filtration performance vs. Nanofiber layer solidosity

Figure 7.6 shows the experimental filtration efficiencies at face velocity of 5 cms^{-1} of clear substrate and substrates coated with nanofibers, together with predictions (continuous curves) from the empirical correlation [eqs. (3.1) – (3.4)] described in Section 3.2. Noted "N1S" represents the composite formed by coating nanofiber layer N1 on substrate S. Experimental results indicate that clear substrate offers negligible filtration efficiency (less than 2 %) compared to composites. It follows that the filtration efficiency as measured across composites can be approximated to that of nanofiber layers. As expected, the efficiency curve shifts upward from N1S to N9S due to an increase in basis weight of nanofibers. Nanofiber coating enhances the filtration efficiency of microfiber substrate, also reduces the most penetrating particle size (MPPS) down to 140 nm. Other studies [18, 20, 54] also showed that composites formed by coating nanofibers on microfiber substrate always have MPPS lower than conventional microfiber filters.

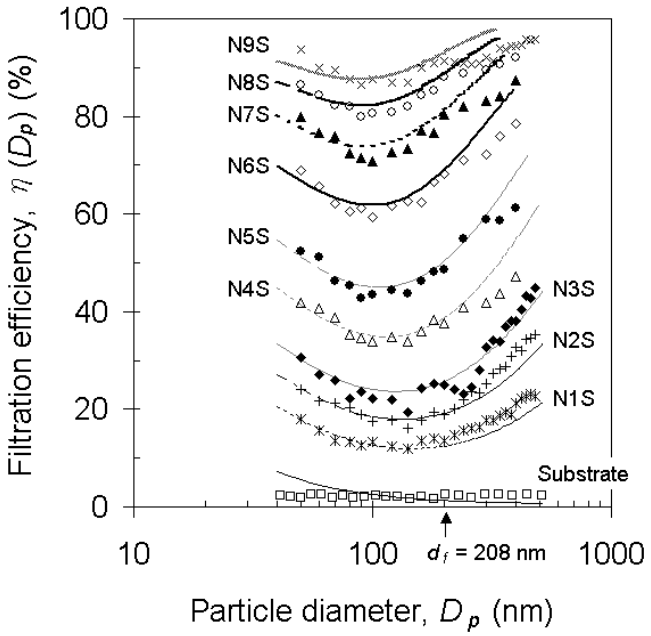

Fig. 7.6 Filtration efficiencies of clear substrate (S) and substrates coated with nanofibers (N1S to N9S)

Since N1S to N9S are dual-layer composites, their theoretical efficiencies are given by:

$$\eta_C = 1-(1-\eta_N)(1-\eta_S) \qquad \text{Eq. (7.1)}$$

where η_C is the filtration efficiency of composite, η_N and η_S are the filtration efficiencies of nanofiber layer and substrate respectively, each determined according to the empirical correlation [eqs. (3.1) – (3.4)] described in Section 3.2. Kn_f of substrate is 9×10^{-3} (d_f = 14.7 μm), thus the flow over fibers belongs to aerodynamic slip flow regime ($0.001 < Kn_f < 0.25$). Hence, the model built upon Navier-Stokes equation with slip correction is suitable to predict the filtration efficiency of substrate. On the other hand, Kn_f of nanofiber layer is 0.64 (d_f = 208 nm), rendering the flow over fibers transitional (i.e. transition from slip to molecular

flow) which is difficult to simulate, and the model is not a physical representation on flow problem in nano-scale. Moreover, our test aerosol is sub-micron in size from 50 to 480 nm. It follows that aerosols and fibers are of similar scale and aerosols can no longer be treated as point masses not affecting the flow over fibers, which contradicts with model's assumption. Despite of this, the theoretical and experimental filtration efficiency of composite containing nanofiber layer are still compared to determine the possible deviation. Surprisingly, the model can predict quite accurately the filtration efficiencies for D_p smaller than 100 nm over the whole test range on nanofiber layer solidosity. For D_p larger than 300 nm, the experimental efficiency curve agrees with theoretical one over the range of nanofiber layer solidosity from 3.9 (N1S) to 8.7 (N3S) $\times$ 10^{-3}. Starting from 13.6 $\times$ 10^{-3} (N4S), the model over-estimates filtration efficiencies for D_p larger than 300 nm and the deviation grows with particle size. This over-estimation even starts early at D_p = 200 nm when nanofiber layer solidosity equals to 36.0 $\times$ 10^{-3} (N9S). Hence, the model seems to over-estimate the interception effect offered by nanofiber in capturing particles larger than its diameter especially under higher solidosity condition.

The theoretical MPPS can be obtained by differentiating eq. (3.1) with respect to D_p and set to zero, or just by inspection from the theoretical efficiency curve. In figure 7.7, the dotted line connecting theoretical MPPS of N1S to N9S shows a generally decreasing trend against nanofiber layer solidosity, where experimental results also agree with the trend.

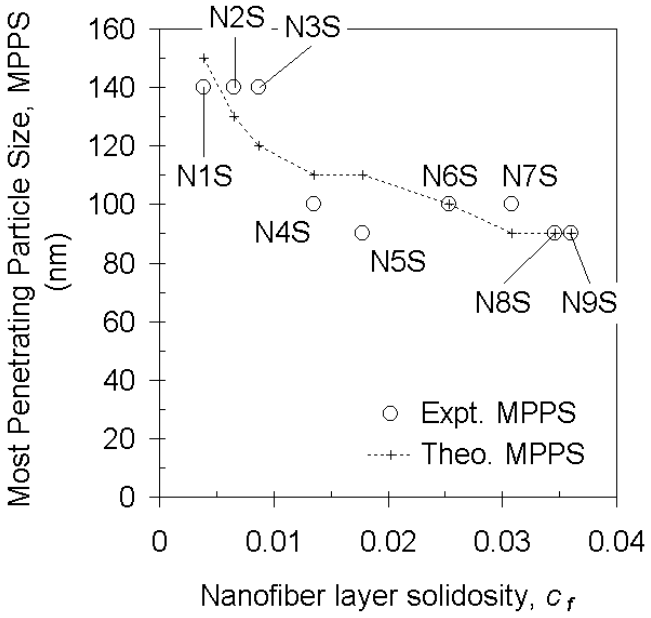

Fig. 7.7 MPPS as a function of nanofiber layer solidosity

7.4 Filtration performance vs. Face velocity

Figure 7.8 compares the filtration efficiencies under face velocities of 5 and 10 cms^{-1}. Experimental results show that filtration efficiencies over particle size range from 50 to 480 nm generally decrease with respect to increase in face velocity from 5 to 10 cms^{-1}. This phenomenon occurs for all composites, despite only the results of N1S, N3S, N5S, N7S and N9S are depicted in figure 7.8. The reduction on filtration efficiency becomes larger at smaller particle sizes. This is in agreement with theoretical prediction because doubling the face velocity is equivalent to reducing by a factor of half the retention time of particles in the nanofiber filter, thus lowers the chance for particles to collide on fibers through Brownian motion (diffusion). Since diffusion is the dominating capture mechanism for particles smaller than 100 nm, the

filtration efficiencies of these particles are mostly affected. For particles larger than 300 nm, the filtration efficiencies remain nearly unchanged when face velocity increased from 5 to 10 cms^{-1}. This is due to the fact that the Reynolds number (*Re*) based on the nanofiber diameter ranges between 7×10^{-4} and 1.4×10^{-3} which is under creeping low Reynolds number flow ($Re << 1$) and the streamlines in such flow field does not change, hence capture, by the nanofiber, of the aerosol as carried by the stream flow (i.e. interception) remains unchanged.

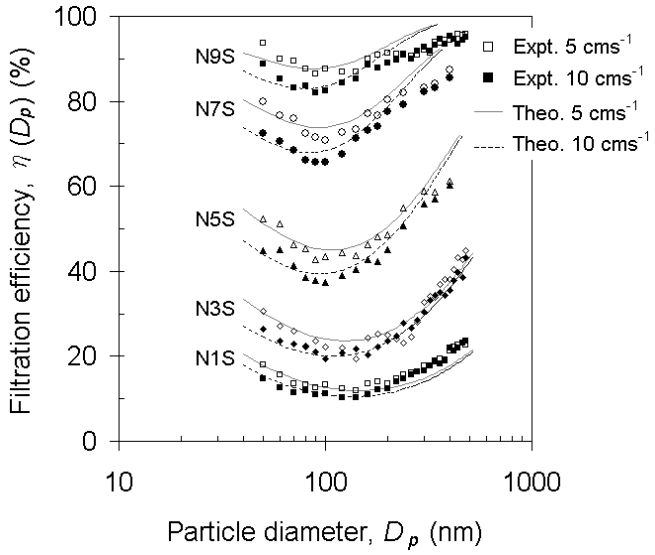

Fig. 7.8 Filtration efficiencies of N1S, N3S, N5S, N7S and N9S under face velocities of 5 and 10 cms^{-1}

When face velocity increased from 5 to 10 cms^{-1}, the model still generates efficiency curve closely agree with experimental values for composites N1S and N3S. However, predicted efficiency curve starts to deviate from experimental values at larger particle sizes as nanofiber layer solidosity increases. This has been observed

in the case of 5 cms^{-1} in Section 7.3. The same observation under 10 cms^{-1} further implies that assumed flow independence between larger particles and smaller fibers cannot be hold when nanofibers become more densely packed. Figure 7.9 plots experimental and theoretical η_D against Peclet number (*Pe*) of nanofiber layers N1 and N9. Theoretical η_D is predicted by eq. (3.3). Experimental η_D is obtained by first back-calculate single fiber efficiency η_f from experimental filtration efficiency η using eq. (3.1), followed by subtracting η_R [eq. (3.4)] from η_f. It shows the applicability of eq. (3.3) to nanofiber filters when *Pe* is smaller than 50.

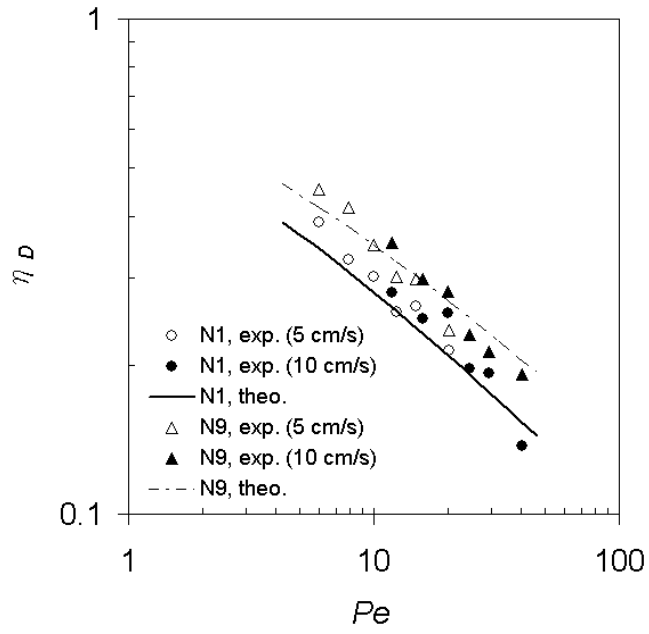

Fig. 7.9 Comparison of experimental and theoretical η_D of nanofiber layers N1 and N9

For particles smaller than 50 nm, the dominating filtration mechanism is diffusion. From fig. 7.9, both experimental results and theoretical predictions show that the

single fiber efficiency due to diffusion (η_D) increases with decreasing Peclet number (*Pe*). Since smaller aerosol has lower *Pe*, it is expected that the filtration efficiency continues to increase when particle size goes under 50 nm, but will start to flatten when particle size goes down further.

Figure 7.10 shows the quality factor (*QF*) at a particle size of 200 nm as a function of nanofiber basis weight (*W*) under face velocities of 5 and 10 cms^{-1}. From Darcy's Law, pressure drop across filter increases linearly with face velocity in laminar flow situation. As shown in figure 7.8, filtration efficiency generally decreases with respect to increase in face velocity. Hence, quality factor as an indicator to filtration performance should become lower at higher face velocity, which is depicted in figure 7.10. *QF* of nanofiber filter decreases with *W*, and most rapidly at initial values of *W*. This trend follows when face velocity increased to 10 cms^{-1}, but subjected to a lower decrease rate. To have better filtration performance, it is recommended to adopt the lowest possible face velocity when nanofiber filter is used. In addition, it is more cost-effective to use lower basis weight of nanofibers due to the relatively higher *QF*, which is the basis of "multi-layer" filter using multiple low-basis weight nanofiber layers to be discussed later.

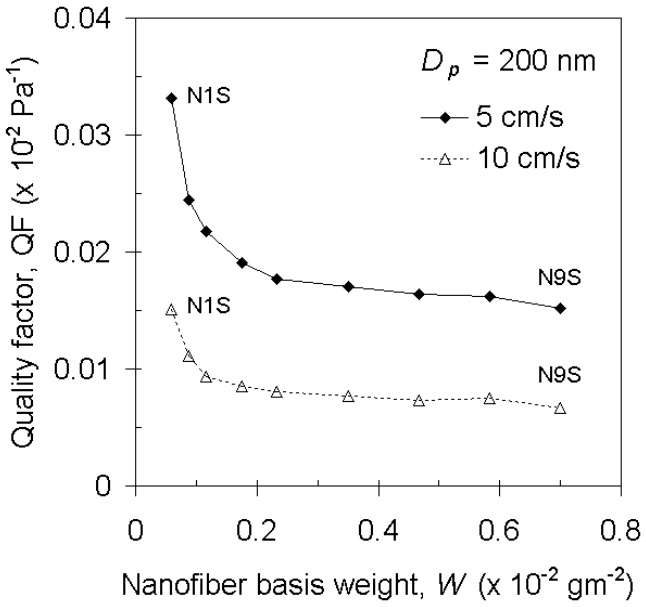

Fig. 7.10 Quality factor at particle size of 200 nm against basis weight of nanofibers under face velocities of 5 and 10 cms^{-1}

7.5 Filtration performance vs. Thickness of nanofiber layer

Two and three layers of N3S are stacked up (so-called N3S ×2 and N3S ×3) in order to form nanofiber layers with the same solidosity but increased thickness as compared to single layer of N3S. Given the filtration efficiency and pressure drop across a filter as η and ΔP respectively, it can be deduced from eq. (2.3) that the quality factor of a composite formed by stacking up k identical layers of the filter remains unchanged, i.e.

$$QF_k = -\frac{\ln(1-\eta)^k}{k(\Delta P)} = -\frac{\ln(1-\eta)}{\Delta P} = QF \qquad \text{Eq. (7.2)}$$

Figure 7.11 shows the filtration efficiencies of N3S, N3S ×2 and N3S ×3 at 5 cms^{-1}. Practically, nanofiber layer solidosity (c_f) remains close to 8.7×10^{-3}, while nanofiber layer thickness (Z) and basis weight (W) increase in discrete multiples. Pressure drop measured across N3S ×2 and N3S ×3 are 29.75 and 47.23 Pa respectively, which are close to two and three times of ΔP across N3S (14.58 Pa). ΔP across individual N3S layers in N3S ×2 and N3S ×3 have also been measured. In N3S ×2, they are 15.44 and 14.31 Pa, thus making up to 29.75 Pa. In N3S ×3, they are 16.53, 14.7 and 16 Pa, thus making up to 47.23 Pa. Hence, ΔP measured across the individual N3S layers are 14.58, 15.44, 14.31, 16.53, 14.7 and 16 Pa respectively. The average is 15.26 Pa with a standard deviation equals to 0.80 Pa. It shows the variation in ΔP of each layer, which indicates the inevitable inhomogeneity of nanofiber packing as resulted from the random nature of electrospinning process. The MPPS of N3S is 140 nm and decreased slightly to 120 nm when Z is doubled. When Z is tripled, MPPS remains at 120 nm. It is believed that the effect of Z on MPPS is less prominent than that of c_f (as depicted in figure 7.7). Figure 7.12 shows the experimental quality factors of N3S, N3S ×2 and N3S ×3, which are close to each other as expected from eq. (7.2).

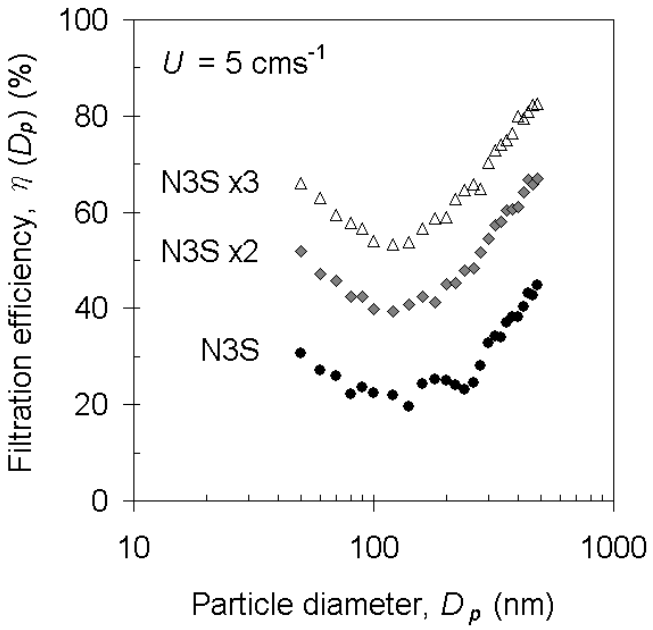

Fig. 7.11 Filtration efficiencies of N3S, N3S ×2 and N3S ×3 under face velocity of 5 cms^{-1}

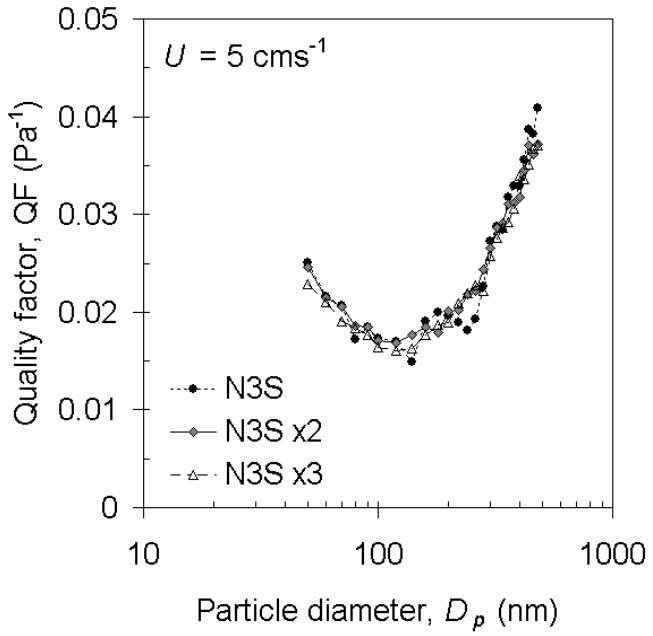

Fig. 7.12 Quality factors of N3S, N3S ×2 and N3S ×3 under face velocity of 5

cms^{-1}

The circles in figure 7.13 represent the experimental filtration efficiencies (of 200 nm aerosol) and pressure drop of N1S to N9S single nanofiber layer filter. These data points are linked up to show the diminishing return characteristic of nanofiber filter. By adding more nanofibers, the filtration efficiency increases in a decreasing rate with respect to pressure drop. It means that nanofibers deposited as single layer elevate the pressure drop without significantly improve the filtration efficiency, which lowers the quality factor and leads to poorer performance, especially when nanofiber basis weight is high (see figure 7.10). This problem may hinder the use of nanofibers in high efficiency filtration. However, eq. (7.2) shows that stacking up multiple filters does not alter the quality factor, and this postulation has been verified by experiment results as depicted in figure 7.12. Hence, it is prudent to investigate the pressure drop savings that can be achieved through "multi-layering". In figure 7.13, the dotted curve represents the projection when multiple units of N1S (W = 0.058 gm^{-2}) with high QF are stacked up. Under the same W of 0.70 gm^{-2}, N1S $\times$12 provides a pressure drop savings by 93.12 Pa, with filtration efficiency at 82.60 %, which is slightly lower than that of N9S at 91.37 %. When W equals to 0.23 gm^{-2}, pressure drop savings offered by N1S $\times$4 as compared to N5S is 15.90 Pa, with filtration efficiency drops from 48.69 to 44.17 %. It can be observed that ΔP savings through "multi-layering" becomes more significant at higher W. In addition, irrespective of single- or multi- nanofiber layer filter, they perform better than microfiber filter, as depicted in figure 7.13. As mentioned before, nanofibers are soft

and their non-wovens produced from electrospinning have fixed solidosity and thickness at each basis weight. Hence, “multi-layering” can also be regarded as an alternative to adjust the solidosity and thickness of nanofiber layer under a fixed basis weight while yielding high efficiency and low pressure drop.

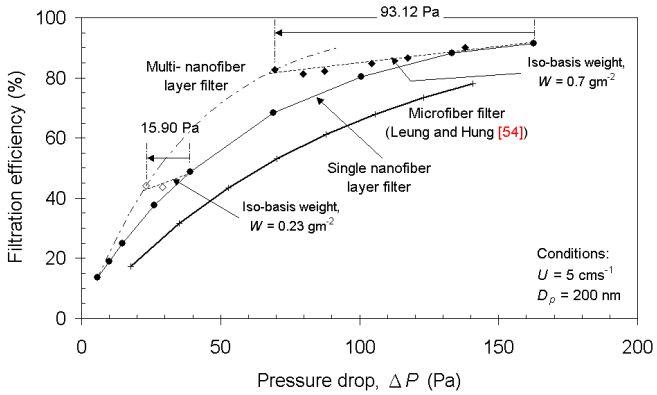

Fig. 7.13 Operation curves (U = 5 cms^{-1}, D_p = 200 nm) of multi- nanofiber layer filters formed by stacking up constituent units from N1S to N9S

The criteria of HEPA quality is to have filtration efficiency over 99.97 % at 0.3 µm aerosol and pressure drop lower than 392 Pa at 5 cms^{-1} face velocity. Hence, the minimum quality factor of HEPA filter media is 0.021 Pa^{-1}. On the other hand, our nanofiber filter N9S produced from electrospinning method can reach 91 % filtration efficiency at 0.3 µm aerosol with 161 Pa pressure drop at 5 cms^{-1} face velocity. The quality factor is 0.015 Pa^{-1}. Although the quality factor of our N9S is lower than HEPA media, it can be improved through “multi-layering” using the most porous N1S as the building block, yielding over 90 % filtration efficiency with quality factor reaches 0.035 Pa^{-1}. Through stacking up N1S, 99.97 % filtration efficiency

can be achieved with pressure drop expected to be 202 Pa, which is lower than HEPA filter.

7.6 Chapter conclusions

Nanofiber filters are produced by electrospinning PEO nanofibers on microfiber substrate. The mean diameter of PEO nanofibers is 208 nm, by which fluid flow around fibers falls under the transition regime. Firstly, the effect of nanofiber layer solidosity on filtration performance has been investigated. Both experiment and theory shows that the MPPS decreases with nanofiber layer solidosity. Secondly, the effect of face velocity on filtration performance has been studied. Filtration efficiency generally decreases with face velocity, and the reduction becomes larger at smaller particle sizes. This agrees with theoretical prediction. It is because increased face velocity reduces the retention time of aerosol within the nanofiber structure, thus lowers the chance for aerosol to collide on fibers through Brownian motion. In addition, it is recommended to adopt the lowest possible face velocity when nanofiber filter is used; otherwise the quality factor drops dramatically. Thirdly, the effect of nanofiber layer thickness on filtration performance has been investigated. Results show that the effect of nanofiber layer thickness on MPPS is less prominent than that of nanofiber layer solidosity. By adding more nanofibers on microfiber substrate, the filtration efficiency increases in a decreasing rate with respect to pressure drop. It means that nanofibers being deposited into single layer elevate the pressure drop without significantly improve the filtration efficiency,

which lowers the quality factor and leads to poorer performance. The performance can be improved by distributing the same amount of nanofibers sparsely through stacking up multiple filters, known as “multi-layering”. Pressure drop savings through “multi-layering” becomes more significant at higher nanofiber basis weight or applications that require high efficiency. In addition, under the same amount of nanofibers, stack up constituent units with lower nanofiber basis weight will enhance the pressure drop savings. Alternatively, a multi- nanofiber layer filter can be realized wherein the pressure drop is the same as a single nanofiber layer filter yet the filtration efficiency for sub-micron aerosol is significantly higher by putting additional nanofibers in the filter.

Chapter 8

Conclusions and suggestions for future research

8.1 Conclusions

The objective of this research to study the filtration of sub-micron aerosol by nanofiber media has been covered. First of all, three types of non-woven nanofiber filters having solidosities (c_f) at 0.011 (filter A), 0.017 (filter B) and 0.024 (filter C) and mean fiber diameter d_f at 300 nm, also a microfiber filter (filter D) with c_f equals to 0.048 and d_f at 1,800 nm are provided by a manufacturer for our research purpose. Under 5 cms^{-1} face velocity, nanofiber filter A shows higher filtration efficiency (η) and quality factor (QF) than microfiber filter D at clean state. However, this does not necessarily imply that nanofiber non-wovens is “absolutely better” than microfiber non-wovens for filtration purpose. By loading the filters with polydisperse sub-micron NaCl aerosol, it is observed that the pressure drop (ΔP) of nanofiber filter rises more rapidly than microfiber filter. The semi-empirical model also suggests this. Hence, the relatively low dust holding capacity is regarded as a weakness of nanofiber filter, as it leads to frequent filter replacement during extended use. Moreover, the pressure drop increase rate of nanofiber filter is very sensitive to c_f. The most penetrating particle size (MPPS) of clean nano- (A) and micro- (D) fiber filters are 103 and 203 nm respectively. It has also been discovered that at similar degree of loading based on deposit solidosity c_p, the shift of MPPS of nano- (A) and micro- (D) fiber filters are 11 and 75 nm respectively. The more stable

MPPS under loading is a potential advantage of nanofiber over microfiber filter.

In order to avoid rapid clogging of nanofiber filter, an inhomogeneous dual-layer media (filter E) formed by placing microfiber media (filter D) upstream and nanofiber media (filter A) downstream is proposed. Loading test results show that filter E has lower pressure drop increase rate than its control filter F (A upstream to D), first of all because the upstream microfiber layer in filter E has collected part of the challenging aerosol, thus reduces the loading on downstream nanofiber layer. Moreover, the newly proposed semi-empirical model shows that the deposition profile $K(x, t)$ across nanofiber layer of filter E is more uniform than that of filter F, thus its pressure drop increase rate is suppressed significantly. Serving two purposes, the dual-layer filter with microfibers upstream and nanofibers downstream is able to utilize the strength of nanofibers at clean state filtration for enhancing the quality factor and microfibers at loaded state filtration for improving the dust holding capacity.

Loaded nanofiber filter can be regenerated by backflow of pulsating air jet with precisely controlled pressure and period. Under repeated loading and regeneration, the residual pressure drop (ΔP) increases gradually, which is the same as the case of microfiber filter. During backflow regeneration, ΔP across nanofiber filter decreases with respect to number of air jet pulses n_s, and the trend can be roughly divided into three stages. The first stage has the major portion of dust agglomerate removed readily from the filter, causing ΔP decreases rapidly. The second stage involves the

cleaning of dust agglomerate more difficult to be removed, hence ΔP decreases at a slower rate. No more dust agglomerate can be removed from the filter in the third stage and ΔP remains constant, which becomes the residual ΔP. By loading the same nanofiber filter to different extent (maximum ΔP), the residual ΔP remains unchanged for different values of ΔP_{max}. The effectiveness of backflow regeneration on loaded nanofiber filter is evaluated by plotting dimensionless ΔP (= ΔP / ΔP_{max}) against n_s, known as the dimensionless regeneration curve. Dimensionless residual ΔP decreases with respect to ΔP_{max}, indicating backflow regeneration is more effective under higher extent of loading. However, there exists an upper limit such that further increase on ΔP_{max} does not lower dimensionless residual ΔP anymore, hence an optimal ΔP_{max} exists for effective backflow regeneration.

Besides manufacturer samples, we have produced our own nanofiber filters by electrospinning polymer nanofibers on microfiber substrate. The substrate is a non-woven microfiber medium with negligible η and ΔP as compared to nanofiber layer. The nanofiber layer is composed of electrospun polyethylene oxide (PEO) nanofibers with d_f equals to 208 nm. Experimental results show that the MPPS decreases from 140 to 90 nm when c_f of nanofiber layer increases from 3.9 to 36 $\times$ 10^{-3}. When face velocity U increases from 5 to 10 cms^{-1}, η decreases in general, and the reduction becomes larger at smaller aerosol sizes especially for D_p below 100 nm. By maintaining c_f at 8.7 $\times$ 10^{-2} and almost triple the thickness of nanofiber layer (Z), the MPPS decreases slightly from 140 to 120 nm. This suggests Z has less prominent effect on MPPS than c_f. By adding more nanofibers on microfiber substrate in a

single layer especially under dense fiber packing, ΔP elevates without significantly improving η exhibiting a diminishing return behavior. Hence, the method of "multi-layering" is proposed to fabricate nanofiber filter with greatly reduced ΔP. This is advantageous for high efficiency applications that require large basis weight (W) of nanofibers.

8.2 Suggestions for future research

Researchers have been putting efforts to improve filter media capture efficiency and air permeability throughout the years [56]. One of the ways is to reduce the fiber diameter. This research project has demonstrated nanofiber filter offers better filtration efficiency and quality factor than microfiber filter and the production of nanofiber media through electrospinning process. However, the filtration mechanism still relies on mechanical means mainly diffusion and interception, with a small degree of inertial impaction. To further improve the efficiency of fibrous filter, a traditional method is to apply electrostatic charges, thus initiating electrostatic attraction between fibers and particulates as a filtration mechanism in addition to the mechanical means. Filter composed of charged fibers are commonly referred as "electret" filter media. The filtration mechanism behind electret filter media has been studied since several decades ago [57 – 59], and N95 respirators is one of the daily life applications of electret filter media. The advantage of electret filter media is that the charge on fibers improves the filtration efficiency without causing extra airflow resistance [60 – 62]. However, electret filter media has disadvantages such

as it undergoes natural charge decay when exposed to ambient environment [63] or certain chemicals (e.g. xylene) in liquid phases [64] and the charges on fibers will also be shaded by collected particulate during extended operation [65 – 66], both leads to efficiency degradation.

It follows that electret and nanofiber media can be combined to enhance filtration performance. Compared to microfiber, nanofiber has larger surface area-to-volume ratio for deposition of electrostatic charges, making it an even better candidate for electret filter media. Hence, the key objective of future research is to develop electret filter media made of nanofibers, which can be regarded as an improvement to existing electret microfiber non-wovens, also the uncharged nanofiber non-wovens. Nanofiber media can be produced by electrospinning, followed by deposition of electrostatic charges on it through corona discharge. Previous studies [67 – 70] have confirmed the production of electret fibrous media by corona discharge. Change of filtration efficiency and pressure drop of electret nanofiber media under continuous aerosol loading should also be studied experimentally, hence quantifying the effect of charge shielding by sub-micron aerosol deposited on electrostatic nanofiber. Since backflow has been demonstrated as an effective method to regenerate uncharged nanofiber filter, its effectiveness on electret nanofiber media can also be studied.

The simulation of aerosol deposition in fibrous media to predict filtration efficiency largely facilitates filter design. Mostly, the single-fiber approach is adopted, which

involves the determination of flow field around fibers and calculation of aerosol tracks by Lagrangian method [71]. However, the continuum assumption no longer holds for flow over nanofibers [6]. Navier-Stokes equation is an improper mathematical description on flow over fiber with Knudsen number larger than 0.25. Moreover, the traveling sub-micron aerosol is in similar scale to the stationary nanofiber, meaning that the influence of the aerosol on the flow field around nanofiber cannot be neglected. Last but not least, the electrostatic attraction provided by electrostatic nanofiber acts as external force on aerosol. All the above mechanisms complicate the simulation of aerosol deposition in electret nanofiber filter. Direct Simulation Monte Carlo (DSMC) method is one of the possible ways to simulate this kind of nano-scale fluid structure interaction (FSI) problem, which is one of the future research directions.

Appendix I

To measure the filtration efficiency of a filter, aerosol of specific size is generated from electrostatic classification. Due to multiple-charge effect, the resultant aerosol stream always contains particles of the same electrical mobility (ξ) but different sizes (D_p) and charges (n). For example, the stream corresponds to 50 nm aerosol actually composed of 50 nm (+1 charged), 73 nm (+2), 92 nm (+3), 108 nm (+4), 124 nm (+5) and 138 nm (+6) particles. Multiple-charge effect at filter upstream can be corrected by using Wiedensohler [41] approximation. However, the filter under test will screen out particles to different extent depending on D_p; another method is thus required to determine the actual concentration at filter downstream from particle counter reading.

Suppose the filter upstream and downstream number concentration of 460 nm (+1) and 480 nm (+1) particles have been measured, the corresponding filtration efficiencies $\eta(460)$ and $\eta(480)$ can be determined directly from Eq. (2.1) due to the fact that their multiply charged (+2, +3, +4…) particles are larger than impactor's cut-off size, usually at 750 nm under normal operating conditions.

However, the 280 nm aerosol stream actually contains 280 nm (+1), 467 nm (+2) and 648 nm (+3) particles. By neglecting 648 nm (+3) particles due to its relatively low concentration in the aerosol stream, the relationship between particle counter reading and actual concentration is given by:

$C_{in,reading} = C_{in}(280_{+1}) + C_{in}(467_{+2})$ Eq. (AI.1)

$C_{out,reading} = C_{out}(280_{+1}) + C_{out}(467_{+2})$ Eq. (AI.2)

where $C_{in,reading}$ and $C_{out,reading}$ are the upstream and downstream number concentration as shown on the particle counter respectively. $C_{in}(467_{+2})$ is the upstream concentration of +2 charged 467 nm particles which is in a fixed proportion to $C_{in}(467_{+1})$ under the standard bi-polar charge distribution. $C_{in}(467_{+1})$ is obtained by interpolation using $C_{in}(460_{+1})$ and $C_{in}(480_{+1})$. $C_{in}(280_{+1})$ is then obtained from Eq. (AI.1). $C_{out}(467_{+2})$ is equal to $C_{in}(467_{+2})$ times $1 - \eta(467)$, as interpolated from $\eta(460)$ and $\eta(480)$. $C_{out}(280_{+1})$ is then determined according to Eq. (AI.2). Both $C_{in}(280_{+1})$ and $C_{out}(280_{+1})$ are substituted into eq. (2.1) giving $\eta(280)$. The above steps are repeated to obtain the filtration efficiencies from large to small particle sizes until the whole test range has been covered.

References

[1] Dorman, R.G. (1966). *Chapter VIII Filtration*, in Aerosol Science, C.N. Davies, ed., Academic Press, London, 195 – 222.

[2] Pich, J. (1966). *Chapter IX Theory of aerosol filtration by fibrous and membrane filters*, in Aerosol Science, C.N. Davies, ed., Academic Press, London, 223 – 283.

[3] Davies, C.N. (1973). *Air Filtration*, Academic Press, London and New York.

[4] Friedlander, S.K. (1977). *Smoke, dust, and haze*, John Wiley & Sons, New York.

[5] Brown, R.C. (1993). *Air Filtration*: *An Integrated Approach to the Theory and Applications of Fibrous Filters*, Pergamon Press, Oxford.

[6] Cercignani, C. (1988). *The Boltzmann equation and its applications*, Springer-Verlag, New York.

[7] Maze, B., Tafreshi, H.V., Wang, Q., Pourdeyhimi, B. (2007). A simulation of unsteady-state filtration via nanofiber media at reduced operating pressures, *Journal of Aerosol Science* 38: 550 – 571.

[8] Formhals, A. (1934). US Patent 1975504.

[9] Formhals, A. (1939). US Patent 2160962.

[10] Formhals, A. (1940). US Patent 2187306.

[11] Doshi, J., Reneker, D.H. (1995). Electrospinning Process and Applications of Electrospun Fibers, *Journal of Electrostatics* 35: 151 – 160.

[12] Subbiah, T., Bhat, G.S., Tock, R.W., Parameswaran, S., Ramkumar, S.S. (2005). Electrospinning of nanofibers, *Journal of Applied Polymer Science* 96: 557 – 569.

[13] Li, D., Xia, Y. (2004). Electrospinning of Nanofibers: Reinventing the Wheel?

Advanced Materials 16: 1151 – 1170.

[14] Tsai, P.P., Schreuder-Gibson, H., Gibson, P. (2002). Different electrostatic methods for making electret filters, *Journal of Electrostatics* 54: 333 – 341.

[15] Ahn, Y.C., Park, S.K., Kim, G.T., Hwang, Y.J., Lee, C.G., Shin, H.S., Lee, J.K. (2006). Development of high efficiency nanofilters made of nanofibers, *Current Applied Physics* 6: 1030 – 1035.

[16] Dharmanolla, S., Chase, G.G. (2008). Computer program for filter media design optimization, *Journal of the Chinese Institute of Chemical Engineers* 39: 161 – 167.

[17] Podgórski, A. (2009). Estimation of the upper limit of aerosol nanoparticles penetration through inhomogeneous fibrous filters, *Journal of Nanoparticle Research* 11: 197 – 207.

[18] Wang, J., Seong, C.K., Pui, D.Y.H. (2008). Investigation of the figure of merit for filters with a single nanofiber layer on a substrate, *Journal of Aerosol Science* 39: 323 – 334.

[19] Podgórski, A., Bałazy, A., Gradoń, L. (2006). Application of nanofibers to improve the filtration efficiency of the most penetrating aerosol particles in fibrous filters, *Chemical Engineering Science* 61: 6804 – 6815.

[20] Gradoń, L., Podgórski, A., Bałazy, A. (2005). *Filtration of nanoparticles in the nanofibrous filters*, in FILTECH EUROPA 2005 Volume II, VDI, Germany, 178 – 185.

[21] Davies, C.N. (1970). The clogging of fibrous aerosol filters, *Journal of Aerosol Science* 1: 35 – 39.

[22] Watson, J.H.L. (1946). Filmless sample mounting for the electron microscope,

Journal of Applied Physics 17: 121 – 127.

[23] Bergman, W., Taylor, R.D., Miller, H.H., Biermann, A.H., Hebard, H.D., daRoza, R.A., Lum, B.Y. (1978). *Enhanced filtration program at LLL – A progress report*, in 15th Department of Energy Nuclear Air Cleaning Conference, DOE, U.S., 1058 – 1099.

[24] Vendel, J., Mulcey, Ph., Letourneau, P. (1990). *Aerosol penetration inside HEPA filtration media*, in 21st Department of Energy / Nuclear Regulatory Commission Nuclear Air Cleaning Conference, DOE / NRC, U.S., 799 – 808.

[25] Letourneau, P., Renaudin, V., Vendel, J. (1992). *Effects of the particle penetration inside the filter medium on the HEPA filter pressure drop*, in 22nd Department of Energy / Nuclear Regulatory Commission Nuclear Air Cleaning Conference, DOE / NRC, U.S., 128 – 142.

[26] Novick, V.J., Klassen, J.F., Monson, P.R., Long, T.A. (1992). *Predicting mass loading as a function of pressure difference across prefilter / HEPA filter systems*, in 22nd Department of Energy / Nuclear Regulatory Commission Nuclear Air Cleaning Conference, DOE / NRC, U.S., 554 – 573.

[27] Thomas, D., Contal, P., Renaudin, V., Penicot, P., Leclerc, D., Vendel, J. (1999). Modeling pressure drop in HEPA filters during dynamic filtration, *Journal of Aerosol Science* 30: 235 – 246.

[28] Brown, R.C., Wake, D. (1999). Loading filters with monodisperse aerosols: Macroscopic treatment, *Journal of Aerosol Science* 30: 227 – 234.

[29] Podgórski, A. (1998). Macroscopic model of two-stage aerosol filtration in a fibrous filter without reemission of deposits, *Journal of Aerosol Science* 29: S929 –

S930.

[30] Sakano, T., Otani, Y., Namiki, N., Emi, H. (2000). Particle collection of medium performance air filters consisting of binary fibers under dust loaded conditions, *Separation and Purification Technology* 19: 145 – 152.

[31] Przekop, R., Moskal, A., Gradoń, L. (2003). Lattice-Boltzmann approach for description of the structure of deposited particulate matter in fibrous filters, *Journal of Aerosol Science* 34: 133 – 147.

[32] Dunnett, S.J., Clement, C.F. (2006). A numerical study of the effects of loading from diffusive deposition on the efficiency of fibrous filters, *Journal of Aerosol Science* 37: 1116 – 1139.

[33] Li, S.Q., Marshall, J.S. (2007). Discrete element simulation of micro-particle deposition on a cylindrical fiber in an array, *Journal of Aerosol Science* 38: 1031 – 1046.

[34] Payet, S., Bouland, D., Madelaine, G., Renoux, A. (1992). Penetration and pressure drop of a HEPA filter during loading with sub-micron liquid particles, *Journal of Aerosol Science* 23: 723 – 735.

[35] ASTM F 2299 (2003). Standard test method for determining the initial efficiency of materials used in medical face masks to penetration by particulates using latex spheres, American Standard of Testing and Material (ASTM) International, Pennsylvania.

[36] 42 CFR Part 84.181 (1995). Approval of respiratory protective devices Subpart K – Non-powered air-purifying particulate respirators, Office of the Federal Register, Maryland.

[37] BS EN 13274-7 (2002). Respiratory protective devices – Methods for test Part 7: Determination of particle filter penetration, British Standards Institution, London.

[38] BS EN 1822-1 (1998). High efficiency air filters (HEPA and ULPA) – Part 1: Classification, performance, testing, marking, British Standards Institution, London.

[39] Yang, S., Lee, G.W.M. (2005). Filtration characteristics of a fibrous filter pretreated with anionic surfactants for monodisperse solid aerosols, *Journal of Aerosol Science* 36: 419 – 437.

[40] Yang, S., Lee, G.W.M. (2005). Electrostatic enhancement of collection efficiency of the fibrous filter pretreated with ionic surfactants, *Journal of the Air & Waste Management Association* 55: 594 – 603.

[41] Wiedensohler, A. (1988). An approximation of the bipolar charge distribution for particles in the submicron size range, *Journal of Aerosol Science* 19: 387 – 389.

[42] Rader, D.J. (1990). Momentum slip correction factor for small particles in nine common gases, *Journal of Aerosol Science* 21: 161 – 168.

[43] Davies, C.N. (1952). The separation of airborne dust and particulates, *Proceedings of the Institution of Mechanical Engineers Part 1B*: 185 – 213.

[44] Werner, R.M., Clarenburg, L.A. (1965). Aerosol filters. Pressure drop across single-component glass fiber filters, *Industrial and Engineering Chemistry Process Design and Development* 4: 288 – 293.

[45] Kuwabara, S. (1959). The forces experienced by randomly distributed parallel circular cylinders or spheres in viscous flow at small Reynolds numbers, *Journal of the Physical Society of Japan* 14: 527 – 532.

[46] Happel, J. (1959). Viscous flow relative to arrays of cylinders, *American*

Institute of Chemical Engineers Journal 5: 174 – 177.

[47] Kirsch, A.A., Fuchs, N.A. (1967). The fluid flow in a system of parallel cylinders perpendicular to the flow direction at small Reynolds numbers, *Journal of the Physical Society of Japan* 22: 1251 – 1255.

[48] Ramarao, B.V., Tien, C., Mohan, S. (1994). Calculation of single fiber efficiencies for interception and impaction with superposed Brownian motion, *Journal of Aerosol Science* 25: 295 – 313.

[49] Wakeman, R.J. (2008). *Filtration in the framework of globalization and technical innovation*, in 10th World Filtration Congress Proceedings Volume III, VDI, Germany, 19 – 20.

[50] Miguel, A.F. (2003). Effect of air humidity on the evolution of permeability and performance of a fibrous filter during loading with hygroscopic and non-hygroscopic particles, *Journal of Aerosol Science* 34: 783 – 799.

[51] Song, C.B., Park, H.S., Lee, K.W. (2006). Experimental study of filter clogging with monodisperse PSL particles, *Powder Technology* 163: 152 – 159.

[52] Callé, S., Bémer, D., Thomas, D., Contal, P., Leclerc, D. (2001). Changes in the performances of filter media during clogging and cleaning cycles, *The Annals of occupational hygiene* 45: 115 – 121.

[53] Przekop, R., Gradoń, L. (2008). Deposition and filtration of nanoparticles in the composites of nano- and microsized fibers, *Aerosol Science and Technology* 42: 483 – 493.

[54] Leung, W.W.F., Hung, C.H. (2008). Investigation on pressure drop evolution of fibrous filter operating in aerodynamic slip regime under continuous loading of

sub-micron aerosols, *Separation and Purification Technology* 63: 691 – 700.

[55] Wan, Y.Q., He, J.H., Yu, J.Y., Wu, Y. (2007). Electrospinning of High-Molecule PEO Solution, *Journal of Applied Polymer Science* 103: 3840 – 3843.

[56] Lydon, R.P. (2008). *Advances relating to Filter Media Developments*, in 10th World Filtration Congress Proceedings Volume II, VDI, Germany, 19 - .

[57] Kanaoka, C., Emi, H., Otani, Y., Iiyama, T. (1987). Effect of Charging State of Particles on Electret Filtration, *Aerosol Science and Technology* 7: 1 – 13.

[58] Lathrache, R., Fissan, H.J. (1986). *Enhancement of particle deposition in filters due to electrostatic effects*, in 4th World Filtration Congress Proceedings Volume III, Belgium, 7.55.

[59] Lathrache, R., Fissan, H.J., Neumann, S. (1986). Deposition of submicron particles on electrically charged fibers, *Journal of Aerosol Science* 17: 446 – 449.

[60] Nifuku, M., Zhou, Y., Kisiel, A., Kobayashi, T., Katoh, H. (2001). Charging characteristics for electret filter materials, *Journal of Electrostatics* 51: 200 – 205.

[61] Łowkis, B., Motyl, E. (2001). Electret properties of polypropylene fabrics, *Journal of Electrostatics* 51: 232 – 238.

[62] Sae-lima, W., Tanthapanichakoonb, W., Kanaoka, C. (2006). Correlation for the efficiency enhancement factor of a single electret fiber, *Journal of Aerosol Science* 37: 228 – 240.

[63] Moyer, E.S., Bergman, M.S. (2000). Electrostatic N-95 respirator filter media efficiency degradation resulting from intermittent sodium chloride aerosol exposure, *Applied Occupational and Environmental Hygiene* 15: 600 – 608.

[64] Jasper, W., Hinestroza, J., Mohan, A., Kim, J., Shiels, B., Gunay, M.,

Thompson, D., Barker, R. (2006). Effect of xylene exposure on the performance of electret filter media, *Journal of Aerosol Science* 37: 903 – 911.

[65] Walsh, D.C., Stenhouse, J.I.T. (1997). The effect of particle size, charge, and composition on the loading characteristics of an electrically active fibrous filter material, *Journal of Aerosol Science* 28: 307 – 321.

[66] Ji, J.H., Bae, G.N., Kang, S.H., Hwang, J. (2003). Effect of particle loading on the collection performance of an electret cabin air filter for submicron aerosols, *Journal of Aerosol Science* 34: 1493 – 1504.

[67] Tabti, B., Dascalescu, L., Plopeanu, M., Antoniu, A., Mekideche, M. (2009). Factors that influence the corona charging of fibrous dielectric materials, *Journal of Electrostatics* 67: 193 – 197.

[68] Ignatova, M., Yovcheva, T., Viraneva, A., Mekishev, G., Manolova, N., Rashkov, I. (2008). Study of charge storage in the nanofibrous poly(ethylene terephthalate) electrets prepared by electrospinning or by corona discharge method, *European Polymer Journal* 44: 1962 – 1967.

[69] Ciach, T., Gradoń, L. (1996). Highly efficient filtering materials, *Journal of Aerosol Science* 27: S613 – S614.

[70] Kravtsov, A., Brüing, H., Zhandarov, S., Beyreuther, R. (2000). The electric effect in polypropylene fibers treated in a corona discharge, *Advances in Polymer Technology* 19: 312 – 316.

[71] Jiang, W., Cheung, C.S., Chan, C.K., Zhu, C. (2006). The aerosol penetration through an electret fibrous filter, *Chinese Physics* 15: 1864 – 1870.